Solar Energy Potential Analysis at Building Scale Using LiDAR and Satellite Data

by

Paula Aguayo

A thesis
presented to the University of Waterloo
in fulfillment of the
thesis requirement for the degree of

Master of Science
in
Geography

Waterloo, Ontario, Canada, 2013

AUTHOR'S DECLARATION

I hereby declare that I am the sole author of this thesis. This is a true copy of the thesis, including any required final revisions, as accepted by my examiners.

I understand that my thesis may be made electronically available to the public.

ABSTRACT

The two main challenges of the twenty-first century are the scarcity of energy sources and global warming; trigged by the emission of greenhouse gases. In this context, solar energy became increasingly relevant. Because it makes optimal use of the resources, minimizes environmental impacts, and is sustainable over time.

However, before installing solar panels, it is convenient pre-assessing the amount of energy that a building can harvest. This study proposes a methodology to semi-automatically generate information a building scale; on a large area.

This thesis integrates airborne Light Detection and Ranging (LiDAR) and WoldView-2 satellite data for modelling the solar energy potential of building rooftops in San Francisco, California. The methodology involved building detection solar potential analysis, and estimations at building scale.

First, the outline of building rooftops is extracted using an object-based approach. Next, the solar modelling is carried out using the solar radiation analysis tool in ArcGIS, Spatial Analyst. Then, energy that could potentially be harvested by each building rooftop is estimated. The energy estimation is defined in economic and environmental terms.

ACKNOWLEDGEMENTS

During this study I have been generously helped by many people. I would like to thank my supervisor, Prof. Dr. Jonathan Li, for accepting me under his supervision and helping me throughout my Master's studies. Moreover, I would like to thank Dr. Su-Yin Tan, for her help and tips on my assignments and term papers and to Dr. Haiyan Guan, who trained me in LiDAR data handling. I would like to thank USGS and Digital Globe for providing the satellite and LiDAR data used in this study, and the IEEE GRSS Data Fusion Technical Committee for organizing the 2012 Data Fusion Contest. Thanks to the National Renewable Energy Laboratory (NREL), at the U.S. Department of Energy, for making available the solar radiation data used in this study as well as for their clarifying e-mails and to all who help to carry out this study.

I am especially grateful to Ms. Mary McPherson for her kind help with my English writing. Finally, I want to extend my gratitude and thankfulness to my family, especially, my husband and dear daughter for their time, patience, and support throughout the years.

For my beloved Paramahansa Yogananda,

Who constantly offers me unconditional love and support

TABLE OF CONTENTS

GLOSSARY OF TERMS AND ABBREVIATIONS

2.5D: 2D representation of 3D data. It refers to a raster representation of the ALS data.

2D: Two dimensional

2D α-shape: polygonal boundary defined by a list of x, y positions.

3D: Three-dimensional

ALS data: data collected by Airborne Laser Scanning technique, each datum is a three-dimensional point.

DEM: digital elevation model, a raster grid that stores the elevation as function of the position, it can be a DTM or a DSM.

DSM: digital surface model represents the elevation data of a surface, including elements above the ground such as: cars, trees, power lines, and buildings.

DTM: digital terrain model represents the elevation at the ground level.

NDSM: normalised digital surface model represents object highs, it is the ground subtracted from a DSM, and makes the segmentation invariant to local changes in the terrain.

Pixel oriented classification: it is the traditional classification approach based on the spectral information of the pixel.

Object oriented classification: the processing units are no longer single pixels but image objects; the image has to be segmented into meaningful pixel groups or objects.

Raster: a regular grid, composed of pixels.

Roughness: In this work, roughness refers to local high variations.

Segmentation: “In computer vision, segmentation is the process of partitioning a digital image into multiple segments (sets of pixels, also known as superpixels). The goal of segmentation is to simplify and/or change the representation of an image into something that is more meaningful and easier to analyze” (Shapiro and Stockman, 2001)

Objects: all the connected pixels that hold the same value.

zMax: this grid stores the highest z-value found for each raster cell. It contains more values on top of trees and other semitransparent objects than zMin, making it possible to classify those objects. Note that trees are denser in zMax than in zMin.

zMin: this grid stores the lowest z-value found for each raster cell. It is useful when generating the ground surface.

LIST OF FIGURES

LIST OF TABLES

CHAPTER 1 INTRODUCTION

1.1 Motivation

Climate change and energy supply are major challenges for the twenty-first century. The consumption of fossil fuel has being dramatically increasing during the last 200 years, mainly because of the industrialisation of developed countries, and the rising world population (Colligon, 2006). This intensive use of fossil fuel has improved the quality of human life; however, the implementation of clean energies became urgent because the limited quantity of fossil fuel as well as its polluting nature.

In this context, solar energy is becoming increasingly relevant (Panwar et al., 2011). With a continual input of 170 billion megawatts, solar radiation is the main source of energy of the Earth, and drives its physical and biological processes (Geiger, 1965); all human activities depend upon solar radiation. Moreover, solar energy makes optimal use of the resources, minimizes environmental impacts, and is sustainable over time (Panwar et al., 2011).

In their efforts to develop solar energy many governments have subsidized urban residences to install solar panels; the photovoltaic market is rising at 30% per annum, especially in German and Japan (Green, 2004). In Canada, the Government of Ontario officially launched Canada's first feed-in tariff policy in September 2009. That expects it to be reflected in the increment of building-integrated photovoltaic BIPV.

In order to efficiently implement solar panels, it is necessary to assess the amount of energy that a building is able to harvest; estimating this amount in a whole area requires a building city model, as well as, a high-resolution solar radiation model. In this way is possible to

automatically or semi-automatically predict how much energy every building in the area can harvest, and even the best locations to install solar panels.

According to Dubayah and Rich (1996), topography is the primary factor determining the amount of solar energy at local scale. The attributes of the terrain such as elevation, slope, aspect (orientation), and shadowing can generate strong local gradients in energy. Because of these heterogenic special distributions of solar energy, accurate local scale maps are required for solar prospection; weather station data are not enough to yield accurate high-resolution results because a simple interpolation of measurements does not yield accurate local information. In order to create accurate isolation maps at local scale, it is necessary to take into account the spatial and temporal variation of radiation over the landscape.

This thesis proposes an object-based approach to integrate airborne Light Detection and Ranging (LiDAR) data and high-resolution multispectral imagery in order to semi-automatically generate a three-dimensional (3D) city model. In addition, the LiDAR data are used as input to feed a solar radiation model using a GIS approach, taking in account the spatial and temporal variation of solar radiation over a specific landscape, and producing a high-resolution solar radiation map, based on the topography of building roof tops. The model is parameterised using weather station data. Finally, solar energy prospection is performed for every building in the scene.

1.2 Research Objectives and Questions

This study is intended to contribute to the development of solar energy, replacement of fossil fuel, and reduction of the greenhouse emissions realised to the atmosphere. In that way, this research contributes to the solution of the two main challenges for our century: climate change and energy supply.

This study uses data from San Francisco, California, to generate information at building scale, about the potential of each structure to harvest solar energy. This energy amount will be expressed as economic and environmental benefits. This information can support decision makers such as administrators, owners, and energy planners.

This study uses an object-based approach to integrate LiDAR and multispectral imagery in order to semi-automatically extract building outlines. In addition, the local topography is derived from the LiDAR data, and the resulting digital surface model (DEM) is used to build a solar radiation model. The solar model is computed using an ArcGIS tool, Solar Analyst, which is parameterised using weather station data. A last stage assesses the potential energy that can be harvested from each building; this amount is expressed as economic saving and environmental benefits. The general objectives of this study can be summarized as follows:

1) To explore the dependency of building detection on different methods of segmentation and object sizes.
2) To analyse the efficiency of the predictors: The Normalized Difference Vegetation Index (NDVI), ratio Perimeter-Area (PA), Sobel, and Area, applied individually and combined for the task of separating buildings from vegetation.
3) To assess the result of a GIS approach for a local solar radiation model.

4) To develop a methodology to semi-automatically extract the building outlines and asses the solar potential of the building roofs, based on LiDAR data and Multispectral imagery.

In addition, this study aims to generate the follow information for each building:

5) Quantified the potential solar energy that each building can harvest by installing solar panels (on the rooftop).
6) Estimates the economic saving of harvesting this energy by comparing the price of buying the same amount of energy from a local distributor.
7) Quantify the contribution of the solar panels to mitigate greenhouse emissions; by calculating the alternative pollution (CO_2 realised to the atmosphere) of generating the same amount of energy by burning fossil fuels.
8) Map the best to locate solar panels places, in each building rooftop.

1.3 Thesis Structure

This thesis encompasses seven chapters:

Chapter 1 introduces the research motivation, general objectives and specific questions, finally, this chapter describes the thesis structure.

Chapter 2 examines the literature related of the two main branches of the research: solar radiation modelling and building extraction from LiDAR data.

Chapter 3 describes the study area, imagery, LIDAR data, and software packages used in this study. In addition, this chapter describes the methodology used in the building detection, solar radiation modelling, and presents a methodology to estimate at building scale: the potential energy harvestable, its cost, and carbon dioxide reductions.

Chapter 4 presents the results of the building detection process, the solar radiation modelling, and the estimations at building scale.

Chapter 5 discusses building detection dependency on predictors, segmentation and object sizes, discusses the calibration of the solar model, and the factors affecting the estimations at building scale.

Chapter 6 summarises the conclusions, discusses the limitations of this research, and does some suggestions for future studies.

CHAPTER 2 LITERATURE REVIEW

This chapter provides the present state of the art of mapping solar potential using LiDAR. The first section reviews the current research in solar potential modeling and the second section describes the theoretical basis of building outlines extraction from LiDAR data, and reviews related works.

2.1 Predicting Solar Potential of Rooftops Using LiDAR Data: An Overview

This section presents an overview of solar potential modeling. It outlines the relevance of solar resource, analyses spatial variation as a relevant factor influencing solar energy, describes the existing approaches used to measure and model solar radiation, and describes current research projects related to the present study.

2.1.1 The Solar Resources

The sun is the main source of energy on the Earth providing the power for the photosynthesis, and causing flows of air and water (Dubayah and Rich, 1996). The solar constant is the amount of energy that arrives to a surface facing the Sun; it is in equivalent to 1380 J/s and its average variation is 0.2% (NASA, 2006). Solar radiation is naturally expressed as light and heat, and can be transformed into electricity through solar panels. Solar energy can be captured through passive solar design (such as large windows), through thermal systems (to heat water) or harvested by solar panels (to generate electricity). The electricity can be stored or used for heating and lighting buildings (Gadsden et al., 2003).

Urban areas can be used to harvest solar energy through the application of solar technologies. Wiginton et al. (2010) state that 30% of the Ontario electricity demands could be generated by urban solar panels. Levinson et al. (2009) identify roof surfaces as an urban resource to harvest energy, one that has the advantage of generating few land-use conflicts; however, they highlight the need of regulation to access the solar resource.

Suri and Hofierka (2004) describe three categories of factors affecting solar energy: Earth features, terrain characteristics, and atmospheric extinction.

The Earth features determine the extraterrestrial solar radiation, which is the energy available at the top of the atmosphere. It varies according to the relative position of the Sun above the horizon, and is given by the Earth geometry and movements (rotation and translation). The exact position of the Sun respect to a point in the Earth can be accurately computed by applying astronomic formulas. It depends on Earth declination (time of the season), latitude, and solar hour angle (time of the day).

The topography affects the available solar radiation on a specific place. It depends on the landscape characteristics: elevation, slope, aspect and shadow. The attenuation of energy due to these factors can be precisely modeled from topographic data.

The atmospheric attenuation is given by scattering and absorption; both caused by gases and suspended particles solid and liquid (including clouds) on the atmosphere. Atmospheric attenuation involves complex interactions and can be modelled just with moderate level of accuracy.

The atmospheric extinction reduces the solar energy available at a specific place. That is because of the absorption and scattering produced by the atmospheric components: solids, liquids, and gases (including the clouds). This category depends on the atmospheric components and on the elevation, which determine thickness of the atmosphere.

Photovoltaic technology

The energy output of a PV panel depends on the incidental solar radiation and on the efficiency of the solar technology. The peak power, expressed as Watt-peak (Wp), is the maximum energy output obtained from a PV under standard conditions: a light intensity of 1000 W/m^2, temperature of 25°C, and an air mass of 1.5.

According to Bermasco and Asinari (2011) the main PV technologies are mono-crystalline, poly-crystalline and amorphous silicon or thin film. The mono-crystalline is the most efficient technology converting solar ration to electricity (15%). The poly-crystalline have an efficiency of 12%, however it cost is lower. The amorphous technology consist on a thin film of silicon that is spread over glass or stain-free-steal it efficiency is 6%, however, it price is lower too.

Under non-standard condition the efficiency decrees due to variation on temperature (10%), efficiency of the tilt angle (10%), and general losses of the system (16%).

The optimal tilt of the panels is the one that maximise the exploitation of the solar radiation; it varies according to the latitude and season. In winter, the sun beams are more horizontal, and a large angle (of the panel) obtains the higher amount of harvest radiation. In summer, the sun rays are more direct, and a small angle is recommended. In a fixed installation, a mean angle that maximises the yearly harvest is recommended. However, according to Chaudari et al. (2004)

near 98% of PV systems are installed without tilt to low the installation cost, in addition non tilt allows denser panels installation. The orientation is other factor influencing solar harvesting in the northern hemisphere the panels should be preferably facing south.

Chaudari et al. (2004) carry out a market study for the PV grid connected. This study analyses the potential market for PV under different price levels and the best states in USA to install PV.

This study depicts an increasing demand for PV systems from 2003 (70MWp) to 2010 (2.9 GWp). This demand represents a market of 6.6 billion dollars. The states from the pacific and mid-Atlantic regions account for a 52% of the PV demand. In California, the potential demand was estimated between 5 and 500 MWp per year; depending on the price of the PV system, and other factors such as the price of the natural gas.

This study assessed the most suitable states, from U.S.A, to install PV systems. The evaluation was made based on utility rates, solar resources and roof space availability. The states that represent higher demand for PV were California 39%, New York 6.6%, and Florida 5.9%.

This study identify three factors that affect the demand on PV systems, they are: the high price of the system, government subsidies and customer behaviour. The elevated price of PV systems is a disadvantage of the solar energy compared to the regular electricity. On other hand, the government incentives reduce the impact of the initial investment trough measurements such as green tag, tax credits, subsidies, low-interest loans, and accelerated depreciation. In addition, this study affirms that the certainty about the long term governmental policy is an important factor promotes PV. According to Chaudari et al. (2004) the attitude of the population toward energy generation has changed over the years. The first customers of solar panels were mainly concern about the environment. However, in the present, the companies improve their corporative image

by generating clean energy, and at residential levels, PV is a symbol of social status. In addition, many PV customers are seeking for an independent source of energy to reduce energy costs.

There are many forms to economically assess the cost-benefice of buying PV. For example, amount of investment, payback period, cost of electricity, or comparing the potential energy generated (by the PVs) to the electricity bill. Other considerations are cost of PV should not surpass 2% of the property value.

In 2010 the average payback period was estimated in 9-12 years (considering $2.00-2.50/Wpdc), and 13-19 years (for a price of $4.25-$5.30/Wpdc). The payback period was estimated based on system price and first year savings. For payback periods longer than 20 years, the demand for PV is considered zero.

2.1.2 Spatial Variation

At global scale, the amount of solar energy depends mainly on factors such as, the Earth latitude, rotation, and revolution around the Sun (Suri and Hofierka, 2004). However, at local scale, spatial variation is the main factor affecting the amount of solar energy captured (Miller et al., 2011). Because, at a given latitude and time period, the solar radiation is mainly affected by factor as cloud cover, shade, and aspect. These factors are all dependent on the 3D form of the landscape.

Dubayah and Rich (1996) state that the attributes of the terrain (elevation, slope, orientation, and shadowing) generate strong local gradients in solar radiation, creating microclimates. These microclimates influence local balances of water and energy, which determine patterns of snow melting, soil moistening, photosynthetic processing and plant growth.

Durbayan and Rich (1995) identify three sources of solar radiation on a slope: direct, diffuse, and reflected. The direct solar radiation is related with the solar angle. The diffuse solar radiation is not dependent on the solar truck; rather it depends on the percent of obstructed sky over a specific point. The reflected solar radiation depends on the albedo of the surrounding landscape (Figure 2-1).

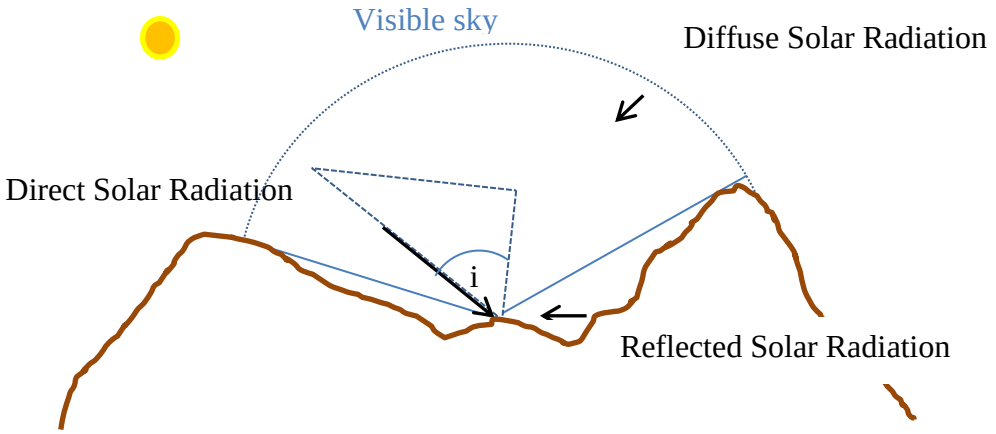

Figure 2-1 Effect of the topography on the solar radiation, adapted from Durbayan and Rich (1995)

The direct solar radiation depends on the angle (i) between the Sun's beam and the slope normal (Figure 2-1). It is maximum when i=0, or the Sun's ray hit directly in 90 degrees the slope surface. Durbayan and Rich (1995) differentiate two concepts shading and shadowing. The shading is defined on function of the solar angle (i), and express how directly the Sun hit the surface. Shading varies with the solar position in the sky (defined by a zenithal and azimuthal angle), as well as with the slope's tilt and orientation. The shadowing is independent of the solar

angle (i); it is the effect of nearby objects that obstruct the Sun's rays and cast a shadow over a specific place.

The diffuse solar radiation depends on the atmospheric components, which have effects of absorption and scattering on the sun light; the atmospheric thickness, given by the elevation above sea level; and the quantity visible sky (at the specific place). Diffuse solar radiation is considered anisotropic; it varies according to the sky angle. However, for simplicity, many models assume the same amount of diffuse solar radiation coming from all directions. Shadowing also affect the diffuse solar radiation; nearby objects that obstruct the visible.

Durbayan and Rich (1995) highlight that topographic effects on solar radiation vary according to the atmospheric conditions. Under clear sky conditions, the solar radiation map is more dependent on the direct solar radiation; and under cloudy conditions the diffuse solar radiation became more relevant in the model. Consequently, under clear sky condition the topographic factors of tilt, orientation, and shadowing have a major influence on the spatial variation. By contrast under cloudy condition, the amount of sky obstructed will dominate the resulting solar map.

Yu et al. (2009) states that in urban environments, topography drives the spatial distribution of solar radiation. On a plain terrain, all the places receive the same solar radiation, and the solar radiation varies only throughout the day and seasons. However, the presence of the buildings creates strong elevation differences in the landscape. That generates significant spatial variability of the solar radiation. This study found that, in landscapes with high elevation differences, the shadowing change quickly according to the Sun truck.

Yu et al. (2009) found that the spatial variability (of solar radiation) is maxima on zones with a dense distribution of skyscrapers. Diffuse solar radiation became more relevant in this scenario, where skyscrapers obstruct the Sun-light. This effect became extreme in winter because the solar angle is low. In contrast, in open areas (as parking lots), solar radiation has little spatial variability. In flat landscapes, direct solar radiation is the main component of the total solar radiation. In addition, this study found that the spatial variation of the Sun light generates different ecosystems, into the city, affecting plant species, distribution, and abundance.

In urban environments, according to Miller et al. (2011), spatial variation is the main factor to consider when placing solar panels, including orientation (in the north hemisphere the best location is facing south), shade (cast by neighboring features), and panel angle. Coincidently, O'Brien et al. (2010) identify building orientation and shape as the main factors influencing the amount of harvestable solar radiation.

2.1.3 Existing Approaches to Estimating Solar Radiation

According to (Miller et al., 2011) the main methods used to estimate solar energy are measuring, modeling, and remote sensing. They describe the measuring approach as the directly application of an instrument to a specific location; the data acquired in this way provide a precise representation of the energy potential, however, a dense network monitoring solar radiation would have a high cost. In addition, values measured by weather station are not continuous on the space. Suri (2006) states that measured data can be interpolated to obtain a continuous spatial dataset. However, the interpolated values have a high level of uncertainty, which rises in regions with complex high variation.

Modeling approaches

The modelling approaches are defined as a simplified representation of reality that follows a logic pattern. The main modelling approach derives solar radiation from other weather station data.

For example, Meteonorm is a database that derives continuous data sets from solar radiation data measured by weather station. It uses 3D inverse method for interpolate the data of direct and diffuse solar radiation. This database uses satellite imagery for region with low density network of weather stations (Meteotest, 2008). Almeida and Landsberg (2003) derived global radiation from net radiation data; derived from a network of automatic weather stations, in Brazil.

In addition, Bindi and Miglietta (1991) developed a model to estimate daily global radiation based on air temperature and rainfall measurements, in Italy. Coop (2000) developed a model to estimate the mean solar radiation based on the extreme monthly temperature, in USA. Angleis-Dimarkis et al. (2011) report, for locations where there are not instruments implemented, the irradiation is derived from the cloud cover and sunshine duration of the day.

The estimation of solar radiation through models is less precise than the measured solar radiation. However, the models are more affordable. In addition, there is a dense network of weather stations measuring temperature, precipitation, cloud cover and long of the day; from which is possible to estimate solar radiation.

Remote sensing approaches

Remote sensing methods do not measure directly solar radiation values; rather they model it from parameters such as elevation or satellite imagery. For example, Rigollier et al. (2004) developed the Meteosat-2 method to derive solar radiation from satellite images. This model is available through the open-source software Helisat-2. The project Heliosat2 created a long term series of solar radiation for Africa and Europe. This dataset encompasses 2004 to 2007, with a temporal resolution of 15 min and a spatial resolution of 5 km. This method has the advantage of being able to model solar radiation over large areas. In addition, Rigollier et al.(2004) state that Meteosat-2 method, using imagery over 10km resolution, can yield s more precise results than interpolated data (from weather stations that are farther apart).

Other models are based on geophysical calculations; starting with the solar constant (at the top of the atmosphere), applying reduction factors (to account for atmospheric attenuation), and using DEMs (to account for the topographic factors). LiDAR techniques offer precise and detailed 3D models, which have been basis of pioneering energy models. These models consider the spatial and temporal variation of the energy. In addition, they generate datasets continuous in the space, and are able to simulate future scenarios (Miller et al., 2011). Geographic Information Systems (GIS) have been broadly applied to model solar energy; especially in urban areas because of their ability to account for spatial variation, as well as for the energy process. According to Hofierka and Suri (2002), the GIS approach provides an affordable, fast, cost-efficient, and precise estimation of the solar radiation. In addition, GIS solar models take into account topographic factors such as: slope, orientation, and shadowing (cast by the surrounding). The accuracy of a

GIS solar radiation model depends on two main factors the quality of the algorithm and the quality of the DEMs (Yu et al., 2009), and (Kumar et al.,1997).

According to Suri and Hofierka (2004) the main factors to take into account when modelling solar radiation in GIS are: extra-terrestrial radiation, terrain characteristics, and atmospheric extinction. The extraterrestrial solar radiation depends on: Earth declination, latitude, and solar hour-angle; these factors can be accurately computed by applying astronomic formulas. The terrain characteristics depend on: elevation, slope, aspect and shadow; that can be accurately modeled from topographic data. The atmospheric attenuation is given by processes of scattering and absorption; both caused by the solids and liquids and gases in the atmosphere (including clouds). These factors involve complex interactions and are difficult to model with accuracy.

The Solar Analyst module from ArcView GIS was developed by Fu and Rich (1999). This solar model computes an angular distribution of the hemispherical view (from a specific point); it is a discrete model of the sky obstruction. A raster is computed, for a specific point, by computing the horizontal angle between the point and a set of directions; for directions outside the set, the horizon angles are interpolated, the result is similar of a fisheye photograph (Rich, 1989),(Rich 1990). As input, this model uses a DEM, which serves as basis to derive the parameters of latitude, elevation, orientation, and shadows (cast by nearby topography). In addition, the model requires setting a period of time for which the isolation variance is integrated; it considers daily and seasonal variations in the solar angle. Two atmospheric parameters are considered Tranmissivity (of the atmosphere) and Diffuse proportion (of the global normal radiation fluxes).

Suri and Hofierka (2004), created the Photovoltaic Geographic information system (PVGIS). This model interpolates solar radiation values from the European Solar Radiation Atlas through the model r.sun, which was implemented in a software open-source called GRASS GIS. The model use as input a DEM and a clear sky index to derive the direct, diffuse and reflected fraction of the solar radiation. This model can predict solar potential for photovoltaic systems considering local factors such as: different levels of tilt and the shadowing (derived from the nearby topography). This model is especially suitable for large areas with complex terrain; also due to its interpolation tools this model is especially helpful in zones with lack of ground measurements. In addition, the authors test the model r.sun in an urban environment, using a 3D city model including: DEM, topographic maps, orthomaps, building food prints and morphology maps. This analysis concluded that two third parts of the electric demand of the city of Slovakia can be covered by the use of solar energy panels. However, this potential has high spatial and temporal variation.

Summary of methods to estimate solar radiation

In summary, direct measuring is the more precise method to estimate solar radiation. However, there is an economic limit on the number of weather stations that can be equipped to this purpose. In this context, modelling approaches became increase relevant, summarise the modelling approaches presented on this section.

Table 2-1: Summary of Modelling Approaches to Measure Solar Radiation Data.

Model	Author	Input	Method to derive solar radiation	Extension
Meteonorm	Meteotest (2008)	Weather Station measurement	3D inverse distance interpolation	Global
Bindi and Miglietta	Bindi and Miglietta (1991)	Temperature and rainfall	Probabilistic	11 countries
Almeida and Landsberg	Almeida and Landsberg	Net radiation data	Probabilistic	Brazil
Coop	Coop (2000)	Extreme monthly temperature	Probabilistic	U.S.A
Meteosat-2	Rigollier (2004)	Satellite imagery	Heliosat-2	Europe
PVGIS Model	Suri and Hofierka (2004)	Weather station measurement and DEM	r.sun	Europe
Solar Analyst	Fu and Rich (1990)	DEM	Fu and Rich (1990)	U.S.A

Usually, if the stations are farther apart, interpolated values have a high level of uncertainty. However, there are dense networks of weather stations that measure other parameter such as rain fall or temperature from which solar radiation can be derived.

Solar radiation modeled from satellite imagery seems to be more precise than interpolated values (when the weather stations are farther apart more than 10km). However, the spatial resolution of the satellite image is about 5km, which is not precise enough to work at building scale.

On the other hand, GIS models are very suitable to work in urban environment. They are affordable, fast, precise, and can use LiDAR data as input (which provide very precise and high resolution 3D models). Notice that the accuracy of the model depends on quality of the DEM, as well as on the algorithm. In addition, the algorithm can start with a theoretical solar constant or

be fitted with weather station data (such as r.sun model does). Finally, GIS models are based on some assumptions and generalizations and when the spatial resolution increases, the model became more complex.

2.1.4 Related Works

Wigton et al. (2010) predict the available solar energy on the rooftops of a large area of Ontario, Canada. This study combines GIS capabilities and an object-oriented approach to extract the building outlines of the region rooftops using Feature Analyst (FA); an extension of ArcGIS. FA extracts objects from an image based on their color, size, shape, texture and orientation. This study reports FA as a very useful tool to extract building outlines. However, it describes some difficulties arising from two factors: the wide variety of rooftops in the cities and the spectral similarity between some rooftops and other land covers (such as pavement). After obtaining the total roof area, a reduction factor of 50% is applied to account for orientation, and a 30% to account for shading, pitch, and availability. The total annual energy output was estimated from the mean daily global isolation of the zone reduced by the efficiency of the panel. This study suggests that a 30% of the Ontario demand can be cover by the using PV panels.

Levinson et al. (2009) applied LiDAR data and aerial ortho-photos to assess the reduction on solar radiation caused by shadowing in four cities of California. The boundaries from roofs, trees and parcels were manually digitalised from aerial ortho-photos. The elevation raster were obtained from the LiDAR imagery and a function was applied to simulate the tree growth. The Hill-shade function of ArcGIS was applied to know if a cell was in a shaded position. This study concludes that at the south-, southeast-, and southwest –plane of the roof; the tree growth may cause a light loss between 50 and 70%; throughout a range of 30 years.

The City of San Francisco through its Department of Environment and the consultant company CH2M HILL developed the San Francisco Solar Map. This project supports people to estimate the solar potential that they could obtain by installing solar panels; promoting in this way the use of solar technologies. In addition, the web site offer information about the local PV installers, tax incentives, and permitting process; this information is addressed to house holders, multi-tenants and industrial building owners. The site provides a free solar assessment that can be accessed by typing an address. The solar potential is estimated based on the surface of the building rooftop, which is obtained from the cadastral outlines of the buildings of San Francisco. A reduction factor of 0.25 is used to account for obstructions (such as chumminess and exhaust fans), shade, tilt, and orientation. It is assumed a requirement of 9 to 18 square meters to produced one kilowatt (kW); assuming an annual solar radiation between 4.1 and 4.6 (kw/day). The cost saving assumes a tariff equal of $0.1868 per kilowatt-hour (kWh) for residential customers based on data published on February, 2010. The CO_2 reductions assume a mitigation factor of 0.29($kgCO_2$/kWh), based on data published on 2008 by the San Francisco Community-Wide. Finally, as a disclaiming, the City of San Francisco recommends verifying the information and calculus before investing (City of San Francisco, 2013).

Dr. Martina Klärle and her team carried out the research project Sun-Area at the Osnabrück University of Applied Sciences. The project carried out an automated solar cadastre from LiDAR data. The research project started at the City of Osnabrück, Germany in 2006, and included 70,000 buildings. The method estimated the potential solar energy at the level of rooftops, county, and city, taking in account local factors such as tilt, orientation and shade from vertical features such as chimneys, masts, nearby vegetation, and constructions. The outputs were the

suitable roof areas, potential power generated, levels of CO_2 reduced, and investment required. In addition, it is possible linking the cadastre to other municipal data to generate more information. This study concludes that 20% of German roofs are suitable for setting solar panels, and the power generated would be able to cover the energy demand of the houses throughout the country (Sun-Area, 2013).

The Solar Atlas of Berlin applies the algorithms developed on the Sun-Area project to create an atlas of the potential solar energy of Berlin (Ludwig and McKinley, 2010). This atlas is available online through a website, which is expected to generate a demand for solar technology, visualises the existing solar installation, estimates the solar potential of the city, and identifies the best locations in which setting solar panels. In addition, this study states that two thirds of the house power demand can be met by solar panels.

The City of Boston has implemented a project to follow the implementation of alternative energies such as wind, biomass, hydro, and solar power. This project has been implemented in a web GIS called the Renew Boston Solar Map. This project expects to help meeting the goal of reducing 20% the greenhouse emissions by 2020; by reducing the investment required for solar panels. In this way the City of Boston aims helps the citizens to save energy and money. For solar radiation, this site implements an application that allows visualising the monthly energy received by each building, total suitable roof area, potential system size, annual potential output, solar radiation (kwh/m^2), monetary saving, and potential CO_2 reductions. This estimation assumes flat roofs, a solar panel delivering 126.98 watts per square meter, and an annual panel producing 1200 kilowatt-hour. The price of the kilowatt-hour is estimated in 0.18 dollars. Finally, to estimate the reduction on greenhouse emissions, the project considers that per each

kilowatt-hour produced, the carbon dioxide will be reduced by 0.519 kg, sulfur dioxide by 1.088 kg, and nitrogen oxide by 0.498 kg (City of Boston, 2009)

2.2 Building Modeling

This section does an overview of Building modeling. It reviews the current method applied to building detection, outline extraction, building segmentation, and describes the related studies.

2.2.1 Building Detection

According to Dorninger and Pfeifer (2008), generating a 3D city model involves representing the buildings next to other urban elements such as vegetation, streets, and power lines. They divide the building model generation process into five steps: building detection, outline extraction, roof shape reconstruction, model generation, and quality analysis. However, most of the existing research work has been done on individual aspects of this process. This study especially concerns on the first two steps: building detection and outline extraction.

Building detection is the process of identifying all the points containing building information in the horizontal x-y plane. This process is often performed on a raster representing a Digital Surface Model (DSM) derived (interpolated) from the LiDAR point cloud. This two-dimensional (2D) representation of heights is called a 2.5D raster.

The difference of 2.5D raster and LiDAR data is that in the raster the x (latitude) and y (longitude) positions are implicit in the layer structure; and only the z (elevation) position is explicit as a number. In addition, in a raster the neighbours of a cell are already defined by the

layer structure. In Contrast, in the LiDAR point cloud the x, y and z position are explicit as numbers and the neighbors of a point need to be defined using an algorithm.

In the present study a 2.5D was preferred because the raster format has the advantages of reducing the amount of data, being faster to process, and being less computationally expensive. However, a 2.5D raster has some limitations representing 3D forms as caves and hanging elements because each x (latitude), y (longitude) position can represent just one z (elevation value). Other disadvantages of working with 2.5D rasters is that the resampling process introduces smoothing effects, especially on sharp surfaces (Dorninger and Pfeifer, 2008) (Maas and Volssman 1999).

Often, roughness measurements, such as local high variations, are used to separate manmade structures from vegetation. First, a normalized digital surface model (nDEM) is computed by subtracting a digital terrain model DTM (a layer that contains elevation data at ground level) from a digital surface-model DSM (layer containing elevation data form a surface including elements above the ground such as trees, power lines, and buildings). Then, high objects with low high variations are classified as buildings, and high objects with high roughness are classified as vegetation. For example Matikainen et al. (2003) classified as building all the objects higher than 2.5 m with high levels of co-occurrence (of heights). They applied this criterion, together with the homogeneity of intensity and the average length of edges. Morgan et al. (2000) detected buildings by setting a minimum area and applying a Laplacian filter to measure changes in elevation. Rutzinger et al. (2006) selected the buildings by setting a minimum object area. Then, buildings were separated from vegetation by using two criteria the difference between the first and last LiDAR pulse (assuming that objects with multiples pulses

are less likely to be building) and the standard deviation of height (assuming that constructions have lower elevation differences than vegetation).

2.2.2 Outline Extraction

Outline extraction is the generation of a polygonal boundary, called the 2D α-shape (Dorninger and Pfeifer, 2008), of all the building points. The building boundaries are defined as the intersection of the building with its surroundings. It can be obtained from cadastre sources or can be generated from the aerial image or the LiDAR point cloud data.

This study chooses to generate the building outlines from the LiDAR point cloud. That because a technique that generates the outlines can be used in any location, independent of the availability of cadastral data, and the resulting outlines would be coincident with the solar analysis that, also, was derived from the LiDAR points.

Usually, the process of building boundary generation starts by detecting a coarse estimate of the outline, after a generalization and regularization is performed (Sampath et al., 2007) (Jwa et al., 2008)

2.2.3 Building Segmentation

Segmentation is the process of segregating a digital image into multiple parts (sets of pixels) with the objective of transforming the image into something more meaningful and easier to analyze (Shapiro and Stockman, 2001).

Building segmentation decomposes the building points into planar patches and other elements. The building segmentation process defines homogeneity criteria to group similar pixels (or points). Some homogeneity criteria may be similar height, normal vector, slope, or aspect.

The present study used 2.5D grids instead of the original LiDAR points in order to reduce the complexity and to increase computational performance. The advantages of this approach are the reduction of the amount of data and the fact that in a raster the neighbours are implicitly defined by the grid representation. In contrast, the disadvantages of grid resampling are its smoothing effect, especially at sharp surfaces, and some constrains in the segmentation process, because the grid allows just one height position for each x-y position (Maas and Volssman, 1999). Segmentation using a LiDAR point cloud is suggested for a better representation of complex geometries such as caves and hanging elements (Filin and Pfeifer, 2006). However, LiDAR a point (during the segmentation process) requires explicitly defined the neighbourhoods (Filin and Pfeifer, 2005).

2.2.4 Related Works

Yu et al. (2009) used a GIS approach to quantify the impact of urban morphology (derived from high resolution LiDAR data) on the distribution of solar radiation; at the center of Houston, Texas. This study fussed LiDAR data and aerial-photograph to map the different components of the urban landscape. Object were created by segmenting the aerial image and geometric attributes derived from LiDAR data were used to support the object classification. This study implement, in ArcGIS, the equations developed by Kumar et al. (1997); in order to estimate the spatial distribution of solar radiation.

Kassner et al. (2008) used LiDAR data to carry out building detection followed by a solar energy potential analysis. The field test encompassed 13 buildings located in the University of Cologne, Germany. The study area included roofs with different levels of inclination and shapes. As primary data, the authors used a normalized digital elevation model, nDEM. Then, in order to select the buildings and eliminate incorrect-positioned points, a threshold value of 3m (selecting points at 3m or higher) was applied. From the segmented image, the buildings outlines were generated and the LiDAR point cloud was masked to this outline. As an alternative, Kassner et al. (2008) suggested the use of polygons from an official cadastral dataset to mask the LiDAR data. The filtered LiDAR points were analyzed according to the slope and were classified between flat (<10°) and sloped (10°-60°) roof areas. Flat roofs were segmented in classes according to their height; a distance of half a standard deviation was used as the inclusion margin. Sloped roofs were classified according to their slope and inclination. Slopes between 10° and 60° were classified as suitable, as well as those with an azimuthal position between 90° east and 270° west.

The main obstacles to overcame when modeling on this scale are the nDEM resolution and possible inaccuracies in the point-positions. Kassner et al. (2008) found a 1.5m wide band around the buildings where the points were misplaced (for example a point with a height value 0 located inside the building). Many of these problems were avoided by segmenting the points equal to or greater than 3m. These misplaced points make identifying the roof outlines difficult, as well as, the determining the internal limits of the roof patches. Finally, to assess the results of the analysis, Kassner et al. (2008) generated a raster layer from panchromatic stereo-photogrammetric aerial photographs (scale 1:13,000). The data were imported to GIS and rasterized.

Brandin and Hamren (2003) developed and implemented algorithms for classification of urban elements derived from LiDAR data (buildings, vegetation, power lines, posts, and roads). For building classification, they used an object-based approach, whereby the process units were not the pixels (basic unit of the raster-grid) but image objects, derived from an image segmentation process. Ideally, an object is a group of connected pixels that represent an element of the reality such as a building or a tree; however, achieving an accurate representation is not always possible. One advantage of working with objects is the possibilities to study the characteristic of the whole group instance of just the pixel characteristics. For example, man-made structures often have a rectangular shape, difference to that vegetation; this feature can be used to classify an object, but not a pixel. The disadvantage of working with objects is that sometimes is difficult to separate objects that are close to another. For example, constructions and trees that overlap each other. In addition, if the separation fails, the classification fails too.

For building classification, Brandin and Hamren (2003) derived a nDEM and set a high threshold of 2m. The trees were removed using an expanded Boolean derived from the number of echoes (LiDAR). Brandin and Hamren (2003) assumed that trees often contain multiple echoes, a difference from buildings, which have a low concentration of multiple echoes (except by the borders). In addition, small objects (less than1.5m^2) were removed because they were not likely being buildings. Finally, three decision values were computed (for each object): the Hough value, Maximum slope, and LaPlacian Slope. Later, these values were used in a neuronal network to classify the objects.

2.3 Chapter Summary

This chapter provides the current state of the art on solar radiation and building detection. Many efforts are being done on modelling solar radiation. At building scale, LiDAR techniques and GIS approaches are considered valuable resources. In addition, LiDAR data is considered very suitable to semi-automatically generate urban 3D models. The challenge of combining both to obtain accurate information at building scale has triggered this study.

CHAPTER 3 METHODS

This chapter first introduces the materials used in the research, encompassing the study area, software, imagery, and data. Then, it presents the methods used for building detection and the outlines extraction process. Next, it describes the implementation of the solar model, and its calibration through weather station data. Finally, the last section describes the method for estimate the energy retrieved by each building, the economic saving and carbon dioxide reduction.

3.1 Study Area and Datasets

This study used ArcGIS to grid the LiDAR data and derive a raster 2.5D, as well as to integrate the raster 2.5D and multispectral imagery in order to perform the building detection process. In addition, the ArcGIS tool Solar Analyst was used to carry out the solar radiation modelling; the tool was parameterized with weather station data. The software ENVI was used to carry out image filtering.

The Solar Analyst module from ArcView GIS was developed by Fu and Rich (1999). This solar model computes an angular distribution of sky obstruction. Viewsheds are computed by dividing the sky into a set of directions and determining the horizontal angle to each one producing the equivalent of a photograph in 360 degrees (Rich et al.,1999). The main parameters of the Solar Analyst are a DEM, a period of time and two atmospheric parameters.

The model uses the DEM to derive latitude, elevation, orientation, and shadows cast by nearby topography. Because the solar radiation is a flux, it needs to be measured over a period of time. This period of time considers daily and seasonal variations in the solar-angle. The atmospheric

parameters are Transmissivity and Diffuse Proportion, which account for atmospheric attenuation of the diffuse fluxes of solar radiation.

The direct solar radiation is calculated based on sunmaps, which are raster representations of the suntracks defined by the Sun's positions at different intervals throughout the day and season. The position of the sun is defined by zenith and azimuth angles, and is derived from astronomical formulae based on the latitude, day of year, and time of day. For sunmaps that encompass one day or less, penumbral effects are taken into account. This effect refers to the decreasing of the intensity of the solar radiation at the edge of shadow because of the partial obstruction of the solar disc. To account for penumbral effects, sunmaps consider the apparent size of the solar disc.

Solar Analyst calculates the global radiation for every pixel by summing direct and diffuse radiation from every region. This procedure is repeated through the topographic surface, generating isolation values for the whole scene. The solar radiation is derived from the equations proposed by Fu and Rich (1999).

3.1.1 Study Area

California is the state, from U.S.A., with the higher level of demand for PV panels. That is because its abundance of solar resources, as well as its large amount of rooftop areas to place the PV panels (Chaudari et al.,2004). The California landscape is mainly modelled by the interaction between two tectonic plates: the North American and Pacific plates. The geomorphology is marked by three main features: the Sierra Nevada, the Coast Ranges, and the Great Valley of California located between them.

These three features run from northwest to southeast, parallel to the motion of the Pacific plate. San Francisco Bay was formed by the floods caused by ice-sheets melting during the Pleistocene era. Currently, this bay is a main water outlet to the pacific, and receives the flow from the rivers Sacramento and San Joaquin Rivers, as well as the drainage from the Sierra Nevada and the Coast Range.

The City of San Francisco is located at the northern end of a peninsula on the Coast Range. This area is characterised by a steep topography that generates several microclimates over short distances. The change in the terrain drives the winds over and around the City. The elevation increases toward the south, reaching 60 m above sea level at 1.6 km inland. Dominating the city are Mount Davison (285m), Mount Sutro (280m) and South Twin (280m), as well as, several significant hills located between North to South.

According to the NOAA Technical Memorandum (NWS WR-126, 1995), the climate in San Francisco is moderated by the cool waters that surround the city and the effect of the Coast range that constrains the flow of the winds. These factors moderate the temperature, which ranges from summer to winter between 21°C to 12.7°C, reaching minimums of 7.2 °C and 4.4 °C respectively. In addition, these conditions generate fog during summer and winter seasons.

The summer is extended from May to September, with its mornings presenting overcast skies clearing by noon; however it have less than 5% of the total yearly rainfalls. The winter season encompasses from November to March. During this time, the fog is thicker than in summer, and this season contains most of the precipitation events (80% of the yearly rain). However, snow event are very rare (approximately ten occurrences in 150 years). The transition seasons of spring and fall usually have the best weather, presenting clearer and warmer days.

The study area (Figure 3-1) covers a surface of approximately 11.2 km^2 of the southwestern zone of the City of San Francisco, California. This study area was chosen because San Francisco is a city with a broad environmental conscience; from 1970, the city has gradually increasing the use solar technologies. The planning department has an easy permitting process to install PV panels and gives priority to green building projects. In addition, there are economic incentives through the California Energy Commission's Emerging Renewables to help the affording the up-front cost of panels installation. Moreover, the government offers a ten percent tax credit to the business that produces electricity through solar panels and offer a five-year accelerated depreciation of the equipment. Then despite the seasonal fog and variability of the terrain, San Francisco is a very suitable City for installing solar panels.

The boundaries of the study area are given by the coverage of the LiDAR data. It correspond mainly to an urban area, encompassing part of San Francisco Bay, the port, industrial zones, highways, bridges, high buildings, and residential housing. In addition, it is possible to find community parks, and urban vegetation.

The main highways on the area are the 101 that run from north to south and the 280 (John F. Foran) that goes from northeast to south-west, other main road is the 3rd street that goes from north to south.

Study Area San Francisco California

Figure 3-1: Study Area San Francisco California

The industrial zones are mainly concentrated near the coast (Figure 3-1). There are three sectors in which the industrial zones enter to the peninsula. The first is on the northern part of the study area; from Cesar Chavez St. (by the north) to the interception between the highways 101 and 280 (by the south), at the east is limited by the highway 101 and extended to the west until the costal line. The second is in the area of Bayview, it encompasses Hunters point, the northern lands around South Basin, and the zone of Bayview (until the high way 101). Both zones are characterised by large buildings and a lack of vegetation. The third is in the southern part of the study area.

The study area presents four main green areas: Bayview Park (at the south), and the parks: Adam Rogers, Hilltop, Heron's Head and India Basin Shorline. In addition, at the southwest corner of the study area is the Candlestick Stadium, which corresponds to a large open-air building.

The remaining sectors on the study are corresponding to residential areas composed by single detached houses and adjacent constructions (as townhouses), these zone shows a combination of small constructions and vegetation.

3.1.2 LiDAR Data

According to the metadata provided in the context of the IEEE GRSS 2012 Data Fusion Contest, the LiDAR data were acquired in June of 2010 in the context of the USGS San Francisco Coastal LiDAR project (USGS, 2010). The whole project covered an area of approximately 981 km^2; however, the data included in this study is only approximately 12km^2. The spatial reference is NAD83, UTM Zone 10N in the horizontal, and NAVD88 in the vertical.

The data are classified into the following classes: Class 1 encompasses vegetation, buildings, noise and others unclassified features; Class 2 corresponds to the ground, Class 7 is noise; Class 9 represents water, and class 10 corresponds to the ground. The extension of the data is bounded by West -122.416118, East -122.354930, North37.800935, South37.702583.

Accuracy Control: According to the metadata provided for USGS, this data were compiled to meet 2m of horizontal accuracy at a 95% of confidence level, but no test was run to check horizontal accuracy. The vertical accuracy was tested against 21 independent points, and the result was RMSEz = 0.06 m at 95% of confidence meeting the 0.09 meters required by NSSDA RMSEz. In addition, the data meet a vertical accuracy of 0.12 meters at 95% confidence for all land cover types. According with the metadata, as a primary control, three existing CGPS stations were observed (CHAB, point 181, and point 222) and used to establish the control points. These points were observed during the flight and used to control the flight missions as well as the static ground survey.

The data were collected using an aircraft platform and an instrument Optech ALTM 3100EA. The data were collected by overlapping two missions that were flown at different heights and parameters, to meet the air traffic control restrictions. The total collection required 14 missions: 10 were carried out during spring 2010 (between June 11 and June 30), and 4 missions were flown during fall 2010 (between October 19 and November 7). All of them were flown under good meteorological and GPS conditions to provide complete coverage. For every mission the GPS data accuracy was excellent, with residuals of 3cm average, and always less than 10 cm. The ellipsoidal heights were transformed to orthometric using the geoid model Geoid09, published by the National Geodetic Survey (NGS).

Every mission was corrected for residual roll pitch misalignments using TerraSolid's TerraMatch software. Then, the points were projected into the coordinate system and one LAS file was generated for each swath. In order to ensure no silvers were present, a coverage check was carried out in a project level.

Data Classification: According to the metadata provided by USGS (2010) the LiDAR point cloud was processed using TerraScan software. The process encompasses tiling the area to the project boundaries, removing outliers and classifying the points using a software routine. In the classification, first the ground points were extracted by building an iterative surface model, which had three parameters: building size, iteration angle and iteration distance. First, a moving window, of a size determined by the building size, selects the lower points (assuming these are the ground points). The low points are triangulated and the remaining points that meet the constraints of angle and distance are added to the ground model.

The total number of points recorded was 59525055. The LAS files were classified according to the American Society of Photogrammetry and remote Sensing (ASPRS) rules. A histogram of the classification point is presented in Table 3-1:

Table 3-1 LiDAR points classification code

Code	Class	Number of Points
1	Unclassified	34858493
2	Ground	21761010
7	Low Point (noise)	73827
9	Water	2821500
10	Reserved for ASPRS Definition	10225

(USGS, 2010)

The point density of the data set is 2.06 points/m^2 for all the points and 1.99 points /m^2 for the last return. The average spacing is 0.7 for all the returns and 0.71 for the last returns.

3.1.3 Satellite Data

Multispectral imagery was used to derive a Normalised Difference Vegetation Index (NDVI), which provides a criterion for the building detection process. NDVI is an excellent predictor to separate building from vegetation. It ranges from -1.0 to 1.0, with low values denoting non-vegetation and large positive values indicating vegetation. (Ünsalan and Boyer, 2011). Buildings are separated from other impervious surface (as sidewalks and roads) by using a height criterion.

The image was a World-View-2, acquired on 9 October, 2011. This image is called ortho Ready Standard Imagery, meaning that it has not any topography corrections; each pixel is mapped to the average base elevation of the satellite scene. Because of that, the image requires terrain correction to obtain the best horizontal accuracy, especially in areas of high relief (Digital Global, 2012). World View 2 has an absolute accuracy specification of 5m, excluding viewing angle and topographic displacement. This image is recommended for orthorectification. The main characteristic of the colour images are: pixel resolution of 2m, format Tiff of 16 bit depth, a spatial reference of WGS_84_UTM_zone_10, and the pixel type corresponds to unsigned integers. Table 3-2 shows the reflectance of each band in the image.

Table 3-2: World View-2 spectral bands

Band	Spectrum
B1	Coastal: 400 - 450 nm
B2	Blue: 450 - 510 nm
B3	Green: 510 - 580 nm
B4	Yellow: 585 - 625 nm
B5	Red: 630 - 690 nm
B6	Red Edge: 705 - 745 nm
B7	Near-IR1: 770 - 895 nm
B8	Near-IR2: 860 - 1040 nm

Source Digital Globe - (2012)

This image was co-registered to the DSM (derived from the LiDAR data) using four points distributed through the image. The total RMS error was 0.495969.

3.1.4 Weather Station Data

Solar radiation data from a weather station are used to parameterise the Solar Analyst tool. The National Resources Energy Laboratory (NREL) provides, through the National Solar radiation data bases (NSRDB), statistical information about solar radiation measurements from 1961 to 1990. For flat collectors, facing south, at tilt of 0, 22.62, 37.62, 52.62 and 90 degrees. Meteorological standards consider a 30 year period as adequate to establish normal values , means, and extremes. The majority of the measured solar radiation data were collected by the National Oceanic and Atmospheric Administration (NOAA) through the National Weather Service (NWS). Primary stations contain measured solar radiation data; however, the data available for San Francisco are from a secondary station. It contains solar radiation data modelled from satellite imagery and supplementary meteorological data. The METSTAT model generates most of the solar radiation data for the NSRDB. This model is based on the data measured from 1977 to 1980 by the NWS.

The weather station assigned to San Francisco California is Weather Bureau Army Navy (WBAN) number 23234. It is located at latitude 37.62, longitude 122.38, at an elevation of 5m above sea level (Figure 3-2). This is the only weather station assigned to San Francisco that contains long term solar radiation data. The station is located at approximately 10 km to the Candlestick Park, at the southern part of the study area. It is a secondary station that contains modelled solar radiation data for flat-plate collectors, facing south, and at fixed tilts.

Weather Station Assigned to San Francisco, California

(WBAN) number 23234

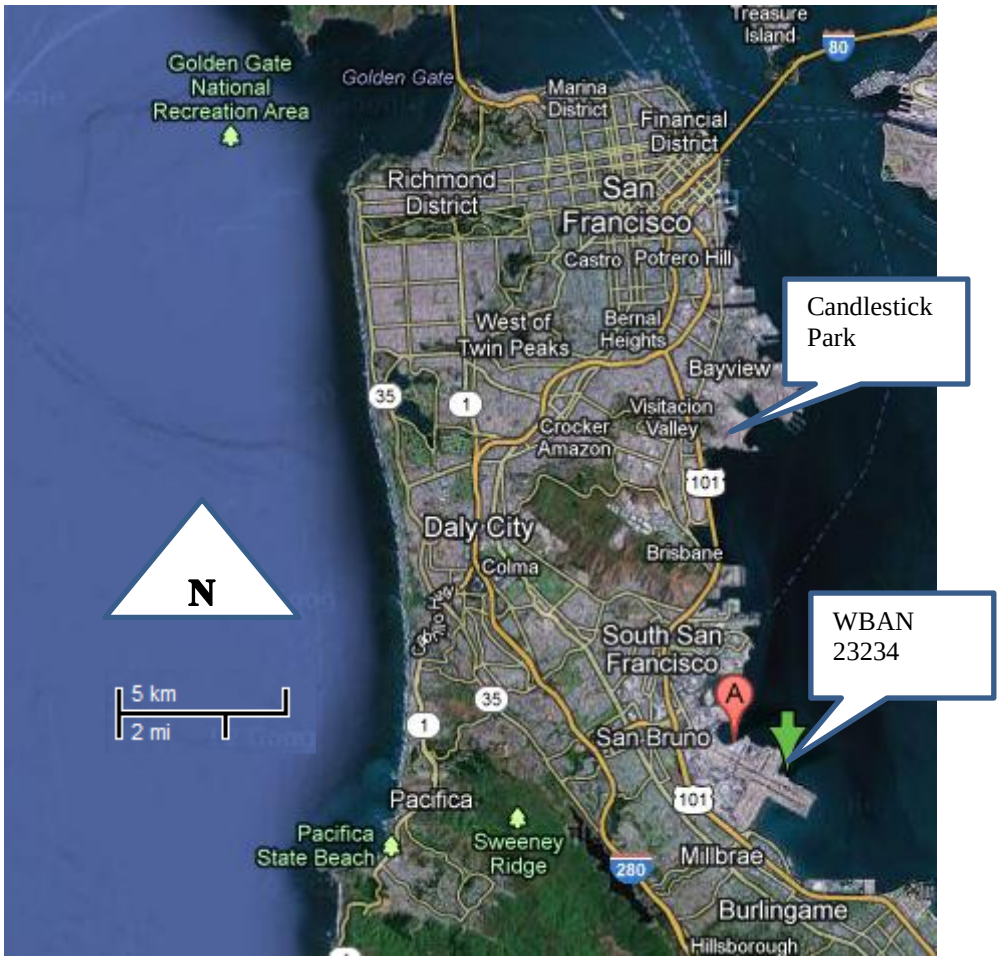

Figure 3-2: Location of the Weather Station WBAN 23234

3.2 Building Extraction

The objective of this study was to assess the proposed building extraction design, which used an object-based approach and carried out the building extraction through three different Decision Tree (DT) models. The tree models are designed to compare the effect of a segmentation using and edge detector (Sobel) and a hierarchical classification. Decision Tree One (DT1) represents the control it was carried out without Sobel segmentation and without hierarchical classification, Decision Tree Two (DT2) implemented a Sobel segmentation, and DT3 applied a hierarchical classification.

The models were fed with five criteria: height, Sobel, Normalised Difference Vegetation Index (NDVI), ratio Perimeter-Area (PA) and Area (A).

The average height value (of each object) was derived from the nDEM layer. The mean Sobel value (of the objects) was derived from an Sobel-filtered layer. The average (NDVI) was derived from a NDVI layer generated from the colour World-View2 satellite imagery. The (PA) and (A) were derived from the geometry of the 2D α-shape objects. In addition, the interaction between these predictors was tested. The methods used to derive each criterion as well as the building extraction process are shown in Figure 3-3 The explanation of each is detailed in the following sections

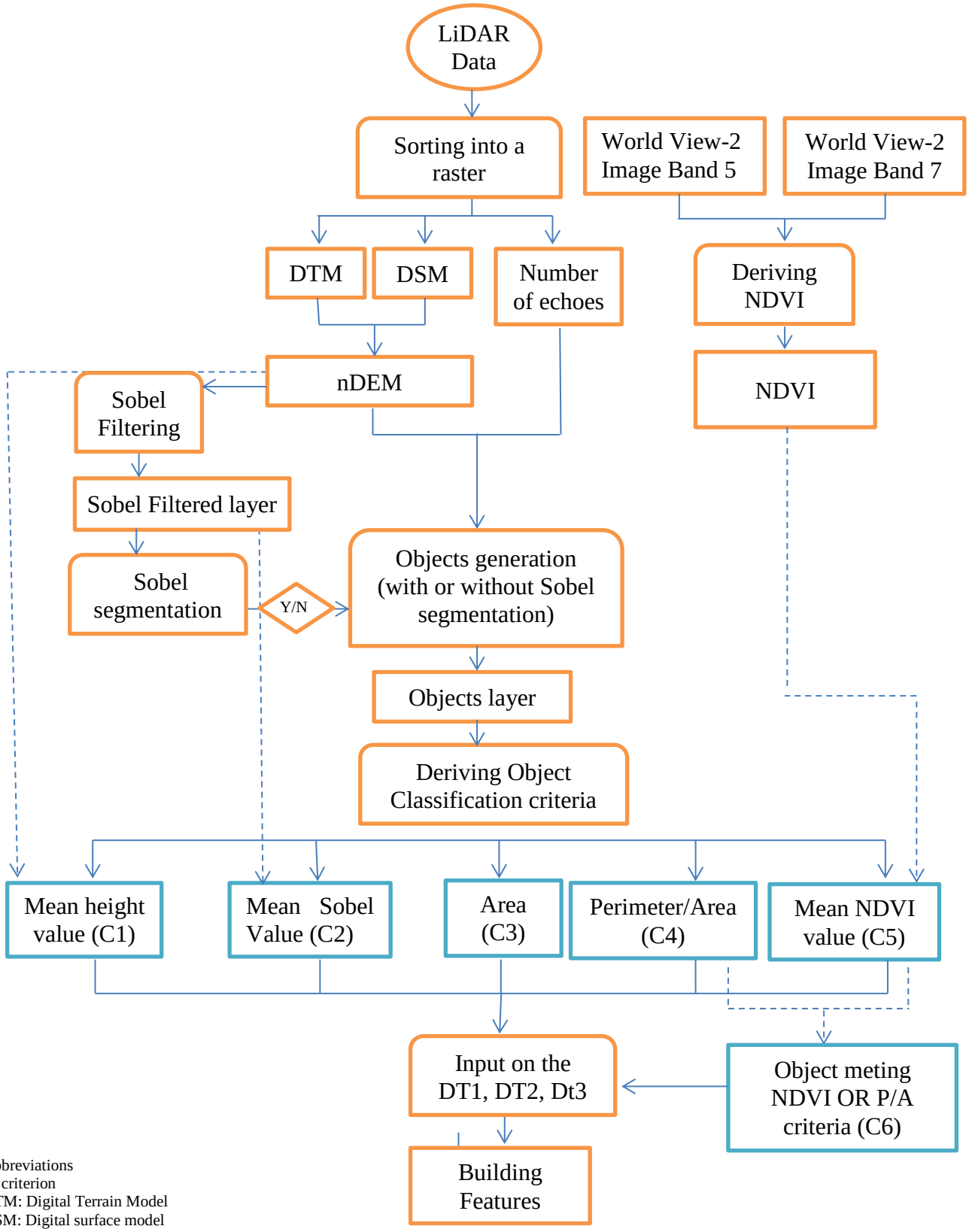

Abbreviations
C: criterion
DTM: Digital Terrain Model
DSM: Digital surface model
nDEM: normalized digital elevation model
Y/N: yes/no
DT: Decision Tree

Figure 3-3 Building feature extraction process

3.2.1Experimental Design

To analyse the factors that influence building extraction in an object-based approach, this study compares three Decision Tree (DT) models using five criteria to separate vegetation from buildings. The interaction between predictors is also examined. The combination of these factors generated fifteen treatments, as displayed in Table 3-3.

Table 3-3 Building extraction experimental design

Criteria	DT1 Control	DT2 Non-hierarchical Classification	DT3 Hierarchical classification
(C2) NDVI	T1	T11	T21
(C3) PA	T2	T12	T22
(C4) Sobel	T3	T13	T23
(C5) Area	T4	T14	T24
(C6) NDVI OR PA	T5	T15	T25
(C7) NDVI OR Sobel	T6	T16	T26
(C8) NDVI OR Area	T7	T17	T27
(C9) PAOR Sobel	T8	T18	T28
(C10) PAOR Area	T9	T19	T29
(C11) Sobel OR Area	T10	T20	T30

The three DT classification processes explore the effects of hierarchical classification and segmentation based on an edge detector Sobel filter. The Control decision tree (DT1) includes an object generation and classification process. Decision trees two (DT2) and three (DT3) include the object generation and classification process of DT1, but they add a segmentation based on Sobel filtering, followed by a second classification. The second classification, in the case of DT2, is carried out for all the objects together; and in the case of DT3, is carried out hierarchically, according to the object size.

The treatments were assessed by creating a training-dataset that encompassed a hundred observations representing building (called true positives) and a hundred observations representing vegetation (called negatives or false positives). These data were used to build Receiving Operating Characteristic (ROC) curves considering building as presences and vegetation as absences. The best criteria were determined by comparing the shape of the ROC and area under the curves. The tabulation of the cut values, of the ROC curves, helped to select the best threshold to be applied for each criterion. Finally, the results of each treatment were compared against a test-dataset that contained 300 observations representing buildings (positives) and 300 observations representing trees (negatives or false positives).

3.2.2 Object Generation

The basic object generation (Figure 3-5), used for Decision Tree One DT1, includes sorting the LiDAR data into regular grids (the raster) and segmenting it to generate groups of pixels that represent the elements on the scene. The objects were considered as the connected pixels that hold the same value, this object represent the element on the scene. The raster format was chosen because it is less time consuming and more computationally efficient. In addition, it makes the handling and analysis of the data easier.

The point cloud was sorted into two different types of Digital Elevation Model (DEM): 1) a Digital Terrain Model (DTM) that represents the ground elevation above sea level, without accounting for features on the ground such as houses, power lines or vegetation, and 2) a Digital Surface Model (DSM) that contains the point heights above sea level (including features on the ground). Then, a normalised Digital Surface Model (nDEM) was generated by subtracting the

DTM from the DSM. The nDEM layer contains the objects height above the ground (Figure 3-4).

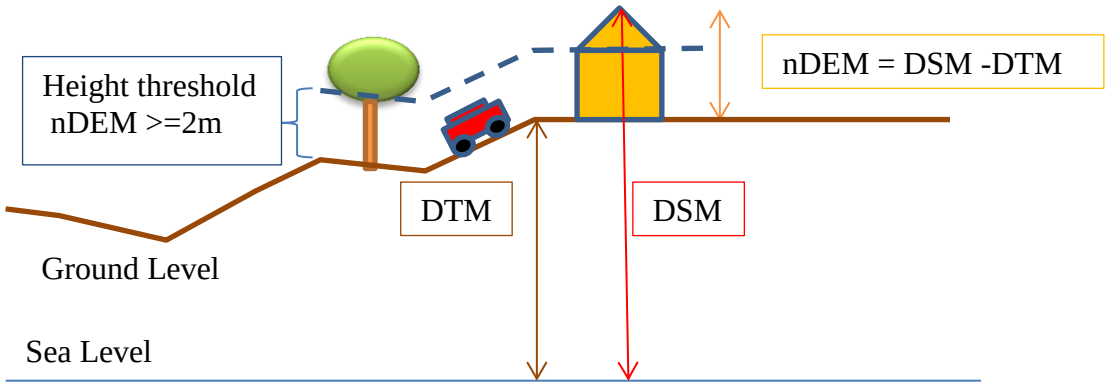

Figure 3-4 Digital Elevation Models derived from Lidar Data: DTM, DSM , and nDEM

The objects were considered as all the connected pixels that hold the same value, this objects represent the elements on the scene as buildings and vegetation.

To detect the groups of pixels representing buildings, a high threshold of 2m was applied to the nDEM, Node 6 (Figure 3-5). This value does not just separate (segment) the high objects; in addition, it removes misplaced points inside the buildings, as described Kassner et al. (2008). Two meters is a low elevation threshold for a building. It was selected empirically and it looks to include even small buildings and exclude other above-ground elements that are not relevant to the study such as cars or bushes. Other high objects as tree are excluded by other criteria.

In order to exclude most of the vegetation, a raster layer containing the number of echoes was derived from the LiDAR data, Node 3 (Figure 3-5). It is assumed that vegetated zones will return two or more echoes (because of their semitransparent nature), unlike man-made structures that

will return just one echo (because of their solid structure). This echo layer was expanded by applying a median filter Node 5 (Figure 3-5), for which a detail description is provided in the following section.

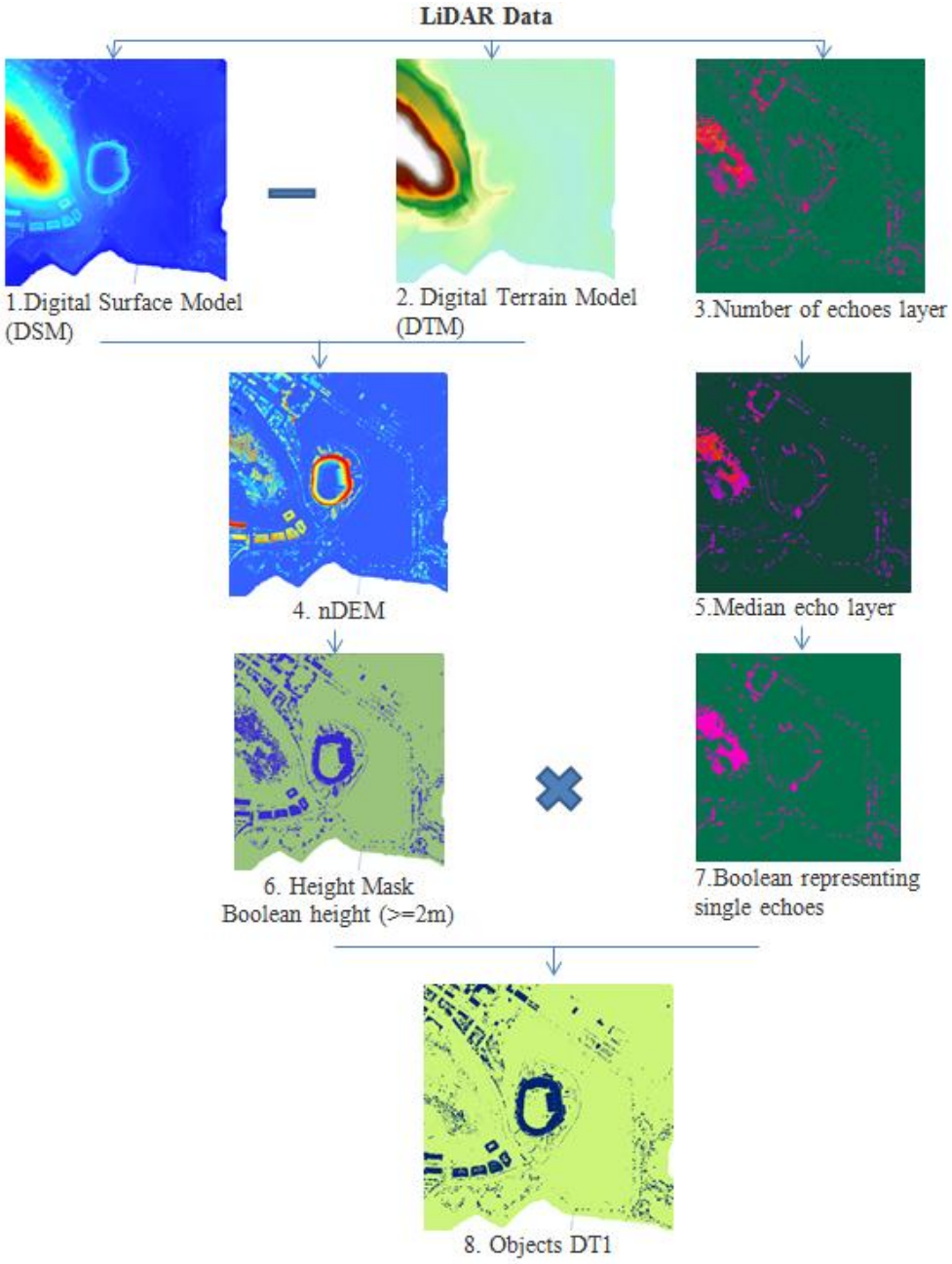

Figure 3-5: Object generation for Decision Tree One DT1

Then, a Boolean was derived from the expanded version of the echoes by classifying the pixel as 1 if it holds one echo and setting the pixel to 0 if it contains two or more echoes, Node 7 (Figure 3-5). This Boolean was multiplied by the high-mask Boolean generating the raster object, Node 8 (Figure 3-5) In the raster object value 1 represents high objects conforming to solid structures (candidates to be buildings), and value 0 represents low semitransparent objects (assumed to be ground or vegetation). Finally, an outline was generated around each group of pixels holding the same value creating polygons, 2D α shapes, representing the objects.

The outlines object generation implies the creation of polygons around each group of pixels holding the same value. When this process is carried out in a large extension, the number of groups generated may surpass the number of objects that the software can handle. Thus, in order to remove noise and reduce the number of objects in a meaningful way, a minimum size is set. If a group is smaller than $20m^2$, the polygon is dissolved into the larger neighbour. This minimum threshold area allows excluding small elements as a cars and at the same time reducing the number of objects to a number that the program can handle.

The final polygons served as object-outlines; later, statistics of the criteria Sobel, NDVI, and nDEM were computed for each object (figures of this process are presented in Appendix B). In addition, the geometric characteristics of the objects were obtained (Area and PA). These data were used to feed the Decision Tree classification methods to detect the buildings.

3.2.3 Median Filter

According to Solomon and Breckon (2011), the median filter replaces the pixel in the center of the kernel with the median of its neighbourhood (this case involved a 3x3 pixels kernel). The

median of a group of numbers is the midpoint of the sorted values. Thus, if a set of numbers is sorted in ascendant order, half of the values are over the median and the other half are under the median. The median filter is efficient in removing the so-called ‘salt and paper’ noise produced by isolated pixels. It is not computationally expensive and preserves the shape of the objects. Figure 3-6 shows an example of how the median filter works. In this case, the central pixel (value=3) is replaced by the median of the group (median= 7).

23	2	7
7	3	10
21	22	1

Sorted value =1, 2, 3, 7, 7, 10, 21, 22, 23

Number of values 9, median 5^{th} = 7

Figure 3-6 Median Filter, adapted from Solomon and Breckon (2011)

3.2.4 Sobel Filtering

A Sobel filtering process was carried out to examine its efficiency as criterion to separate vegetation and buildings. Sobel yields greater values at higher elevation differences. Then, it is assumed that vegetation objects will present greater average Sobel. That is because the semitransparent nature of vegetation implies more internal height differences. The threshold applied to Sobel, in order to separate buildings and vegetation, was select by applying an statistical analysis, which is described in a following section.

In addition, Sobel values were used to segment the objects used in Decision Tree One (DT1) and generate the objects used in Decision Tree Two (DT2) and Three (DT3). Because Sobel is an edge detector, it yields higher values on the object borders. Then, Sobel-segmentation helps

separating adjacent elements (such as adjacent constructions) or overhanging features (like vegetation hanging over nearby buildings).

Sobel is a gradient filter; it detects significant changes of the digital number from one pixel to another. It gives higher values where the local height differences are larger and lower values if the elevation difference between pixels is smaller. It is assumed that vegetation objects present higher Sobel values because of their semitransparent nature, which implies more internal elevation differences than solid structures.

This filter approximates the first derivate (Table 3-4), which represents the elevation gradient between the central pixel and its neighbours. Because a Sobel filter is isotropic, it needs to be passed in both directions (horizontal and vertical). Figure 3-7 shows the components of a Sobel filter.

Table 3-4 First derivate in x and y, continuos and discrete case.

	Continuos case	Discrete case
Df/dx	$\lim_{d\Delta x \to 0} \frac{f(x+\Delta x,y) - f((x,y)}{\Delta x}$	f(x+1,y)-f(x,y)
df/dy	$\lim_{d\Delta x \to 0} \frac{f(x, y+\Delta) - f(x,y)}{\Delta y}$	f(x,y+1) – f(x,y)

(Solomon and Breckon, 2011 pag.98)

1	2	1
0	0	0
-1	-2	-1

(a)

-1	0	1
-2	0	2
-1	0	1

(b)

Figure 3-7-(a) Sobel component for X derivate, and (b): Sobel component for y derivate (Source: Solomon and Breckon, 2011, pp.98)

To generate the objects for DT2 and DT3, Sobel filtering was applied to the nDEM, Node 1 (Figure 3-8), Sobel segmentation was carried out to separate adjacent features that are represented as a single object; this study assumes that high elevation differences represent natural limits between objects. The segmentation was accomplished by deriving a Boolean from the Sobel-filtered layer; values greater or equal to 5 were set to 0, and values smaller than 5 were set to 1, Node3 (Figure 3-8). This threshold was selected by image observation by testing different thresholds.

The Boolean derived from Sobel was multiplied by the Boolean containing the basic objects derived for DT1, Node 4 (Figure 3-8), creating a new set of objects. This segmentation is done in a separate step because, otherwise, the number of objects generated may surpass the limit of the software. Sobel segmentation was carried out only in the DT2 and DT3 classification processes (treatments T11 to T30).

Finally, outlines were created around each group of pixels holding the same value, Node 6 (Figure 3-8). The average of the criteria Sobel, NDVI, and nDEM were computed for each object and the geometric characteristics of Area and (PA) were obtained from the outlines polygons. These data were used to feed DT2 and DT3 during the building detection process.

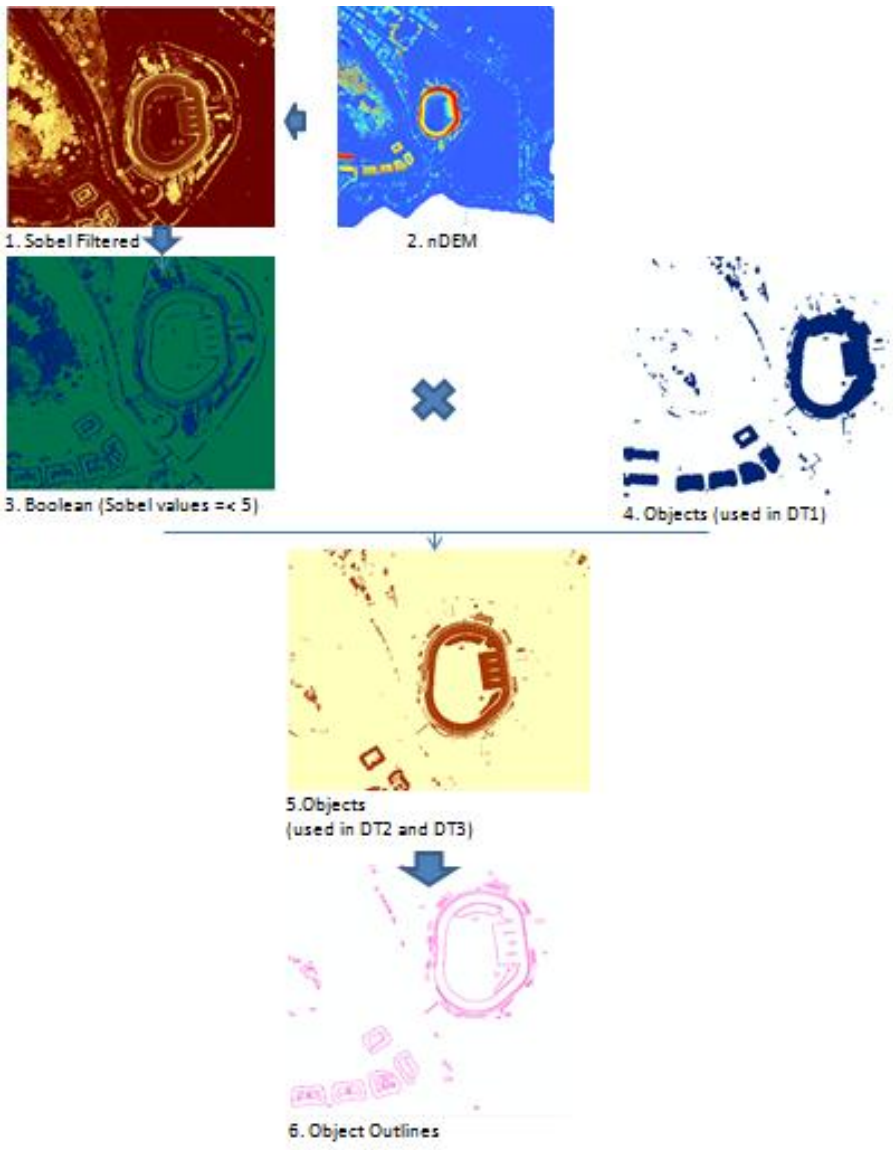

Figure 3-8: Object Generation for Decision Tree Two and Three (DT2 and DT3)

3.2.5 Deriving Normalised Difference Vegetation Index (NDVI)

The (NDVI) was assessed as criterion to separate objects representing vegetation from manmade structures. According to Ünsalan and Boyer, (2011) NDVI is regarded as one of the most effective indicators of vegetation in several applications. The NDVI ranges from -1.0 to 1.0, with

low values denoting non-vegetation and large positive values indicating vegetation; the higher the value is, and the denser the vegetation is. Notice that the objects already represent elements higher than 2m. Thus, objects classified as vegetation only represent trees excluding grass or low vegetation elements. The threshold applied to NDVI was selects applying statistical analysis to make sure it works evenly good for the whole image.

The formula proposed by Kriegler et al. (1969) was used to calculate NDVI (3-1).

$$NDVI = \frac{\lambda_{NIR} - \lambda_{RED}}{\lambda_{NIR} + \lambda_{RED}} \qquad (3\text{-}1)$$

where λ_{NIR} and λ_{RED} represent the reflectance in the near infrared and red band, respectively.

In this study, the NDVI was calculated using World View-2 image. This database set the red spectrum in Band 5 (red: 630-690nm) and the infrared in Band 7(near infrared: 770-895nm). Thus, the NDVI was calculated in ArcGIS® using (3-2)

$$NDVI = \frac{B_7 - B_5}{B_7 + B_5} \qquad (3\text{-}2)$$

where B_7 and B_5 stand for Bands 7 and 5 (Wold-View2) respectively. The NDVI layer was used to compute the average NDVI value for each object, and this mean was used to separate vegetation from man-made structures. It is assumed that objects representing vegetation have a higher NDVI than other structures.

3.2.7 Control Decision Tree DT1

Three decision tree classification processes were carried out; DT1 acts as the control and involve an object-generation and an object-classification process. DT2 and DT3 included the same object-generation and -classification than DT1. However, DT2 and DT3 added a Sobel segmentation; and DT3 include a hierarchical classification, according to the object size.

In the Control Decision Tree (DT1) building objects were detected by consecutively separating them from: the background, vegetation, and highways DT1 (Figure 3-9). In the first node (I), the background was separated from the objects by setting a mean height threshold of 2m. This threshold was set based on the image observation. Then, objects higher than 2m were classified as non-ground and objects lower than 2m were labelled as ground. After, the object outlines were created around each group of pixels. Then, the average of each criterion (Height, NDVI, PA, Area, and Sobel) was calculated for each object.

In the third node (III), five criteria (NDVI, PA, Area, Sobel and a combination of them) were tested to check their effectiveness in separating vegetation from constructions. DT1 encompasses the first ten treatments from T1 to T10 (Table 3-3).

In the fifth node (V), the highway was segregated using the criterion of Area, which threshold values were derived from the scene observation. The resulting objects serves as a base for DT2 and DT3 to refine the selection.

3.2.8 Non-hierarchical Decision Tree DT2

The Non-hierarchical classification process DT2 (Figure 3-9), starts with the same steps and cut values applied in the Control process, DT1 (Figure 3-9). However, the objects classified as man-made structures (highways and buildings) are re-segmented through a Boolean representing the Sobel values lower than 5. Then, a Non-hierarchical classification (with all the objects together) starts: at the Node 1 (Figure 3-9) separating the background from the objects by setting a mean height threshold of 2m. In the Node 3 (Figure 3-9), the highway was detected by selecting the objects intersecting the highway found in DT1 and applying a PA and Area criteria, for which cutting values were derived from the scene observation.

I Node 5 (Figure 3-9), the five criteria used to separate vegetation from buildings (NDVI, PA, Area, Sobel and a combination them) were assessed; DT2 involves ten treatments, from T11 to T20 (Table 3-3).

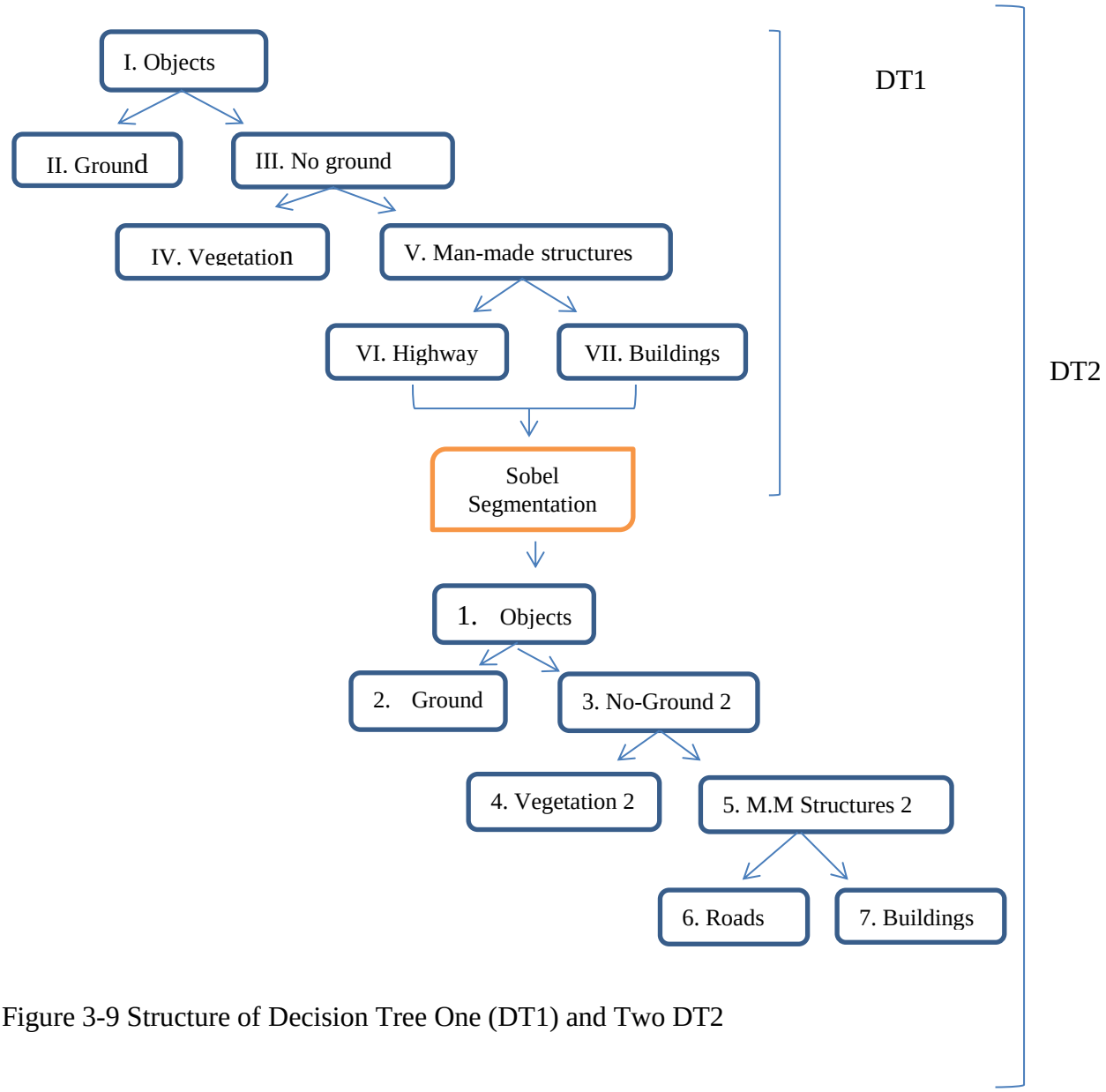

Figure 3-9 Structure of Decision Tree One (DT1) and Two DT2

3.2.9 Hierarchical Decision Tree DT3

Hierarchical classification (DT3) starts with the same steps and cut values utilised in DT1 (Nodes I, III, and V from Figure 3-10), the highways and buildings are re-segmented using the Sobel Boolean. At Node 1(Figure 3-10), the background is separated from the objects by setting a mean height threshold of 2m.

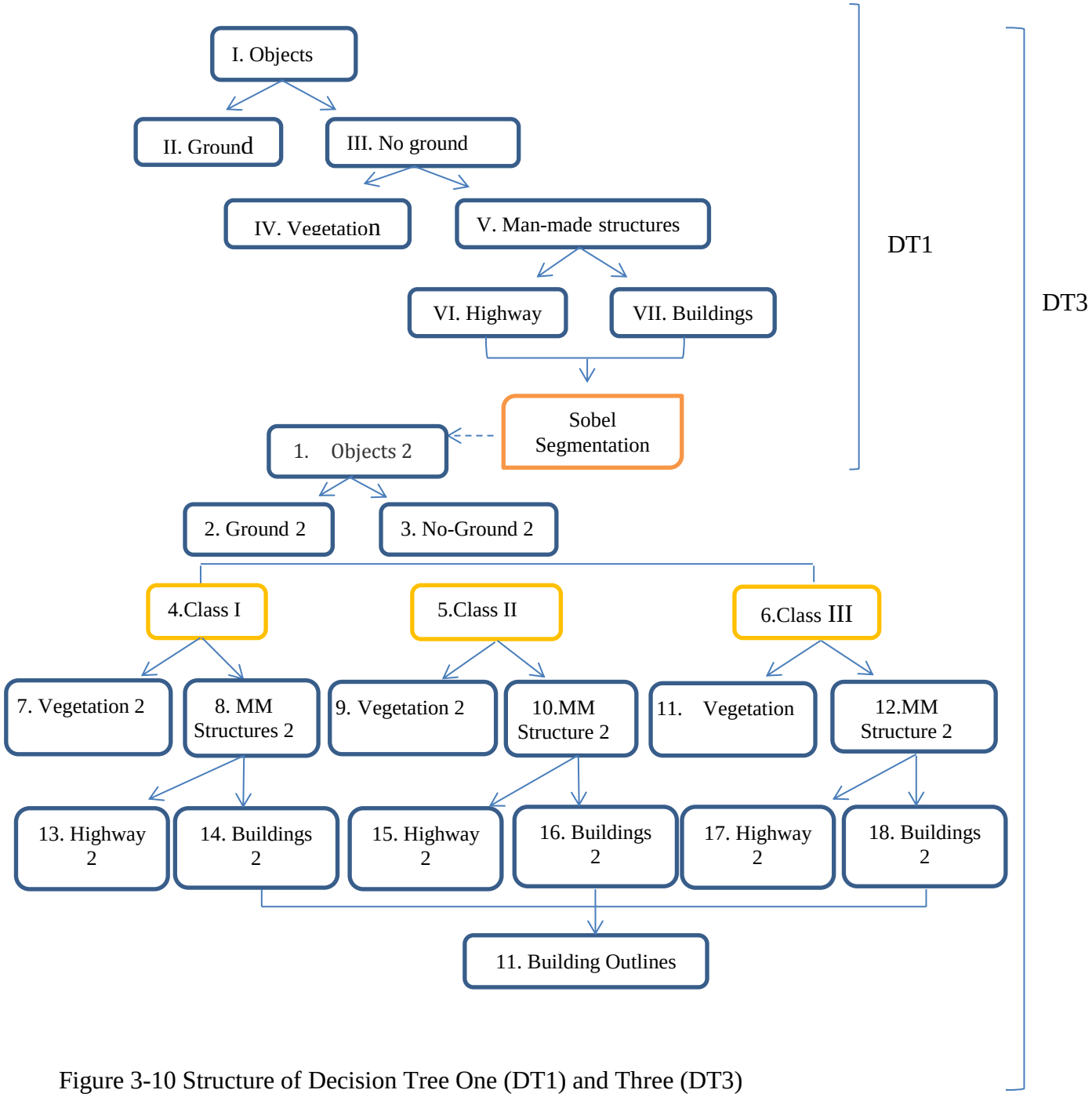

Figure 3-10 Structure of Decision Tree One (DT1) and Three (DT3)

At Node 3 (Figure 3-10) the highway was detected by selecting the objects intersecting the highway found in DT1 and applying a PA and Area criterion to refine the selection, for which cutting values were derived from the scene observation.

The objects classified as man-made structures (highways and buildings) were re-segmented through a Boolean representing the Sobel values lower than 5. Then, the objects were classified hierarchically into: Class I objects smaller than $88m^2$, Class II objects between 88 m^2 and $259m^2$, and Class III objects greater than $259m^2$. The thresholds were selected trying to find the natural brakes of the object areas. Class I corresponds to small detached constructions, which size is very similar to most of vegetation objects. Class Two are large detached buildings, which size is slightly larger than the average vegetation object. Class III correspond to adjacent constructions (as town houses) until large commercial buildings, their size is much larger than the vegetation objects.

The best threshold to separate buildings from vegetation is expected to be different for each class. Then, statistical analyses were carried out to find the best threshold values for the criteria NDVI, PA, Area, and Sobel. DT3 includes ten treatments from T21 to T30 (Table 3-3)

3.3 Solar Radiation Modelling

The solar radiation modeling is based on three assumptions 1) the weather station data represents the true solar radiation values (in field) 2) the solar panels are set in a flat position respect to the roof tilt 3) the upper two third parts of the histogram (derived from solar radiation map) represents the zones free of shade.

The solar modelling was carried out using Solar Analyst tool, from ArcGIS®. It is a solar transmission model based on latitude, local topography and atmospheric conditions. It generates a solar radiation map at landscape scale. This tool was chosen because it takes into account local variation factors such as elevation, tilt, orientation, and shade. In addition, Solar Analyst uses as input the same DSM layer that was used to generate the building model, which ensures a perfect match between the solar radiation map and the building outlines. The detailed explanation of the solar radiation model is in Fu and Rich (1999). An overview of the theory is presented as follows.

The global radiation is estimated as the sum of the direct and the diffuse solar radiation as shown in (3-3)

$$G = Dir. + Diff. \quad (3\text{-}3)$$

where G is the global radiation, Dir. Rad. is direct solar radiation and Diff. Rad. is diffuse solar radiation (Fu and Rich 1999).

First, the model generates (for each raster cell) a hemispherical raster view (in 360 degrees), similar to a fisheye photography. This layer represents the visible and obstructed sectors of the sky, Figure 3-11 (a).

A sunmap (raster layer) is generated to represent the Direct solar radiation, which arises from the Sun angle respect to a specific point (Fu & Rich, 2009). The Sun angle varies throughout the day and season tracing the Sun truck on the sky. In the sunmap, the sun track is represented as discrete sky sectors and it is specific for given latitude, Figure 3-11(b).

A skymap (raster layer) is generated to estimate the diffuse radiation. Diffuse radiation does not proceed directly from the Sun; rather it arises from each position of the sky. Then, in this raster the sky is divided into azimuthal and zenithal angles, Figure 3-11(c).

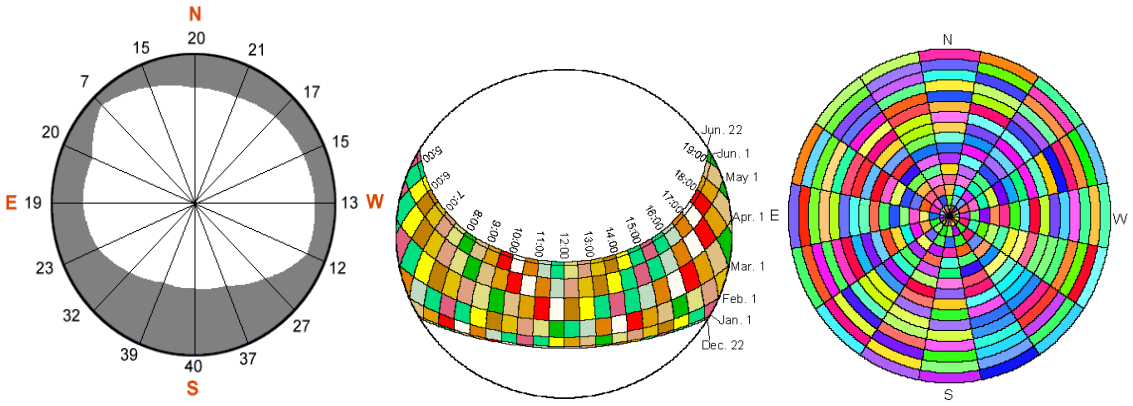

(a) (b) (c)

Figure 3-11 (a) sky obstruction of a point respect to the nearby topography, (b) Sunmap representing the Direct solar radiation at different hours of the day throughout the months June to December for a latitude of 39° (c) Skymap representing the Diffuse solar radiation coming from different sectors of the sky (Fu & Rich, 1999).

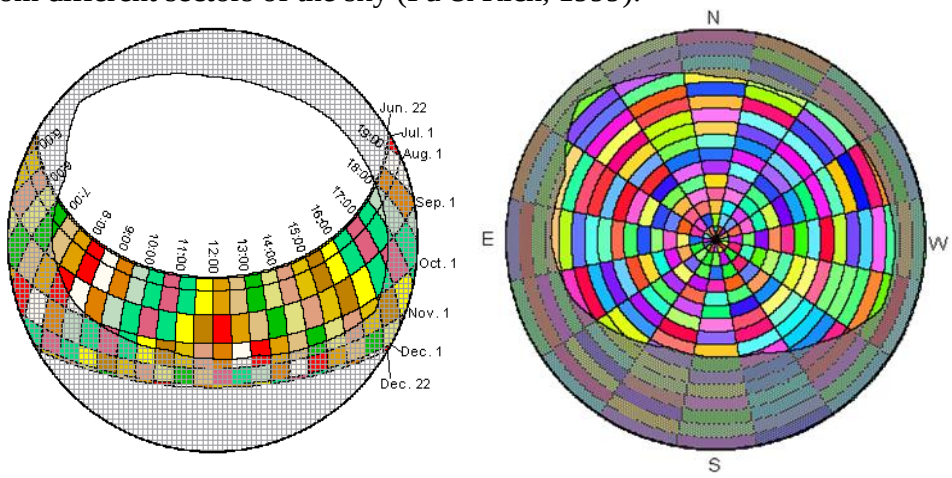

(a) (b)

Figure 3-12 (a) Viewshed overlaying sunmap (b) viewshed overlaying skymap. (Fu and Rich 1999).

The sky obstruction of a point is placed over the sunmap Figure 3-12 (a) and skymap Figure 3-12 (b). Then, the Global solar radiation is computed by summing each non obstructed cell of Direct and Diffuse solar radiation.

Parameterizing the Solar Analyst

This study used LiDAR data to derive the DSM (raster) to feed the Solar Analyst. This tool derives the initial amount of solar radiation (at the top of the atmosphere) from the latitude, which is taken from the DSM (37.5° North). The slope and aspect also are obtained from the DSM and account for shading, orientation and tilt effects. The parameters set for the study were: sky size, period of time, interval of time throughout the day, number of azimuthal and zenith angles, and atmospheric parameters.

The sky size is the resolution of the rasters representing the sky obstruction, as well as the Direct and Diffuse solar radiation. The sky size was set to 200 cells, which correspond to the default value. The period of time, for which the solar radiation is integrated, was set to one year at monthly intervals. The interval of time throughout the day was modeled at half hour. The sky map was divided into 8 azimuthal and zenithal angles using the uniform overcast model (considering the same Diffuse solar radiation coming from each sky sector).

The atmospheric parameters should be set according to local atmospheric conditions. There are two atmospheric parameters Diffuse proportion and Trasmittivity. They depend on the temperature, humidity and atmospheric composition. Even though they have a major influence on the resulting solar radiation, are difficult to estimate from classic atmospheric data. Then, the atmospheric parameters were calibrated on a number of sample sites as is described in the following section.

3.3.1 Calibration Samples

In order to calibrate the solar radiation model, a number of sample sites were collected under shade-free and slope zero conditions. However, to estimate the number of sites, the variability of the solar radiation is assessed at different tilts. This requires finding places with similar conditions to those of the solar collectors, including locations that were shade-free, facing south, and with slopes corresponding to the tilt of the solar collectors (0, 22, 37, 52, and 90). Because these exact slopes were not found in the scene, the closest tilts were selected (0, 19, 26, 35, 38, 51, 54, and 89).

In order to find the places in the image that correspond to the solar collectors, the Arc GIS tools Slope and Aspect were used to locate the appropriated tilt-types and orientation, respectively.

The shade-free condition is estimated by running the Solar Analyst tool using the default atmospheric parameters. Then, image histograms are built and the upper two third parts of the histogram picks were considered shade-free (according to the third assumption of this solar modelling).

In order to select the threshold, for the shade-free regions, statistical parameters such as the median and the mean were considered, however, these parameters were discarded because these are central measurements, and the segmentation is looking for extremely high value. Then, a more sophisticated approach was taken; an image histogram was created and the threshold was found by analysing its shape. The objective of the threshold is selecting the area shade-free that retrieve the highest amount of energy; including as many pixels as possible. Then, because the peak of the histogram is located among the higher values, the threshold was set, by image observation, at the initial two third parts of the peak.

The image statistic of the shade-free places, at specific tilts and aspect were used to estimate the number of sample through (3-4) assuming a normal distribution and with a 99% of confidence level.

$$n = \left[\frac{2.57 \times \sigma}{0.01 \times \mu}\right]^2 \qquad (3\text{-}4)$$

where n is the number of samples, μ is the mean of the population, σ is the standard deviation of the population. This equation was derived from the Central Limit Theorem, which states that for a standard normal distribution, the 99% confidence interval for the population mean is given by the expression (3-5)

$$0.99\ \mu = X +/- Z\sigma/\sqrt{n} \qquad (3\text{-}5)$$

where X is the mean of the sample and Z is the value from the standard normal distribution for the selected confidence level (for 99% of confidence level Z=2.57). Then the variability that corresponds to 1% of the population mean, which is given by (3-6)

$$0.01\ \mu = Z\ \sigma/\sqrt{n} \qquad (3\text{-}6)$$

3.3.2 Model Calibration

In order to adjust the atmospheric parameters to the local conditions, all the possible combinations of Trasmittivity and Diffuse proportion were run, generating 100 (Table 3-5). Both atmospheric parameters can takes values from 0 to 1. The default values for Transmittivity and Diffuse are 0.5 and 0.3, both for conditions of generally clear sky. The sensibility was tested

at interval of 0.1 to assess how much vary the resulting solar radiation vary when the parameter increase in 0.1 units.

Table 3-5 Atmospheric calibration experimental design

Diffuse Proportion	Atmospheric Trasmittivity									
	0.1	0.2	0.3	0.4	0.5	0.6	0.7	0.8	0.9	1.0
0.1	T1	T2	T3	T4	T5	T6	T7	T8	T9	T10
0.2	T11	T12	T13	T14	T15	T16	T17	T18	T19	T20
0.3	T21	T22	T23	T24	T25	T26	T27	T28	T29	T30
0.4	T31	T32	T33	T34	T35	T36	T37	T38	T39	T40
0.5	T41	T42	T43	T44	T45	T46	T47	T48	T49	T50
0.6	T51	T52	T53	T54	T55	T56	T57	T58	T59	T60
0.7	T61	T62	T63	T64	T65	T66	T67	T68	T69	T70
0.8	T71	T72	T73	T74	T75	T76	T77	T78	T79	T80
0.9	T81	T82	T83	T84	T85	T86	T87	T88	T89	T90
1.0	T91	T92	T93	T94	T95	T96	T97	T98	T99	T100

The treatments were run on sample sites taken in place shade-free and tilt 0. These conditions are similar to the solar collectors, on the weather station. In this form the modeled values can be compared to the values measured at the weather station. The treatment that yielded the closer solar radiation to the value measured on the weather station was run in the full scene.

3.3.3Model Assessment

The selected treatment was run on the full scene, and the resulting solar radiation map was compared with the weather station data measured by solar collectors.

The characteristic of the solar collector plate are: flat plate, shade free, facing south with tilts of 0, 22, 37, 52, and 90 degrees. Then, in the image, places with similar condition were found and the solar radiation values from the image were compared to the values measured at the weather station.

Assuming that the value measured at the weather station represents the real solar radiation , the errors of the model were estimated as the difference between the modeled and measured values.

3.4 Estimations at Building Scale

This section encompasses four parts: the first proposes a methodology to estimate the energy harvested by each building in the study area; the second part estimates the CO_2 reduction that each building can achieve by producing energy through solar panels; the third section estimates the economic savings derived from the energy production of each building, and the last estimates the hourly energy production by buildings.

3.4.1 Energy Harvested by Each Building

The solar radiation harvested by every building was estimated based on the building outlines, obtained through the best Decision Tree classification method, and the solar radiation map, obtained through the best atmospheric calibration.

To define suitable areas in which install Photovoltaic panels, two conditions were required: the area should be large enough to support a solar panel and be highly efficient retrieving solar radiation. An area greater than $4m^2$ is considered large enough to support a solar panel, assuming a Photovoltaic (PV) size of $2.25m^2$ and a 65% area available for solar panels). This study considered the 100% of the roof material appropriated to install PV panels. In addition, it was assumed most of the roof shapes are square and the tendency would be locate the panels on the center of the available space. The most efficient areas to install solar panels on were defined by masking the solar map by the building outlines, thus, generating an image that represents the

solar energy captured by the building roofs. Then, an image histogram was built and the values belonging to the upper two third parts of the histogram pick are considered highly efficient.

Only values greater than a two third parts of the histogram pick and belonging to areas larger than $4m^2$ are consider suitable for placing a Photovoltaic panel.

The solar potential of each suitable area is computed through an adaptation of the equations defined by Bernasco and Asinari (2012) and Chaudhari et al. (2004). It involves the following factors:

1) The module coverage (MC), estimated at 65%, which reduces the available area to account for the space required between solar panels, and for access and wires installation.
2) The module efficiency (ME), which depends on the Photovoltaic technology used.The efficiency generally ranges from 6%, for thin film, to 15% for mono-crystalline silicon. This study considered an intermediate value of 12% that corresponds to poly-crystalline silicon.
3) The atmospheric efficiency (AE), estimated at 90%, also considers loses of efficiency due to changes in temperature and irradiance.
4) The installation efficiency (IE), estimated at 84% considers loses in the whole PV system such as from beam reflectance, dust covering the solar panels, and inverter efficiency.

The solar potential of the area was calculated by (3-7)

$$\text{Solar Potential of the Area} = M\ (wh/m^2 day) \times S\ (m^2) \times 65\% \times 12\% \times 90\% \times 84\% \quad (3\text{-}7)$$

where M represents the mean solar radiation (in the area) and S is the surface of the area.

The solar potential of each building was calculated by summing the energy generated by all the areas inside the building (3-8)

$$Solar\ Potential\ of\ the\ Building = \sum_{n=1}^{\infty} (\ Solar\ Potential\ of\ the\ Area_n)$$

(3-8)

3.4.2 Reductions of CO_2 Emissions

This section estimates the reduction on CO_2 emissions that every building can achieve by harvesting energy through PV. Estimations were based on comparing the CO_2 realised to the atmosphere with the PV system in place with the CO2 produced to generate the same amount of energy by burning fossil fuels. This amount was estimated in accordance tothe data published by the U.S. Energy Information Administration (EIA) from USA summarised in Table 3-6.

Table 3-6 CO_2 released to generate a 1 kwh by burning different fossil fuel

Fuel Type	Pound CO_2	Kg CO_2
Coal	2.117	0.960255111
Petroleum	1.915	0.868629446
Gas	1.314	0.596020414
Other fuels	1.378	0.625050327
Average	1.350	0.61234974

Source: U.S. Energy Information Administration (2012)

As show in Table 3-6, the amount of CO_2 realised to the atmosphere varies in relation to the types of fuel burned. This study takes an average (0.61 kgCO_2/kwh) to estimate annual reduction of CO_2 emissions that every building produces, through (3-9):

Annual Reductions on CO_2 (Kg) = Energy (kwh/year) x 0.61(Kg CO_2/kw)

(3-9)

3.4.3 Cost Saving

The buildings can save costs by producing their own electricity instead of buying it from a local distributor. This cost are estimated based on information realised for the Bureau of Labor Statistics (BLS), from the U.S. Department of Labour (2013), which indicates that the average price of the kwh measured from December 2011 to December 2012 was $0.203 dollars. Then the annual cost saving derived from harvesting energy is estimated by (3-10):

Annual Cost Saves ($) = Energy harvested (kwh/year)*0.203$/kwh

(3-10)

3.4.4 Distribution of daytime energy Harvesting

Finally, as a first approach to an analysis of the distribution of the daytime solar energy, sixteen buildings were selected as subject of Solar Analyst tool. The analysis was carried out using the 15^{th} day of every month, at daily intervals of one hour, utilising the atmospheric parameter selected in the model calibration section.

3.5 Chapter Summary

This chapter presents the information of the study area and describes the data used on this study. Next, it explains the methodology utilised to carry out the building detection, solar modelling and the estimations at building scale.

CHAPTER 4 RESULTS

This chapter is divided into three main sections. The first offers the results of building-detection processes carried out through the three decision trees (described in Chapter 3). The second section presents the results of the solar radiation modelling. Finally, the third part presents the estimations at building scale.

4.1 Results of Building Detection

The results of the building-detection processes are divided into four sections, one for each Decision Tree and a comparison between decision tree classification methods.

Each decision tree presents classification results and statistical analysis. The statistical analyses are applied to find the best predictors and thresholds to separate vegetation from buildings. The statistics analysis includes: descriptive statistics, Receiver Operator Characteristic (ROC) curves, selection of a criteria and threshold, and a cross validation of the results.

4.1.1. Results of Control Decision Tree DT1

The first decision tree (DT1) corresponds to the control. The classification results obtained by DT1 are disclosed in Table 4-1. A threshold of 2m height separates ground from non-ground, which means the objects higher than 2m such as buildings, trees, or highways are classified as non- ground, and elements shorter than 2m such as cars, bushes, or street are classified as ground. Two meter is a low threshold that looks to include all kind of constructions.

NDVI is higher for vegetation than for others land covers, usually, pixels representing vegetation have a value higher than 0.3. However at object level the best threshold (found by

statistical analysis) is 0.25. Then, objects with average NDVI higher than 0.25 are classified as vegetation; and objects with average NDVI lower than 0.25 are classified as man-made structures. Notice that street, bare soil and other impervious that present low NDVI values were already separated as ground. Then, the objects higher than 2m and with NDVI lower than 0.25 are mainly buildings, however, also there are some highways.

The relationship Perimeter Area (PA) is usually higher for vegetation because natural elements usually are less compact and regular in their borders. The best threshold (find through statistical analysis) is 0.67. Then, objects with PA higher than 0.67 are classified as vegetation, and objects with PA lower than 0.67 are classified as man-made structures. The highways were classified as the objects with areas larger than 52000m^2 (by image observation); highways are separated from buildings because they are not suitable to places to locate solar panels.

Table 4-1 Classification Results DT1

Node	Object Class	Number of Objects	Criteria of selection	Method of threshold selection
I	Objects	5933		
II	Ground	180	Height < 2m	Image Observation
III	Non-Ground	5753	Height > 2m	Image Observation
IV	Vegetation	1784	NDVI > 0.25 AND PA > 0.67	Statistical Analysis
V	Man-made Structures	3969	NDVI < 0.25 OR PA<0.67	Statistical Analysis
VI	Roads	2	Area >52000m^2	Image Observation
VII	Buildings	3967	Area <52000m^2	Image Observation

Descriptive Statistics DT1

In order to separate vegetation from man-made structures, in Node III (Figure 3-9), training- and test-datasets were built; Table 4-2 presents the descriptive statistics for both. The training-dataset

encompasses 100 observations for building presence (Presence=1) and 100 for building absence (presence =0). The test dataset includes 295 observations for presence and 300 for absence. Remember that a value of 0 means not only the absence of buildings; but also the presence of vegetation.

In both training and test- datasets, a building presence (1) had a lower mean for NDVI, Sobel and PA than building absence (0). That is because of NDVI is characteristically lower for man-made structures than for vegetation. Sobel is typically lower for constructions than for vegetation (because buildings present fewer internal elevation differences). The relationship perimeter-area (PA) is supposed to be lower when objects are more compact and regular in their limits, as buildings are compared to vegetation. Finally, the mean Area tends to be higher in the presence of buildings (1) than in their absence (0).

Table 4-2 Group statistics for training- and test-datasets for DT1 (measured based on number of observations)

	Training Dataset for DT1					Test Dataset for DT1			
	Pres /Abs	N	Mean	Std. Deviation		Pres/ Abs	N	Mean	Std. Deviation
NDVI	1	100	0.05	0.07	NDVI	1	295	0.07	0.09
	0	100	0.37	0.19		0	300	0.35	0.22
P/A	1	100	0.36	0.14	P/A	1	295	0.45	0.15
	0	100	0.79	0.25		0	300	0.92	0.34
Sobel	1	100	5.45	2.09	Sobel	1	295	5.97	1.84
	0	100	8.48	3.74		0	300	8.35	3.83
Area	1	100	1592.54	2720.34	Area	1	295	1016.51	4188.76
	0	100	925.13	6137.65		0	300	519.87	3622.91

N: number of observation; Pres= presences; Abs= absences

Table 4-3 shows the results of an independent samples t-test: the criteria NDVI, PA, and Sobel meet the assumption of the t-test; that is the groups had the same variance. In addition, the means

of these criteria are significantly different between presences (1) and absences (0). These results indicate them as suitable criteria to distinguish between vegetation and man-made structures. In contrast, the Area criterion did not meet the condition of having equal variance; in addition, the mean of the Area was not significantly different (between presences and absences), indicating that is not an appropriate criterion to distinguish between constructions and plants.

Table 4-3 T-test for independent samples training dataset DT1

	EVA	Levene's Test for Equality of Variances		t-test for Equality of Means					Confidence Interval of the Difference	
		F	Sig.	t	df	Sig. (2 -tailed)	Mean Difference	Std. Error Difference	95% Lower	95% Upper
NDVI	yes	95.68	0.00	-15.55	198.00	0.00	-0.31	0.02	-0.35	-0.27
	no			-15.55	128.68	0.00	-0.31	0.02	-0.35	-0.27
Sobel	yes	28.84	0.00	-7.08	198.00	0.00	-3.03	0.43	-3.88	-2.19
	no			-7.08	155.58	0.00	-3.03	0.43	-3.88	-2.19
Area	yes	0.28	0.60	0.99	198.00	0.32	667.40	671.35	-656.5	1991.31
	no			0.99	136.45	0.32	667.40	671.35	-660.1	1995.00
PA	yes	25.30	0.00	-14.96	198.00	0.00	-0.43	0.03	-0.48	-0.37
	no			-14.96	151.46	0.00	-0.43	0.03	-0.48	-0.37

Variance Significance < 0.05 indicates the groups' variance is not significantly different and the assumption of the test is met.
Mean significance <0.05 indicates the group mean is significantly different and the criterion is suitable to distinguish between presence and absence group.
EVA=Equal variances assumed

Receiver Operator Characteristic (ROC) Curves of DT1

The training-dataset was used to build ROC curves and select the cut points for the criteria: NDVI, PA, Sobel, and Area. In the ROC curves, the sensitivity represents the rate of true positive results (the presence of buildings), and one minus specificity represents the number of false positive (vegetation classified as buildings). The best predictors should maximise the selection of positives and minimise the selection of false positives.

In Figure 4-1 the shape-curves suggest that, at this level of segmentation, the best predictors are PA and NDVI and the worse is Sobel. The area under the curve is also an indicator of the validity of a predictor model; the larger area under the curve belongs to PA (0.93%), followed by NDVI (0.91%), Area (0.85%) and finally Sobel (0.75%).

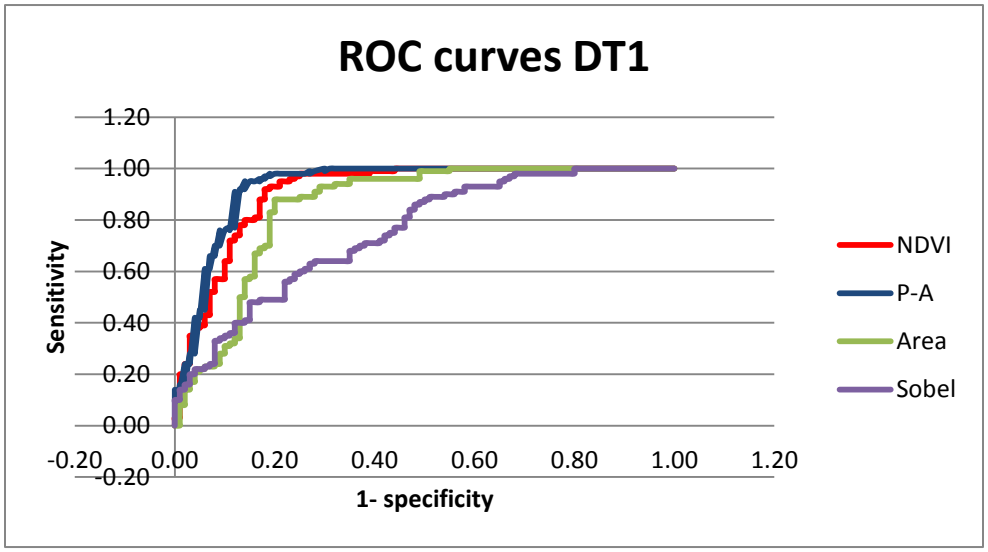

Figure 4-1 ROC curves for NDVI, PA, Sobel and Area for DT1

Because this study is intended to detect the maximum number of buildings, the cut values were selected to maximise the sensitivity, while keeping a reasonable percent of false positives (likely less than 30% for each individual criterion).

Selection of Criteria and Thresholds for DT1

The selected cut points, comparing individual criteria (T1 to T4), are shown in Table 4-4. The best result in the training dataset is obtained by PA (with a 100% of buildings detected and 30% false positives) followed by NDVI (with 98% of buildings detected and 25% false positives).

The combined criteria (T5 to T10) use the logic operation OR, which represents the union of two criteria. The combined treatments detected 100% of the building presences; however, the number of false positives raise compared to the result of each individual treatments.

T5 (NDVI OR PA) was selected to be used in Node III (Figure 3-9) because it combines the two criteria with better individual performance. In addition, these variables are very independent from each other; NDVI is derived from the object reflectance and PA from the object geometry. The combination of both increases the efficiency of the results.

Table 4-4 Selected cut point for treatment T1 to T10, training dataset

Treatment	Criteria	Cut Value	Sensitivity (true positives)	1-Specificity (false positive)
T1	NDVI	(<0.25)	0.98	0.25
T2	PA	(<0.675)	1	0.3
T3	Sobel	(<7.71)	0.89	0.51
T4	Area	(>102)	0.97	0.49
T5	NDVI or PA	(*)	1	0.42
T6	NDVI or Sobel	(*)	1	0.62
T7	NDVI or Area	(*)	1	0.56
T8	PA or Sobel	(*)	1	0.62
T9	PAor Area	(*)	1	0.51
T10	Sobel or Area	(*)	1	0.72

(*) The combined treatments keep the individual cut values presented in individual treatments.

Cross Validation DT1

In order to verify if the thresholds found in the training-dataset are valid for a larger dataset the cut values were applied to a test-dataset (group-statistics are provided in Table 4-5)

Table 4-5 presents the results of the independent sample t-test for the test-dataset. The numbers identify NDVI, Sobel and PA as suitable criteria to distinguish between vegetation and man-

made structures because they met the assumption of equal variance and their means are significantly different. In contrast, the mean Area do not show meaningful differences between groups (presence and absence), nor it met the assumption of having the same variance.

Table 4-5 T-test for independent samples test-dataset DT1

	EVA	Levene's Test for Equality of Variances		t-test for Equality of Means					Confidence Interval of the Difference	
		F	Sig.	t	df	Sig. (2 -tailed)	Mean Difference	Std. Error Difference	95% Lower	95% Upper
NDVI	yes	296.8	0.00	-20.59	593.00	0.00	-0.28	0.01	-0.31	-0.26
	no			-20.71	400.46	0.00	-0.28	0.01	-0.31	-0.26
Sobel	yes	86.08	0.00	-9.65	593.00	0.00	-2.38	0.25	-2.87	-1.90
	no			-9.70	431.39	0.00	-2.38	0.25	-2.86	-1.90
Area	yes	1.54	0.22	1.55	593.00	0.12	496.64	320.90	-133.60	1126.89
	no			1.55	578.06	0.12	496.64	321.29	-134.40	1127.68
PA	yes	126.6	0.00	-22.04	593.00	0.00	-0.47	0.02	-0.52	-0.43
	no			-22.17	416.07	0.00	-0.47	0.02	-0.52	-0.43

Variance Significance < 0.05 indicates the groups' variance is not significantly different and the assumption of the test is met. Mean significance <0.05 indicates the group's mean is significantly different and the criterion is suitable to distinguish between presences and absences. EVA=Equal variances assumed

Cross validation (Table 4-6) illustrates the results of the selected cut values applied to a test-dataset. The individual criteria (T1 to T4) that obtain better results are NDVI and PA, both with 94% of true positives detected and 34% and 21% of false positive, respectively. In the combined treatment (T5 to T10), the best results are obtained by T7 (NDVI or Area) and T5 (NDVI or PA). T7 can be discarded because of the poor performance of Area criterion in the independent samples t-test. Coincident with the training-dataset, T5 appears as the best treatment because it detects 100% of the building presences and combines the two criteria that had the better individual results, NDVI and PA.

Table 4-6 Cross validation of the cut values for treatments from T1 to T10 on the test-datasets

Treatment	Criteria	Cut Value	Sensitivity (true positives)	1-Specificity (false positive)
T1	NDVI	(<0.25)	0.94	0.34
T2	PA	(<0.675)	0.94	0.21
T3	Sobel	(<7.71)	0.85	0.52
T4	Area	(>102)	0.92	0.34
T5	NDVI or PA	(*)	1.00	0.44
T6	NDVI or Sobel	(*)	0.99	0.67
T7	NDVI or Area	(*)	1.00	0.52
T8	PA or Sobel	(*)	0.99	0.57
T9	PAor Area	(*)	0.95	0.36
T10	Sobel or Area	(*)	0.99	0.63
(*) The combined treatments keep the individual cut values presented in individual treatments.				

4.1.2 Results of Decision Tree Two (DT2)

The second decision tree (DT2) starts identically to DT1, and then obtains identical results from Node I to VII (Figure 3-9). After the Sobel segmentation 80288 objects are created, and then, the objects smaller than 20m^2 are merged into the larger neighbours remaining 5845 objects. The classification results obtained by DT2 from node 1 to node 7 (Figure 3-9) are disclosed in Table 4-7.

Table 4-7 Classification result of DT2

Node	Object Class	Number of Objects	Criteria of selection	Method of threshold selection
1	Objects	5845		
2	Ground	19	Height<2m	Image Observation
3	Non-Ground	5826	Height>2m	Image Observation
4	Vegetation	524	NDVI >0.202 AND PA>0.81	Statistical Analysis
5	MM Structures	5302	NDVI <0.202 OR PA<0.81	Statistical Analysis
6	Roads	8	(hwy =1) and height (>8.5m) and Area (>179m^2)	Image Observation
7	Buildings	5294	(hwy <>1) or height (<8.5m) or Area (<179m^2)	Image Observation
Hwy = 1: objects that intercept the highway found in DT1;MM structures : Man-made structures				

Descriptive Statistics DT2

Two datasets are employed in DT2 to separate vegetation from man-made structures, Node 3 (Figure 3-9); their descriptive statistics are presented in Table 4-8. The training dataset encompasses 100 point samples for building presence (1) and 81 points for building absence (0). The test-dataset includes 303 samples for presences and 164 for absences. The tendencies of the means in DT2 are similar to those in DT1 for the reasons discussed previously.

Table 4-8 Group statistics for training and test-dataset for DT2

	Training Dataset for DT2					Test Dataset for DT2			
	Presence/ Absence	N	Mean	Std. Deviation		Presence/ Absence	N	Mean	Std. Deviation
NDVI	1	100	0.05	0.10	NDVI	1	303	0.06	0.10
	0	81	0.36	0.21		0	164	0.37	0.21
Sobel	1	100	1.58	0.94	Sobel	1	303	1.66	0.83
	0	81	3.33	1.18		0	164	3.21	1.11
Area	1	100	444.68	1269.88	Area	1	303	361.92	1184.40
	0	81	135.99	173.28		0	164	96.29	131.29
PA	1	100	0.55	0.29	PA	1	303	0.57	0.24
	0	81	1.10	0.36		0	164	1.20	0.42

Table 4-9 displays the results of an independent samples t-test; NDVI, Area and PA met the criterion of equal variance. In addition, PA and NDVI present significantly different means (between presences and absences) that indicate they are suitable criteria for separating buildings from vegetation. In contrast, the mean Area is not significantly different between presences and absences. The Sobel criterion does not meet the test assumption of equal variance, and so the result for the mean is not trustworthy.

Table 4-9 T-test for independent samples training-dataset DT2

	EVA	Levene's Test for Equality of Variances		t-test for Equality of Means					Confidence Interval of the Difference	
		F	Sig.	t	df	Sig. (2 - tailed)	Mean Difference	Std. Error Difference	95% Lower	95% Upper
NDVI	yes	68.139	0.000	-13.11	179.00	0	-0.317	0.0242	-0.36559	-0.26994
	no			-12.28	110.19	0	-0.317	0.0258	-0.36905	-0.26649
Sobel	yes	1.994	0.160	-11.09	179.00	0	-1.753	0.1580	-2.06532	-1.44158
	no			-10.83	151.07	0	-1.753	0.1618	-2.07318	-1.43372
Area	yes	9.148	0.003	2.17	179.00	0.031	308.68	142.2308	28.0193	589.348
	no			2.40	103.53	0.018	308.68	128.4393	53.9707	563.397
PA	yes	8.538	0.004	-11.34	179.00	0	-0.548	0.0483	-0.64345	-0.45270
	no			-11.06	150.16	0	-0.548	0.0495	-0.64595	-0.45020

Variance significance< 0.05 indicates the groups' variance is not significantly different and the assumption of the test is met. Mean significance <0.05 indicates the group mean is significantly different and the criterion is suitable to distinguish between presence and absence group. EVA=Equal variances assumed

Receiver Operator Characteristic (ROC) Curves DT2

The receiver operator characteristic (ROC) curves are built from the training-dataset (Figure 4-2). They suggest that, at this level of segmentation, the best predictors are PA and NDVI because they top the other curves for sensitivities over 90%. The Area appears to be the least useful criterion because its curve barely reaches the reference diagonal that represents a random classification.

The larger area under the curve belongs to PA (0.93%), followed by the Sobel (0.91%), NDVI (0.89%), and Area (0.67%). The area under the curve (AUC) is an indicator of the overall reliability of a predictor model; however, AUC may be misleading if the the goal is maximizing the number of precences, even at the expense of increasing the number of false possitives. For example, the Sobel curve (Figure 4-2) is very efficient, detecting up to 84% of positives (yielding 12% of false positives); however, it loses efficiency, detecting over 90% of true

positive (returning 49% of false positives). Different to PA and NDVI, which present values apropriated to select over 90% of presences, while they keep a low number of false positives (20 and 22% respectively).

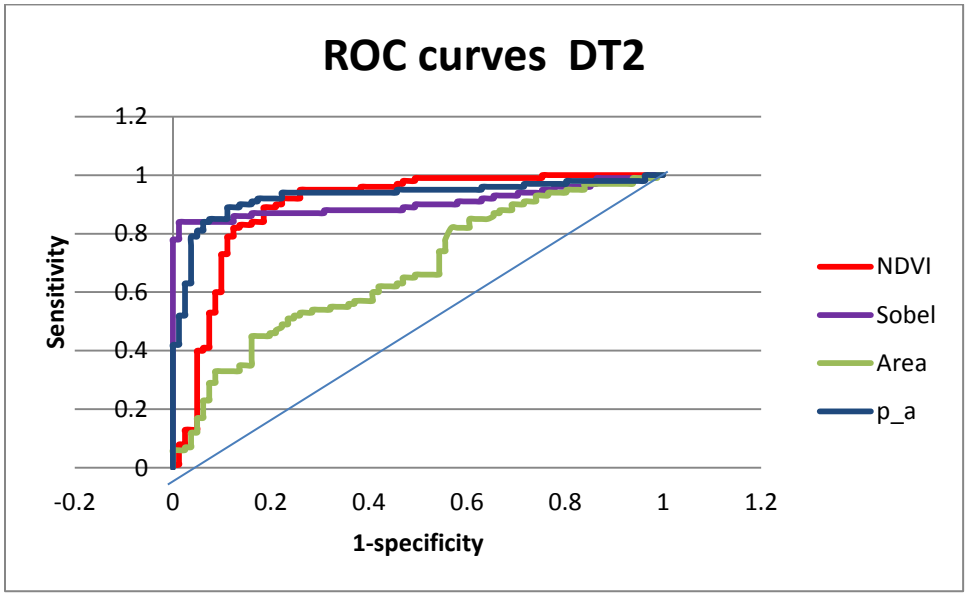

Figure 4-2 ROC curves for NDVI, PA, Sobel and Area for DT2

Selection of Criteria and Thresholds for DT2

The cut values selected for every criterion are shown in Table 4-10. In individual treatments, NDVI (T11) and PA (T12) have the best results, with 95% and 94% of presences detected versus 26% and 22% false positives respectively. In the combined treatments, the best combinations are T15 (NDVI or PA) and T16 (NDVI or Sobel), both detect 100% of the buildings, while they yield 44% and 58% of false positive, respectively. T15 was selected because it obtains the best results and combined the two predictors with better individual performances (NDVI and PA).

Table 4-10 Selected cut points for for treatments T11 to T20, training dataset

Treatment	Criteria	Cut Value	Sensitivity (true positives)	1-Specificity (false positive)
T11	NDVI	(<0.202)	0.95	0.26
T12	PA	(<0.81)	0.94	0.22
T13	Sobel	(<3.11)	0.90	0.49
T14	Area	(>84)	0.72	0.54
T15	NDVI or PA	(*)	1.00	0.44
T16	NDVI or Sobel	(*)	1.00	0.58
T17	NDVI or Area	(*)	0.98	0.65
T18	PA or Sobel	(*)	0.97	0.59
T19	PAor Area	(*)	0.94	0.57
T20	Sobel or Area	(*)	0.95	0.73
(*) The combined treatments keep the individual cut values presented in individual treatments.				

Cross Validation DT2

The independent samples t-test are applied to the test-dataset in DT2. The results are presented in Table 4-11. As in the training-dataset, PA and NDVI meet the assumption of the test about having equal variance, and their means are significantly different. The Sobel does not meet the test assumption of equal variance. Different to the training-dataset, the Area criterion meets the assumption of the test and its means are significantly different between presences and absences.

Table 4-11 T-test for independent samples test -dataset DT2

		Levene's Test for Equality of Variances		t-test for Equality of Means					Confidence Interval of the Difference	
	EVA	F	Sig.	t	df	Sig. (2 - tailed)	Mean Diff.	Std. Error Diff.	95% Lower	95% Upper
NDVI	yes	178.04	0	-21.504	465	0	-0.31621	0.01470	-0.34510	-0.28731
	no			-17.821	204.92	0	-0.31621	0.01774	-0.35119	-0.28122
Sobel	yes	3.58	0.059	-17.062	465	0	-1.55390	0.09107	-1.73287	-1.37493
	no			-15.663	262.86	0	-1.55390	0.09920	-1.7492	-1.35855
Area	yes	9.93	0.002	2.861	465	0.004	265.620	92.8379	83.1871	448.054
	no			3.86	315.57	0	265.620	68.8099	130.236	401.005
PA	yes	74.62	0	-20.588	465	0	-0.62915	0.03055	-0.68920	-0.56910
	no			-17.804	225.88	0	-0.62915	0.03533	-0.69878	-0.55951

Variance Sing < 0.05 indicates the groups variance is not significantly different and the assumption of the test is met. Mean sig. <0.05 indicates the group mean is significantly different and the criterion is suitable to distinguish between presence and absence groups.
EVA=Equal variances assumed

Table 4-12 exhibits the cross-validation of the selected cut values applied to the test-dataset. The individual criteria that obtain the best result are the Sobel, at 93%, followed by NDVI, at 90%, and PA, at 88%. The Area has the lower results, 76%. However, the Sobel returns the highest number of false positive (56%), different to NDVI and PA that return 26% and 20%, respectively. In the combined treatments, the best result is for T16 (NDVI or Sobel), followed by T15 (NDVI or PA). However, because the Sobel criteria does not meet the assumption of equal variance in the t-test, and because it gives a high number of false positives, T15 (NDVI or PA) appears as the most suitable criterion.

Table 4-12 Cross validation of the cut values for treatment T11 to T20, test-dataset of DT2

Treatment	Criteria	Cut Value	Sensitivity (true positives)	1-Specificity (false positive)
T11	NDVI	(<0.202)	0.90	0.26
T12	PA	(<0.81)	0.88	0.20
T13	Sobel	(<3.11)	0.93	0.56
T14	Area	(>84)	0.76	0.39
T15	NDVI or PA	(*)	0.99	0.43
T16	NDVI or Sobel	(*)	1.00	0.65
T17	NDVI or Area	(*)	0.99	0.55
T18	PA or Sobel	(*)	0.97	0.64
T19	PAor Area	(*)	0.89	0.41
T20	Sobel or Area	(*)	0.97	0.71
(*) The combined treatments keep the individual cut values presented in individual treatments.				

4.1.3 Results of Decision Tree Three (DT3)

The Third decision tree (DT3) starts identically to DT1 and DT2, and returns identical results from Node I to VII (Figure 3-10). Then, the Sobel segmentation creates 80288 objects, and after the objects smaller than 20m^2 are merged into the larger neighbours; 5845 objects remain. The classification results obtained by DT3, from Node 1 to 7, are disclosed in Table 4-13.

Table 4-13 Classification result of DT3

Node	Object Class	Number of Objects	Criteria of selection	Method of threshold selection
1	Objects 2	5845		
2	Ground 2	19	Height<2m	Image Observation
3	Non-Ground 2	5826	Height>2m	Image Observation
4	Class I	2807	Area <88m^2	Image Observation
5	Class II	1522	88m^2<Area <259m^2	Image Observation
6	Class III	1497	Area >259m^2	Image Observation
7	Vegetation	155	NDVI>0.38 AND PA<1.24	Statistical Analysis
8	M.M. Structures	2652	NDVI<0.38 OR PA<1.24	Statistical Analysis
9	Vegetation	46	NDVI>0.171 AND PA>817	Statistical Analysis
10	M.M. Structures	1476	NDVI<0.171 OR PA<0.817	Statistical Analysis
11	Vegetation	4	NDVI>0.5 AND Sobel>2.63	Image Observation
12	M.M. Structures	1497	NDVI<0.5 OR Sobel<2.63	Image Observation
13	Highway	21	(Hwy=1) AND Sobel >0.97 AND Height >3.12	Image Observation
14	Buildings	2600	(Hwy<>1) OR Sobel <0.97 OR Height < 3.12	Image Observation
15	Highway	5	(Hwy=1) AND PA>0.46	Image Observation
16	Buildings	1471	(Hwy<>1) OR PA<0.46	Image Observation
17	Highway	8	(Hwy=1) AND PA >0.176 AND Height >7.78	Image Observation
18	Buildings	1485	(Hwy<>1) OR PA <0.176 OR Height <7.78	Image Observation
(hwy=1) :objects that intercept the highway found in DT1; (hwy<>1) objects that do not intercept the highway found in DT1.				

Descriptive Statistics of DT3

Group-statistics were built for the training- and test-datasets; they are displayed in Table 4-14. The training-dataset encompasses, in Class I, 34 observations for building presences (1) and 37 observations for their absences (0). In Class II, it comprises 33 observations for presences and 37 for absences. Finally, in Class III, it includes 33 observations for presences and only 7 observations for absences. The seven absences are considered insufficient to draw a general rule.

Table 4-14 Group statistics for training and test dataset for DT3

		Training Dataset for DT3				Test Dataset for DT3				
		Presence/ Absence	N	Mean	Std. Dev		Presence/ Absence	N	Mean	Std. Dev
Class I	NDVI	1	34	0.05	0.13	NDVI	1	79	0.04	0.09
		0	37	0.39	0.23		0	101	0.39	0.23
	Sobel	1	34	1.98	1.04	Sobel	1	79	1.79	0.99
		0	37	3.57	1.66		0	101	3.33	1.35
	Area	1	34	66.69	19.44	Area	1	79	62.16	17.82
		0	37	49.66	19.51		0	101	41.51	17.91
	PA	1	34	0.80	0.33	PA	1	79	0.84	0.26
		0	37	1.33	0.36		0	101	1.39	0.38
Class II	NDVI	1	33	0.03	0.09	NDVI	1	129	0.05	0.11
		0	37	0.32	0.21		0	56	0.34	0.20
	Sobel	1	33	1.50	1.00	Sobel	1	129	1.71	0.86
		0	37	3.10	0.47		0	56	3.00	0.54
	Area	1	33	155.56	49.58	Area	1	129	155.7	50.80
		0	37	140.90	52.11		0	56	136.3	46.76
	PA	1	33	0.53	0.09	PA	1	129	0.56	0.12
		0	37	0.94	0.22		0	56	0.91	0.24
	NDVI	1	33	0.05	0.08	NDVI	1	95	0.08	0.11
		0	7	0.48	0.12		0	7	0.48	0.12
Class III	Sobel	1	33	1.25	0.58	Sobel	1	95	1.47	0.59
		0	7	3.26	0.39		0	7	3.26	0.39
	Area	1	33	1123.24	2067.1	Area	1	95	891.1	2021.4
		0	7	566.39	345.77		0	7	566.3	345.77
	PA	1	33	0.32	0.11	PA	1	95	0.37	0.11
		0	7	0.72	0.16		0	7	0.72	0.16

Table 4-15 describes the outcomes of the independent samples t-test carried out with the training-and test-datasets. Only NDVI met the assumption of equal variance between presences and absences in the three classes. Sobel and PA met the assumption of equal variance in Class II (objects between 88 and 259m^2). The Area criterion did not meet the assumption of the test in any of the classes. NDVI, PA and Sobel present significantly mean differences in the three

classes. In contrast, the Area criterion does not show a significant mean difference between presences and absences in any of the classes.

Table 4-15 Independent samples t-test for training-dataset DT3

		EVA	Levene's Test for Equality of Variances		t-test for Equality of Means					Confidence Interval of the Difference	
			F	Sig.	t	df	Sig. (2 - tailed)	Mean Diff.	Std. Error Diff.	95% Lower	95% Upper
Class I	NDVI	yes	15.09	0.00	-7.54	69.00	0.00	-0.33	0.04	-0.42	-0.25
		no			-7.70	58.62	0.00	-0.33	0.04	-0.42	-0.25
	Sobel	yes	0.05	0.83	-4.81	69.00	0.00	-1.60	0.33	-2.26	-0.93
		no			-4.90	61.27	0.00	-1.60	0.33	-2.25	-0.95
	Area	yes	0.27	0.60	3.68	69.00	0.00	17.03	4.63	7.80	26.26
		no			3.68	68.53	0.00	17.03	4.63	7.80	26.26
	PA	yes	1.29	0.26	-6.44	69.00	0.00	-0.53	0.08	-0.70	-0.37
		no			-6.47	68.98	0.00	-0.53	0.08	-0.70	-0.37
Class II	NDVI	yes	29.48	0.00	-7.30	68.00	0.00	-0.29	0.04	-0.36	-0.21
		no			-7.58	51.58	0.00	-0.29	0.04	-0.36	-0.21
	Sobel	yes	9.27	0.00	-8.76	68.00	0.00	-1.61	0.18	-1.97	-1.24
		no			-8.43	44.16	0.00	-1.61	0.19	-1.99	-1.22
	Area	yes	0.11	0.74	1.20	68.00	0.23	14.66	12.20	-9.67	39.00
		no			1.21	67.70	0.23	14.66	12.16	-9.61	38.93
	PA	yes	14.20	0.00	-10.00	68.00	0.00	-0.41	0.04	-0.49	-0.33
		no			-10.41	49.83	0.00	-0.41	0.04	-0.49	-0.33

Variance Significance < 0.05 indicates the groups variance is not significantly different and the assumption of the test is met. Mean sig. <0.05 indicates the group mean is significantly different and the criterion is suitable to distinguish between presence and absence group. EVA=Equal variances assumed

The results suggest that the NDVI criterion is appropriate to distinguish between vegetation and man-made structures at all object sizes, while the PA and Sobel would be suitable predictors for objects between 88 m^2 and 259m^2, but not for objects smaller than 88m^2 (Table 4-15). The Area does not seem an appropriated classification criterion in any classes. That is because in Class I

the Area do not met the assumption of equal variance (EVA) of the test, and in Class II the Area is not significantly different between the groups (presences and absences)

Receiver Operator Characteristic (ROC) Curves for DT3

The receiver operator characteristic (ROC) curves for objects smaller than 88m^2 (Class I from DT3) are illustrated in Figure 4-3. For sensitivities greater than 85%, the NDVI curve tops the other criteria, followed by PA, Sobel and finally Area. The larger area under the curve (AUC) is PA (89.7%), followed by NDVI (87.5%), Sobel (82.9%), and Area (75%).

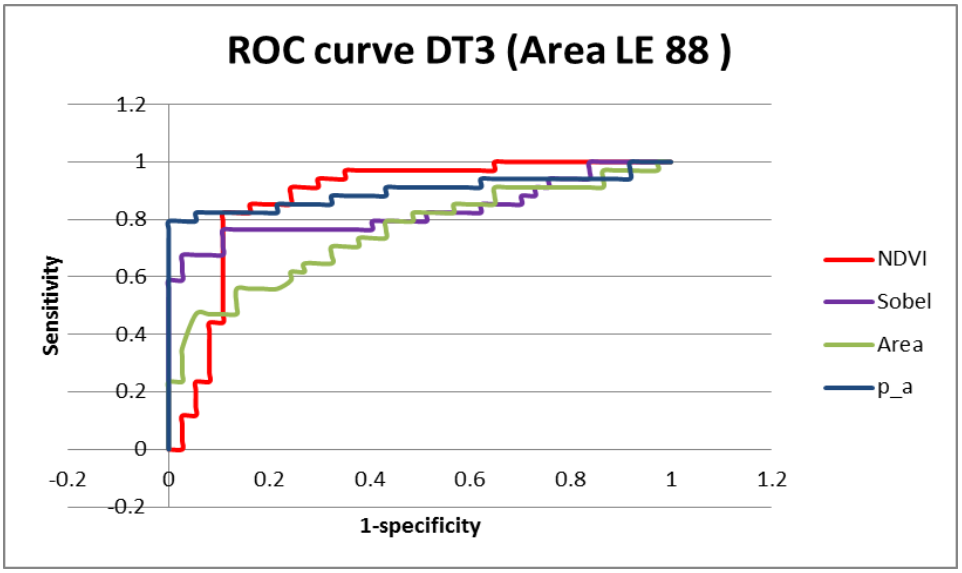

Figure 4-3 ROC curves for NDVI, PA, Sobel and Area for class I of DT3

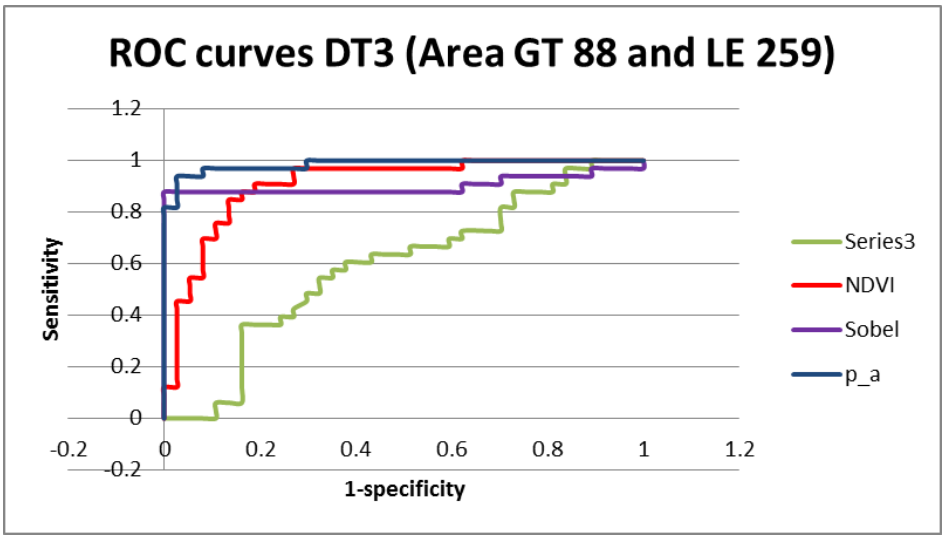

Figure 4-4 ROC curves for NDVI, PA, Sobel and Area for Class II of DT3

Figure 4-4 shows the ROC curves for the objects between 88 and 259m^2(Class II of DT3). For sensitivities higher than 85%, the PA curve tops the other criteria, followed by NDVI, Sobel and Area. The larger area under the curve (AUR) is from PA (98.5%) followed by NDVI (90.9%), Sobel (90.2%), and Area (59.3%).

Selection of Criteria and Thresholds for DT3

The selected threshold values for DT3 are described in Table 4-16 Selected Threshold Values for the Training Dataset; in addition, this table displays the sensitivities and one minus specificity for these thresholds.

Table 4-16 Selected Threshold Values for the Training Dataset DT3

	Treatment	Criteria	Cut Value	Sensitivity (true positives)	1-Specificity (false positive)
Class I	T21	NDVI	(<0.38)	0.97	0.35
	T22	PA	(<1.24)	0.91	0.43
	T23	Sobel	(<3.06)	0.76	0.41
	T24	Area	(>51)	0.82	0.49
	T25	NDVI or PA	(*)	1.00	0.62
	T26	NDVI or Sobel	(*)	1.00	0.54
	T27	NDVI or Area	(*)	1.00	0.73
	T28	PA or Sobel	(*)	0.94	0.62
	T29	PAor Area	(*)	0.91	0.68
	T30	Sobel or Area	(*)	0.88	0.73
	Treatment	**Criteria**	**Cut Value**	**Sensitivity (true positives)**	**1-Specificity (false positive)**
Class II	T21	NDVI	(<0.171)	0.97	0.27
	T22	PA	(<0.817)	1.00	0.30
	T23	Sobel	(<2.359)	0.88	0.00
	T24	Area	(>132.5)	0.61	0.38
	T25	NDVI or PA	(*)	1.00	0.49
	T26	NDVI or Sobel	(*)	1.00	0.27
	T27	NDVI or Area	(*)	1.00	0.49
	T28	PA or Sobel	(*)	1.00	0.30
	T29	PAor Area	(*)	1.00	0.54
	T30	Sobel or Area	(*)	0.91	0.38
(*) The combined treatments keep the individual cut values presented in individual treatments.					

In Class I, objects smaller than 88m^2, the individual criteria that perform the best are NDVI and PA, with 97% and 91% of building detected, and with 35% and 43% false positives, respectively.

In Class II, objects between 88 and 259m^2, PA is the variable that operates the best, followed by NDVI with 100% and 97% of building detected and 30% and 27% false positive, respectively.

Cross Validation of DT3

The results of the independent sample t-testing, carried out on the test-dataset of DT3, are disclosed in Table 4-17, in Class I, the NDVI and PA criteria meet the assumption of equal variance between the groups (presences and absences), and both present significant differences in their means. In Class I (objects between 88 and 259m^2) the Sobel and PA criteria meet the assumption of equal variance and all of them present significant differences in their means.

Table 4-17 T-test for independent sample for the test-dataset DT3

		EVA	Levene's Test for Equality of Variances		t-test for Equality of Means					Confidence Interval of the Difference	
			F	Sig.	t	df	Sig. (2 tailed)	Mean Difference	Std. Error Difference	95% Lower	95% Upper
Class I	NDVI	yes	91.99	0.00	-13.01	178.00	0.00	-0.35	0.03	-0.40	-0.30
		no			-14.21	138.71	0.00	-0.35	0.02	-0.40	-0.30
	Sobel	yes	1.17	0.28	-8.48	178.00	0.00	-1.53	0.18	-1.89	-1.18
		no			-8.79	177.36	0.00	-1.53	0.17	-1.88	-1.19
	Area	yes	0.03	0.87	7.70	178.00	0.00	20.66	2.68	15.36	25.95
		no			7.70	168.10	0.00	20.66	2.68	15.36	25.95
	PA	yes	9.53	0.00	-10.92	178.00	0.00	-0.55	0.05	-0.65	-0.45
		no			-11.41	175.47	0.00	-0.55	0.05	-0.65	-0.46
Class II	NDVI	yes	46.81	0.00	-12.72	183.00	0.00	-0.28	0.02	-0.33	-0.24
		no			-10.15	68.96	0.00	-0.28	0.03	-0.34	-0.23
	Sobel	yes	19.18	0.00	-10.36	183.00	0.00	-1.29	0.12	-1.53	-1.04
		no			-12.33	159.60	0.00	-1.29	0.10	-1.49	-1.08
	Area	yes	4.19	0.04	2.44	183.00	0.02	19.40	7.94	3.73	35.07
		no			2.52	113.05	0.01	19.40	7.68	4.17	34.62
	PA	yes	38.21	0.00	-13.45	183.00	0.00	-0.36	0.03	-0.41	-0.30
		no			-10.52	66.97	0.00	-0.36	0.03	-0.42	-0.29

Variance Significance < 0.05 indicates the groups variance is not significantly different and the assumption of the test is met. Mean significance <0.05 indicates the group mean is significantly different and the criterion is suitable to distinguish between presence and absence group.

In order to validate the threshold selected for the training-dataset, the criteria and thresholds are assessed for the test-dataset; the results are presented in Table 4-18. In Class I, NDVI obtains the best individual results, followed by PA and Sobel. The combination selected was T25 (NDVI or PA) because Sobel does not meet the condition of the independent samples t-test.

In Class II, as well as in the training dataset, PA obtained the best individual result; however, the second place was shared between NDVI and Sobel. The best combined criterion was T25 (NDVI or PA) it obtained the best combined results, with 100% of building detected and 55% false positives; in addition, both individual predictors met the condition of the t-test.

Table 4-18 Cross validation of the cut values DT3

	Treatment	Criteria	Cut Value	Sensitivity (true positives)	1-Specificity (false positive)
Class I	T21	NDVI	(<0.38)	0.99	0.44
	T22	PA	(<1.24)	0.95	0.33
	T23	Sobel	(<3.06)	0.95	0.33
	T24	Area	(>51)	0.72	0.28
	T25	NDVI or PA	(*)	1.00	0.64
	T26	NDVI or Sobel	(*)	1.00	0.71
	T27	NDVI or Area	(*)	1.00	0.66
	T28	PA or Sobel	(*)	1.00	0.60
	T29	PAor Area	(*)	0.95	0.48
	T30	Sobel or Area	(*)	0.94	0.61
	Treatment	**Criteria**	**Cut Value**	**Sensitivity (true positives)**	**1-Specificity (false positive)**
Class II	T21	NDVI	(<0.171)	0.78	0.11
	T22	PA	(<0.817)	0.97	0.39
	T23	Sobel	(<2.359)	0.78	0.11
	T24	Area	(>132.5)	0.57	0.36
	T25	NDVI or PA	(*)	1.00	0.55
	T26	NDVI or Sobel	(*)	0.98	0.30
	T27	NDVI or Area	(*)	0.96	0.46
	T28	PA or Sobel	(*)	0.98	0.41
	T29	PA or Area	(*)	0.97	0.57
	T30	Sobel or Area	(*)	0.90	0.39

(*) The combined treatments keep the individual cut values presented in individual treatments.

4.1.4 Comparing Treatments

In order to easily compare decision trees methods, this section summarise, the results of independent sample t-test, AUC, and accuracy assessment. In addition, relevant screenshots of a visual inspection are presented.

Summary Tables

Table 4-19 summarises the results obtained for every variable in the t- tests

Table 4-19 Summary of Independent Sample t-tests

	DT1		DT2		DT3				Total
					Class I		Class II		
	Training	Test	Training	Test	Training	Test	Training	Test	
NDVI	1	1	1	1	1	1	1	1	**9**
PA	1	1	1	1	0	1	1	1	**7**
Sobel	1	1	0	0	0	0	1	1	**4**
Area	0	0	0	1	0	0	0	1	**2**

The selected treatment for each decision tree is display in Table 4-20. This table includes the criteria, cut values and accuracy assessment results of each treatment.

Table 4-20: Summary of cut value of each criteria, sensitivity and specificity

		Treatment	Threshold		Accuracy Assessment	
			NDVI	PA	Sens.	1-Sp
DT1		T5 (NDVI OR PA)	0.25	0.675	100%	44%
DT2		T15 (NDVI OR PA)	0.202	0.81	99%	43%
Total DT3					**100%**	**59%**
	DT3 class I	T25 (NDVI OR PA)	0.38	1.24	100%	64%
	DT3 class II	T25 (NDVI OR PA)	0.172	0.81	100%	55%

Sens.: Sensitivity(true positives)
1-Sp: 1-Specificity(false positive)

The area under the curve of the predictors for each decision tree is summarised in Table 4-21.

Table 4-21: Area under the curve AUC

	DT1	DT2	DT3 I	DT3 II
NDVI	0.91	0.89	0.88	0.91
PA	0.93	0.91	0.83	0.90
Area	0.85	0.67	0.75	0.59
Sobel	0.75	0.93	0.90	0.99

Visual Inspection

Visual inspection is an important criterion used to assess the quality of results. This section presents screen shots of relevant issues found during this study. The utility of the object-oriented approach for integrating LiDAR data and satellite imagery; a comparison of the performance of the tree decision trees, and finally the resulting map of the best treatment (T25).

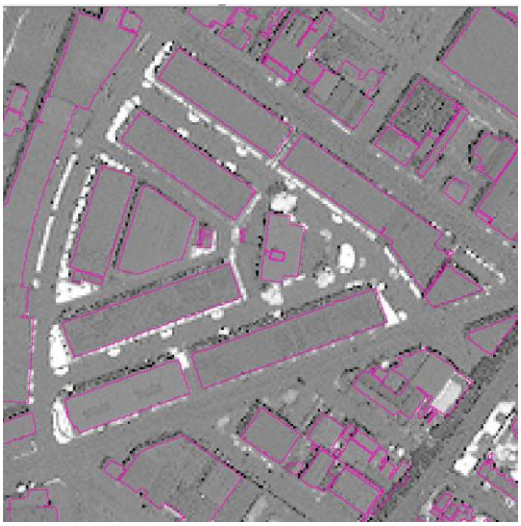

(a)

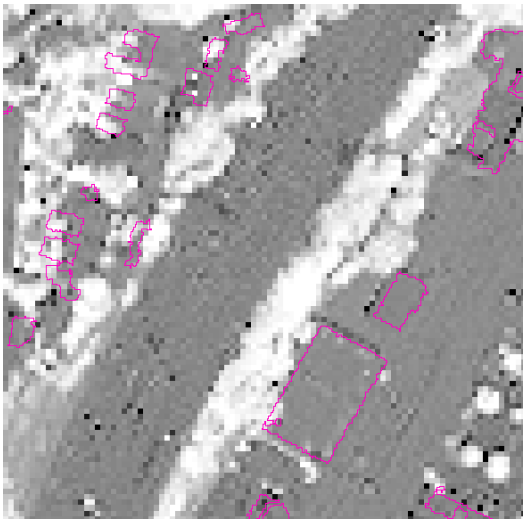

(b)

Figure 4-5 Building outlines (in pink) derived from LiDAR data and NDVI derived from satelite imagery (a) LiDAR and satelite data matching perfectly (b) LiDAR and satelite data Mismatching

The object oriented approach is a very appropriate way to integrate LiDAR and satellite imagery data.

Figure 4-5 (a) illustrates a perfect match between building outlines (in pink), derived from LiDAR data, and the NDVI, derived from satellital imagery. The white color indicates high NDVI values, for which pixels correspond to vegetation. The dark colors indicate low NDVI values are caracterict on the ground and buildings. A perfect macth between data allows a pixel by pixel classification based on height and NDVI values.

In contrast, Figure 4-5 (b) shows an offset between the the LiDAR and satellital imagery, in these cases a pixel-by-pixel classification would be not useful. However, an object classification allows one to distiguish between objects based on the average of the pixels inside the obejct and the geometry of the object.

(a)

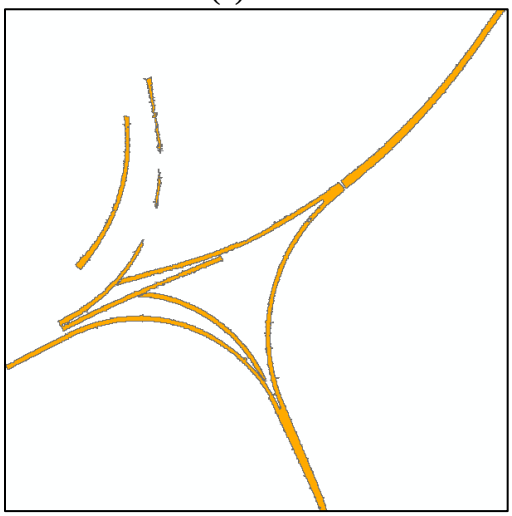

(b)

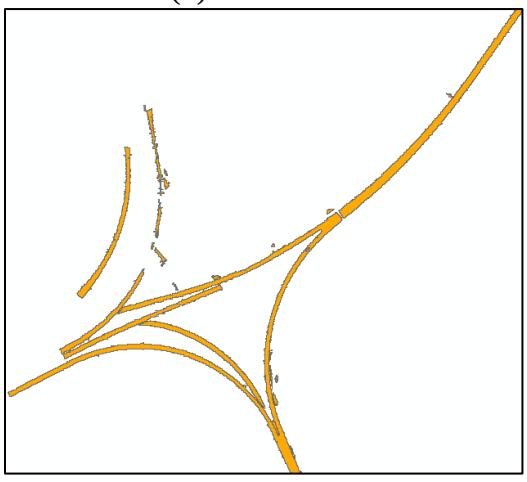

(c)

Figure 4-6 Roads detection (a) DT1, (b) DT2, and (c) DT3

The roads were detected to separate them from the buildings, in order to carry out the solar analysis only in places suitable to set solar panels..

Figure 4-6 shows the selection of the highway of DT1, DT2 and DT3, in (a), (b), and (c), respectively.

Figure 4-6 (a) depicts DT1 detection of the roads. The low level of segmentation of DT1 does not allow separating the highway from adjacent buildings.

Figure 4-6 (b) shows the road selection of DT2, which does not include neighboring structures.

Figure 4-6 (c) illustrates the selection of road with DT3, which does not include adjacent buildings, but does contain small features that are not present in DT2 (b)

(a)

(b)

(c)

Figure 4-7 Building detection (a) DT1, (b) DT2, and (c) DT3

Building detection using DT1, DT2 and DT3 is illustrated in Figure 4-7(a), (b), and (c), respectively.

The low level of segmentation of DT1 does not allow it to clearly define complex shapes. Figure 4-7(a) shows four buildings that were roughly approximate to a square shape by DT1.

The same four buildings, detected by DT2, in Figure 4-7 (b), are better defined in their forms.

Figure 4-7(c) illustrates the building selection of DT3. The object shapes are well defined, but DT3 (c) includes smaller objects than DT2 (b).

(a)

(b)

(c)

Figure 4-8 shows the differences between DT1, DT2 and DT3 in separating adjacent and overhanging features.

For example, Figure 4-8 (a) shows a tree overlapping a building; these two features are detected as a single object by DT1.

In contrast, Figure 4-8 (b) illustrates that DT2 is able to distinguish between the tree and building, and in (b), only the buildings are represented. Moreover, DT2 is better able to separate and define adjacent constructions.

Finally, Figure 4-8(c) presents the building detection of DT3, as well as DT2, DT3 (b) is able to separate the overlapping tree from the building. In addition, DT3 (c) detects smaller buildings that DT2 (b) omit.

Figure 4-8 Overlaping features (a) DT1, (b) DT2, and (c) DT3

DT 3 was identified as the best decision tree to carry out the building detection, because DT3 obtained better results than DT2 in the accuracy assessment (Table 4-20). Moreover, visual inspection shows that DT3 is better than DT1 at defining shapes (Figure 4-7), and separating adjacent and overlapping objects (Figure 4-8). In addition, T25 was acknowledged as the best treatment to carry out building detection because it combines the use of DT3 with the stronger predictors, NDVI and PA. Figure 4-9 present the building outlines extracted by T25.

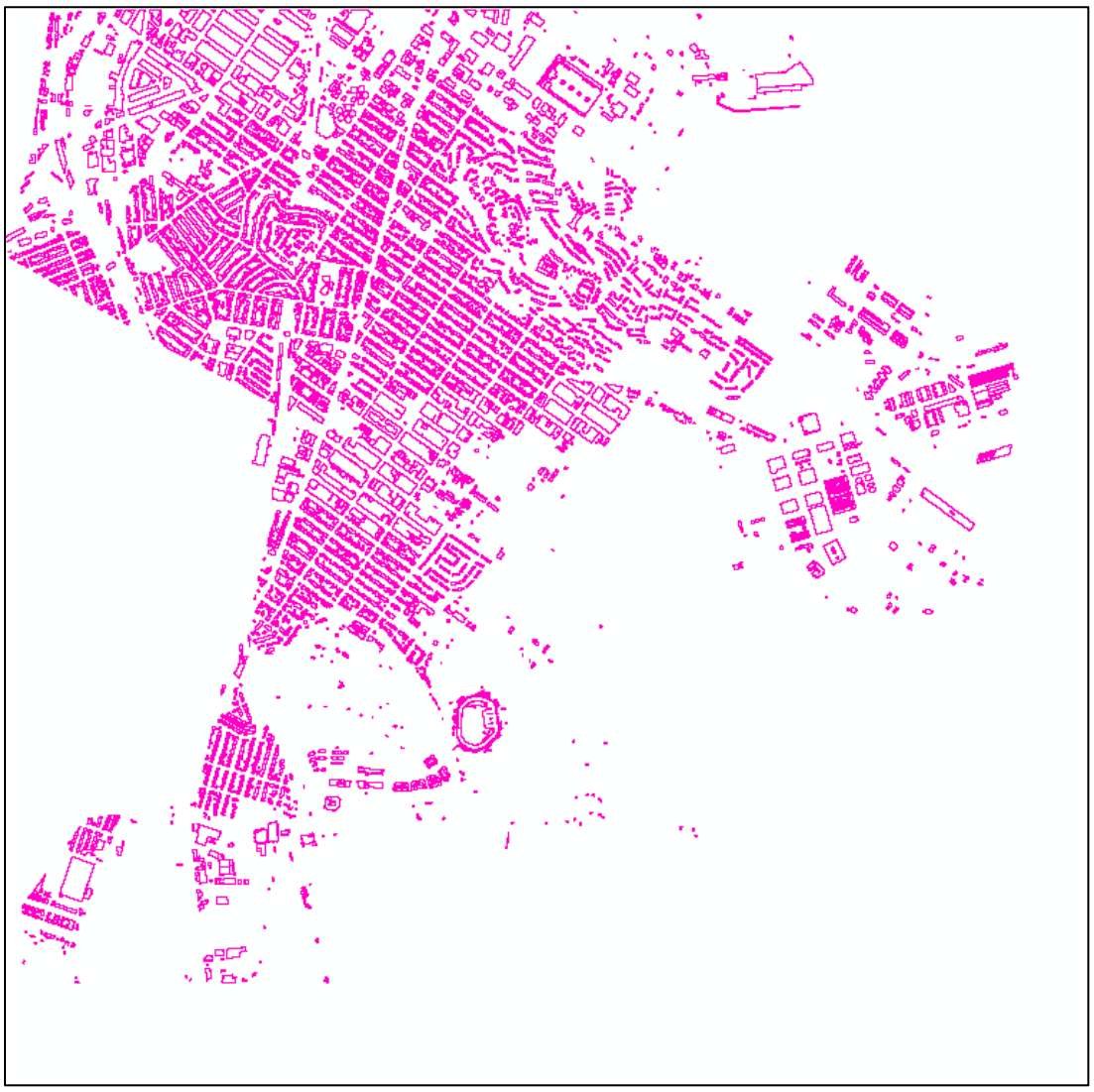

Figure 4-9 Building detection by DT3

4.2 Results of Solar Radiation Modelling

This section encompasses three parts. The first involves estimating the number of calibration samples. The second describes the model calibration, which implies the selection of a treatment. The third part presents the model assessment.

4.2.1 Number of Calibration Samples

The solar radiation of locations with tilt zero are mapped in Figure 4-10. These solar radiation values are plotted in a histogram, in Figure 4-11, where the y-axes represents the number of pixels that present a solar radiation amount, and the x-axes represents the amount of solar radiation present in the image. In the histogram (Figure 4-11), the threshold that separates the upper two third parts of the peak is highlighted in blue; solar radiation amounts greater than this threshold are considered shade-free.

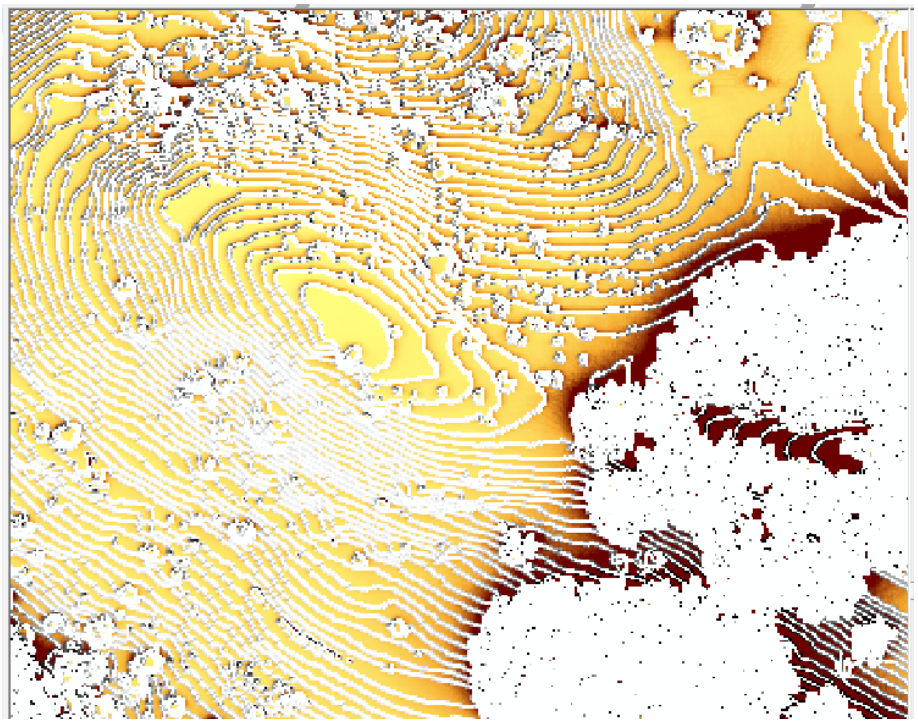

Figure 4-10: Solar map of places with tilt of zero

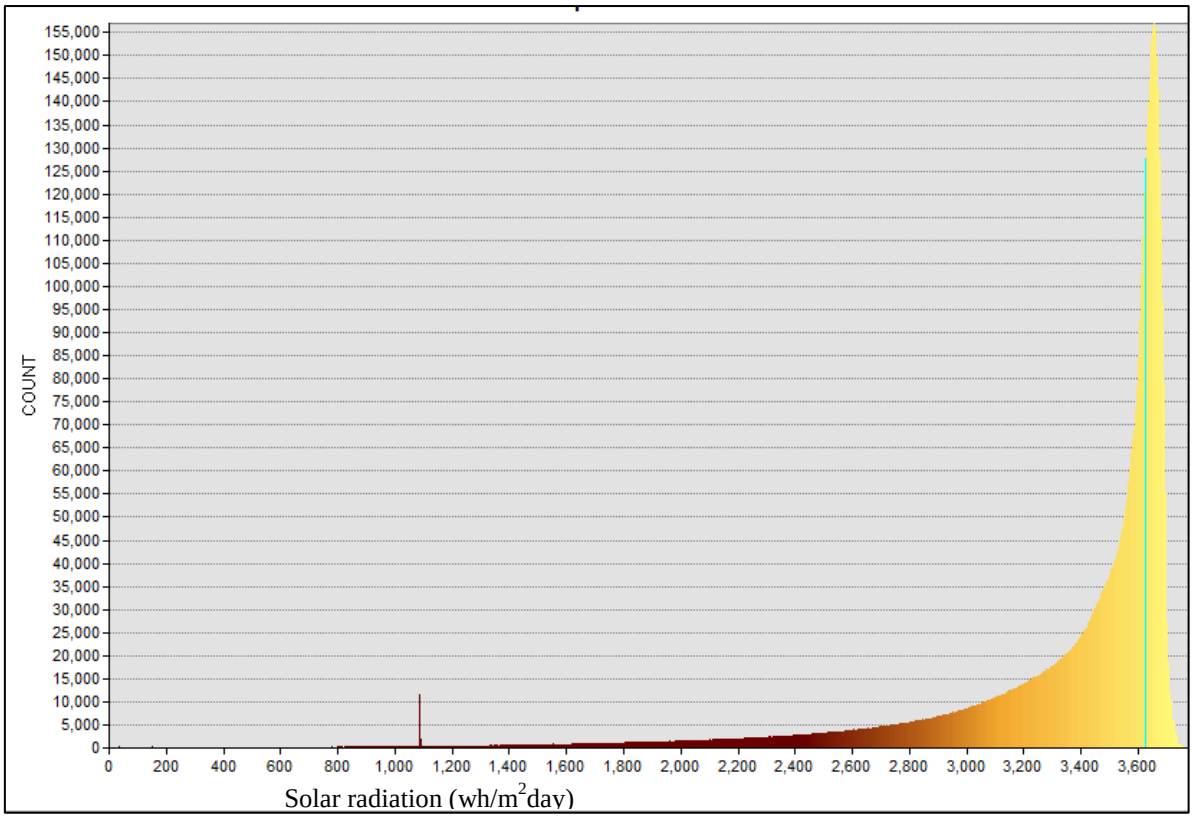

Figure 4-11: Image histogram of places with tilt of zero

The image statistics of the places- shade-free, facing south and having tilts of 0, 19, 26, 35, 38, 51, 54, or 89 - were used to calculate the number of calibration samples, according (in Chapter 3)

According to Table 4-22, the minimum number of samples needed to obtain a 99% confidence level is six; this study takes 9 samples, composed of 150 pixels each, in order to ensure a good representation of the data. The samples were selected from shade-free places with a tilt of 0.

Table 4-22 Image statistics for solar energy map (wh/m^{2}day) on places with similar conditions to solar collectors using default atmospheric parameters.

	Tilts						
	0	**19**	**26**	**35**	**38**	**51**	**54**
min	3616	3760	3897	3603	3744	3486	3135
max	3782	3916	4043	3761	3898	3606	3289
mean	3656	3800	3937	3651	3788	3521	3198
Std. Dev.	23.8	26.0	22.9	30.1	26.1	22.4	31.2
error 1%	36.56	38	39.37	36.51	37.88	35.21	31.98
Number of samples	3	3	2	4	3	3	6
(*) 99% of confidence							

4.2.2 Model Calibration

The atmospheric parameters of the Solar Analyst tool of ESRI are: Diffuse proportion and Transmittivity. All their possible combinations were run for the nine calibration sites, generating 90 treatments, which were assessed by comparing them with the weather station data. The monthly results are shown in APPENDIX A; the yearly results are presented in Table 4-23, T45 (in bold) seems to be closer to the weather station measurements (4.7kwh/m^{2}day).

Table 4-23 Yearly result of solar parameter combination.

Diffuse Proportion	**Atmospheric Trasmittivity**									
	0.1	**0.2**	**0.3**	**0.4**	**0.5**	**0.6**	**0.7**	**0.8**	**0.9**	**1.0**
0.1	0.32	0.80	1.40	2.12	2.96	3.92	5.04	6.31	7.78	9.50
0.2	0.35	0.87	1.53	2.32	3.25	4.32	5.56	7.00	8.67	10.64
0.3	0.38	0.96	1.69	2.57	3.62	4.83	6.24	7.88	9.81	12.11
0.4	0.43	1.08	1.91	2.92	4.11	5.51	7.14	9.06	11.33	14.08
0.5	0.49	1.25	2.22	3.40	**4.80**	6.46	8.41	10.71	13.46	16.82
0.6	0.59	1.50	2.68	4.11	5.84	7.88	10.30	13.18	16.66	20.94
0.7	0.75	1.92	3.44	5.31	7.57	10.26	13.47	17.31	21.98	27.81
0.8	1.07	2.76	4.97	7.71	11.03	15.01	19.79	25.55	32.63	41.54
0.9	2.04	5.28	9.56	14.90	21.41	29.27	38.75	50.29	64.57	82.72
1.0	Non valid results									

The square differences of every treatment with the weather station data is presented in Table 4-24, Treatment 45 (bolded), with a Transmittivity and Diffuse Proportion of 0.5, is the closer value to weather station data, with a square error of 0.010.

Table 4-24 square errors of the treatments.

Diffuse Proportio	Atmospheric Trasmittivity									
	0.1	**0.2**	**0.3**	**0.4**	**0.5**	**0.6**	**0.7**	**0.8**	**0.9**	**1.0**
0.1	19.16	15.20	10.88	6.665	3.039	0.601	0.113	2.597	9.507	23.038
0.2	18.93	14.66	10.06	5.674	2.117	0.144	0.744	5.284	15.766	35.330
0.3	18.63	13.98	9.047	4.517	1.176	0.017	2.372	10.127	26.127	54.982
0.4	18.23	13.09	7.781	3.179	0.348	0.654	5.970	19.012	43.991	87.916
0.5	17.69	11.90	6.168	1.700	**0.010**	3.094	13.747	36.115	76.775	146.950
0.6	16.88	10.23	4.100	0.343	1.299	10.142	31.407	71.968	142.958	263.777
0.7	15.58	7.719	1.588	0.375	8.233	30.919	76.828	158.924	298.614	533.890
0.8	13.14	3.754	0.072	9.050	40.051	106.34	227.619	434.833	779.990	1356.87
0.9	7.072	0.342	23.58	103.94	279.11	603.57	1159.58	2078.55	3584.65	6087.86
1.0	Non valid results									

Figure 4-12 illustrates the sensibility of the solar radiation (Kwh/m^{2}day) to the atmospheric parameters. The solar radiation, graphed on the y-axis, increases proportionally to the Transmittivity, graphed on the x-axis. In addition, the solar radiation rises when the diffuse proportion (Dp), represented as nine lines that vary from 0.1 to 0.9, increases.

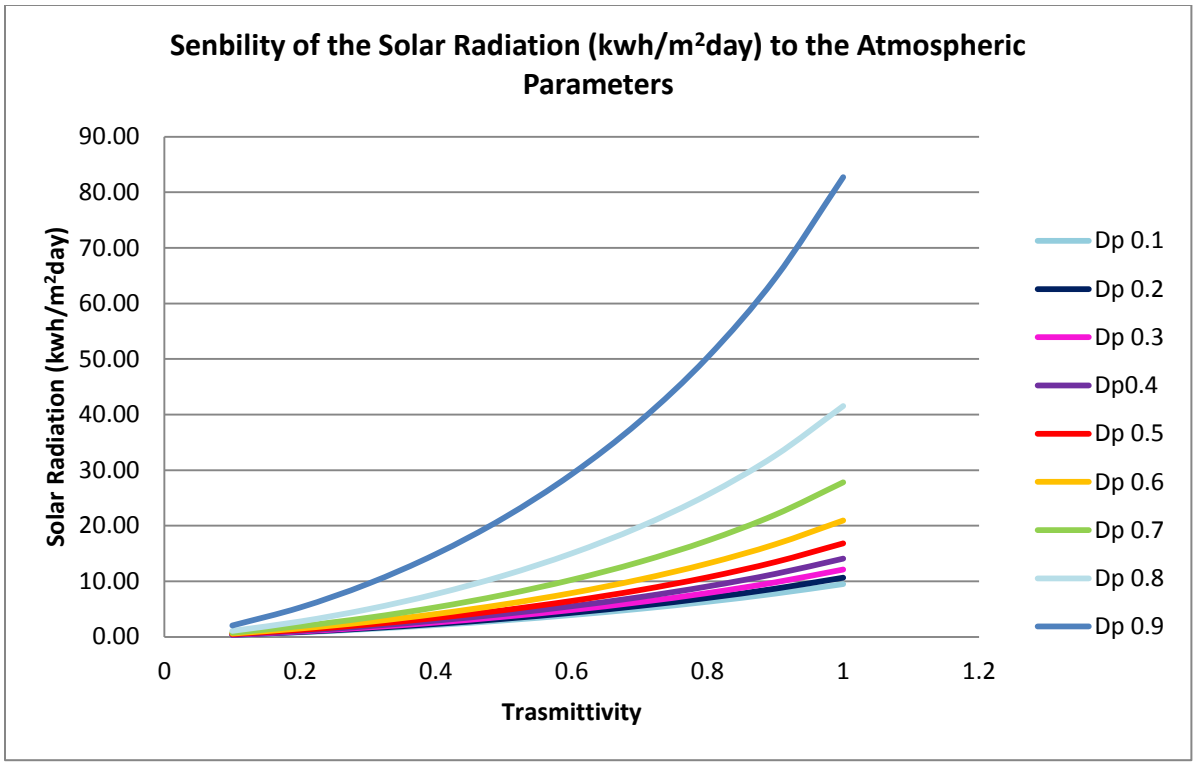

Figure 4-12 Sensitivity of the solar radiation to the atmospheric parameters. Dp: diffuse proportion.

Monthly Results

Every month returns different combination of parameters as being the most suitable for calibrating the model; they are described in Table 4-25. T7 seems the most appropriate for November, December and January; T16 for March, April, May, and June; T26 for February, July, August and September; T36 for October; and T45 obtained the best yearly results. The best treatments for each month are in bolded (Table 4-25), and a combined treatment was created with the monthly parameterisation that best fit the data of the weather station.

Table 4-25 Solar radiation from Best treatments (Kwh/m^2/day).

	Jan	Feb	Mar	Apr	May	Jun	Jul	Aug	Sep	Oct	Nov	Dec	Year
Weather Station	2.2	3	4.2	5.7	6.7	7.2	7.3	6.5	5.4	3.9	2.5	2	4.7
Treatment													
T7	**2.20**	3.19	4.80	6.43	7.56	7.86	7.89	6.95	5.56	3.59	**2.47**	**1.94**	5.04
T16	1.75	2.63	**4.09**	**5.59**	**6.63**	**6.92**	6.92	6.06	4.77	2.99	1.99	1.53	4.32
T26	2.03	**3.00**	4.59	6.21	7.32	7.63	**7.64**	**6.72**	**5.34**	3.40	2.30	1.78	4.83
T36	2.41	3.50	5.26	7.03	8.25	8.57	8.61	7.59	6.09	**3.94**	2.71	2.12	5.51
T45	1.91	2.91	4.56	6.22	7.38	7.71	7.70	6.75	5.31	3.32	2.18	1.66	**4.80**
Best Monthly Treatment	**7**	**26**	**16**	**16**	**16**	**16**	**26**	**26**	**26**	**36**	**7**	**7**	
	2.20	3.00	4.09	5.59	6.63	6.92	7.64	6.72	5.34	3.94	2.47	1.94	4.71

If the Solar Analyst tool were calibrated on a monthly basis, using each moth the combination of parameters return the closer values to the weather station measurements, the yearly result would be better than a yearly calibration with T45. This is demonstrated in Table 4-26 which presents the square differences between the results modeled values presented in Table 4-25 and the weather station data. The lowest yearly square error is from the Best Monthly Treatment (4E- 5) followed by that of T45 (0.010) and T26 (0.017).

Table 4-26 Square difference between best treatments and weather station data.

T	Jan	Feb	Mar	Apr	May	Jun	Jul	Aug	Sep	Oct	Nov	Dec	Year
7	0.000	0.036	0.356	0.534	0.741	0.439	0.346	0.200	0.024	0.098	0.001	0.004	0.113
16	0.205	0.136	0.012	0.013	0.005	0.077	0.146	0.197	0.400	0.828	0.265	0.225	0.144
26	0.029	0.000	0.154	0.257	0.390	0.185	0.118	0.046	0.004	0.253	0.041	0.048	0.017
36	0.043	0.252	1.128	1.774	2.414	1.890	1.722	1.199	0.479	0.002	0.045	0.015	0.654
45	0.083	0.007	0.128	0.275	0.462	0.258	0.162	0.061	0.007	0.338	0.102	0.113	0.010
BMT	**7**	**26**	**16**	**16**	**16**	**16**	**26**	**26**	**26**	**36**	**7**	**7**	
	8E-07	2E-05	1E-02	1E-02	5E-03	8E-02	1E-01	5E-02	4E-03	2E-03	6E-04	4E-03	4E-05

T:Treatment
BMT: Best Monthly Treatment

The monthly results are illustrated in Figure 4-13. T45 is the treatment that returns the lower yearly square difference (0.010) compared with the weather station (Table 4-26). However, T45

tends to overestimate solar radiation during the warmer months from March to September; the squared differences between the modeled and measured values varies between 0.07 and 0.462 (Table 4-26). In contrast, during the months from October to April, T45 tends to underestimate solar energy; the squared difference between the model T45 and the weather station varies between 0.07 and 0.338 (Table 4-26).

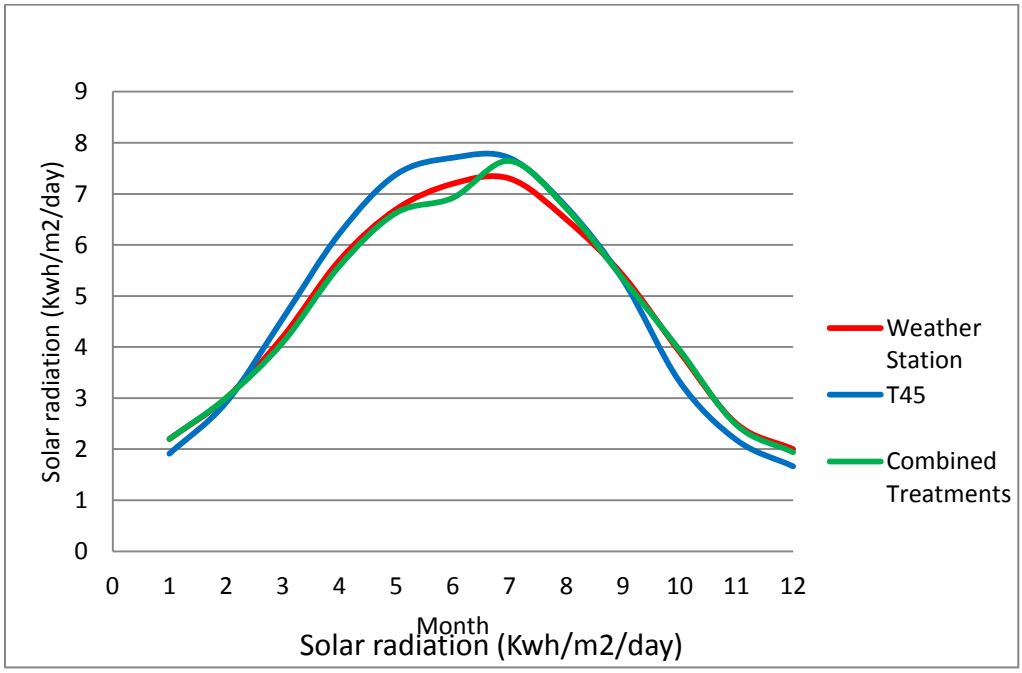

Figure 4-13 Monthly solar radiation

On the other hand, adjusting the atmospheric parameters in a monthly basis (combined treatment) yield a yearly result closer to the weather station measurement than that of T45 (Figure 4-13). Because the atmosphere conditions (humidity, temperature, solar radiation) vary throughout the year, it is reasonable that the atmospheric parameters require adjustments throughout the months. However, T45 was selected to calculate the yearly solar radiation because it is more time and computationally efficient, and T45's yearly result is considered close enough to the weather station measurement (squared error = 0.010).

4.2.3 Model Assessment

T45, the selected treatment (Transmittivity 0.5 and Diffuse proportion 0.5), was run for the full scene, and the results were tested against the values measured by the solar collectors at tilts of 0, 22, 37, 52, and 90. The model assessment involves finding the locations with conditions similar to those of the solar collectors at places that are shade-free, facing south, and with slopes corresponding to the tilt of the solar collectors. Because the exact slopes corresponding to these tilts could not be found, they were interpolated from the closest tilts: 0, 19, 26, 35, 38, 51, 54, and 89. The shade-free places were found by building image histograms for each tilt (facing south) and selecting the $2/3^{th}$ upper part of the histogram peak. Table 4-27 summarises characteristic of the peak values for every tilt; the threshold were computed as the minimum of the peak plus 1/3 of the range; the values over the threshold were considers as shade-free.

Table 4-27 Characteristic of the solar energy picks (wh/m^2day)

	Tilts							
	0	**19**	**26**	**35**	**38**	**51**	**54**	**89(*)**
Min	4123	4159	4177	4168	4237	3160	2751	2132.8
Max	4943	4937	4933	4880	4931	4868	4791	2666
range	820	778	756	712	694	1708	2040	533.2
Pick value	4533	4548	4555	4524	4584	4014	3771	
Threshold	4396	4418	4429	4405	4468	3729	3431	2311
(*) At 89 degrees not enough points were found to build histogram; thus the range was consider to be 20% of the maximum.								

Image statistics were computed for places with conditions similar to the solar collectors; these values are presented in Table 4-28, and the standard deviation tends to increase proportionally to the tilt. In addition, by comparing these image statistics with the statistics of the analysis using the default parameters (Table 4-22) is possible to appreciate that when the amount of energy

increases, the standard deviation increases as well. That indicates that at larger energy amounts, the variability increases and more samples are required to calibrate the model.

Table 4-28 Image statistics of the solar energy values (wh/m^{2}day) on places facing south and shade-free using atmospheric parameters of T45

	Tilt							
	0	19	26	35	38	51	54	89(*)
min	4396	4418	4429	4405	4468	3729	3431	2326
max	4943	4937	4933	4880	4931	4868	4791	2666
mean	4535	4593	4587	4539	4628	4121	3840	2429
stand deviation	80.1	105.5	98.4	83.8	98.4	233.3	247.35	87.8
(*) At 89 degree the image is composed by few values.								

The values corresponding to the tilt of the solar collectors were interpolated from values in Table 4-28 and are presented in Table 4-29. This allows comparing the modeled solar radiation to that measured by the weather station (Table 4-29). The solar energy measured by the weather station is closer to the mean, at tilt 0; however, at higher tilts, the weather station values are closer to the maximum modeled values. This is confirmed by the correlations: between weather station and maximum it is 94% and between weather station and means it is 93%.

Table 4-29 Interpolated solar energy values (wh/m^{2}day) for places shade-free and facing south

Solar Radiation (wh/m^2/day)	Tilt					Correlation with weather station values
	0	**22**	**37**	**52**	**90**	
Weather Station	4700	5300	5400	5100	3400	
Model Minimum	4397	4424	4480	3775	2289.3	0.91
Model Mean	4535	4590	4598	4027	2389	0.93
Model Max	4943	4935	4914	4842	2605	0.94

Figure 4-14 displays in green the values measured by the weather station, and the modeled values are in yellow, the minimum, in red, the mean, and in blue, the maximum. At tilt 0, the

mean is closer to the weather station values; however, at higher tilts, the model tends to underestimate the solar radiation values.

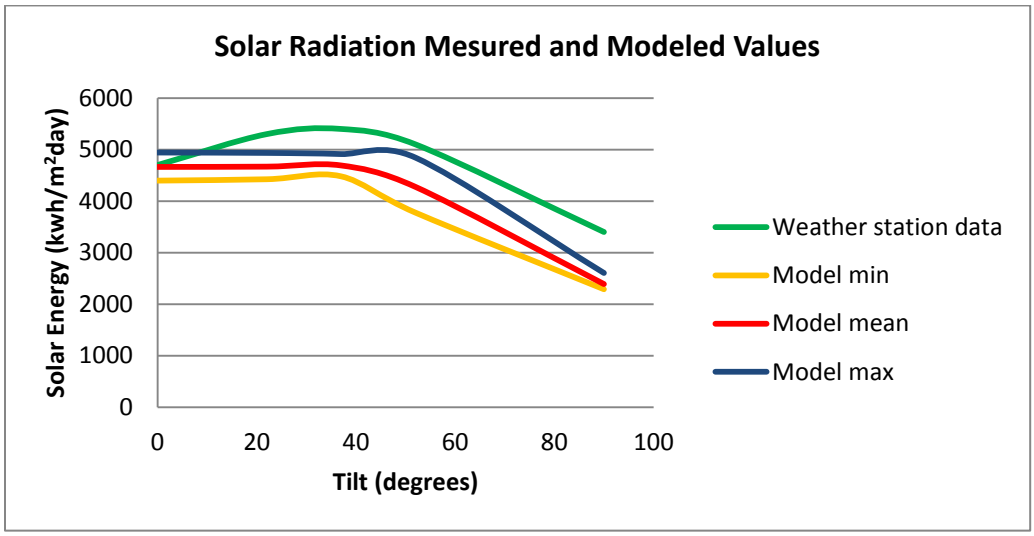

Figure 4-14 Solar energy (wh/m^2day) at different tilts measured and modeled values.

Table 4-30 portrays the errors between the modeled and measured values; when the tilt increases the error increases as well. At tilt 0, the mean values return smaller errors; however, at higher tilts, the maximum modeled values return lower errors.

The percentage errors of the mean (Table 4-30) vary from 3.5% to 29.7% according to the tilt.

Table 4-30 Error estimated for the solar Radiation model T45

Error						
Tilt	0	22	37	52	90	Sum
Min	304.0	877.3	953.0	1470.3	1105.6	4710
Mean	165.0	709.6	801.7	1072.7	1011.3	3760
Max	-243.0	364.7	486.0	257.7	794.7	1660
Percentage Error						
Tilt	0	22	37	52	90	Sum
Min	6.5	16.6	17.6	28.8	32.5	19.7
Mean	3.5	13.4	14.8	21.0	29.7	15.7
Max	-5.2	6.9	9.0	5.1	23.4	6.9

Among the models, T45 returns the solar radiation closer to the value measured by the weather station. That is evident in Table 4-26 where is possible to confirm that T45 returns the lower yearly squared error, 0.010. Thus, T45 is considered the best treatment, and its combination of parameters was run for the whole scene. Figure 4-15 presents the resulting solar radiation map. This image represents, in blue, the lower solar radiation values that usually correspond to vegetation, such as the Bayview Park at the east of Candlestick stadium, and the parks Hilltop and Adam Rogers at the north of the study area. The map represents in orange the higher energy amounts, which corresponds mainly to the industrial zones at the north, south, Bayview and coast sector.

Solar Radiation map T45

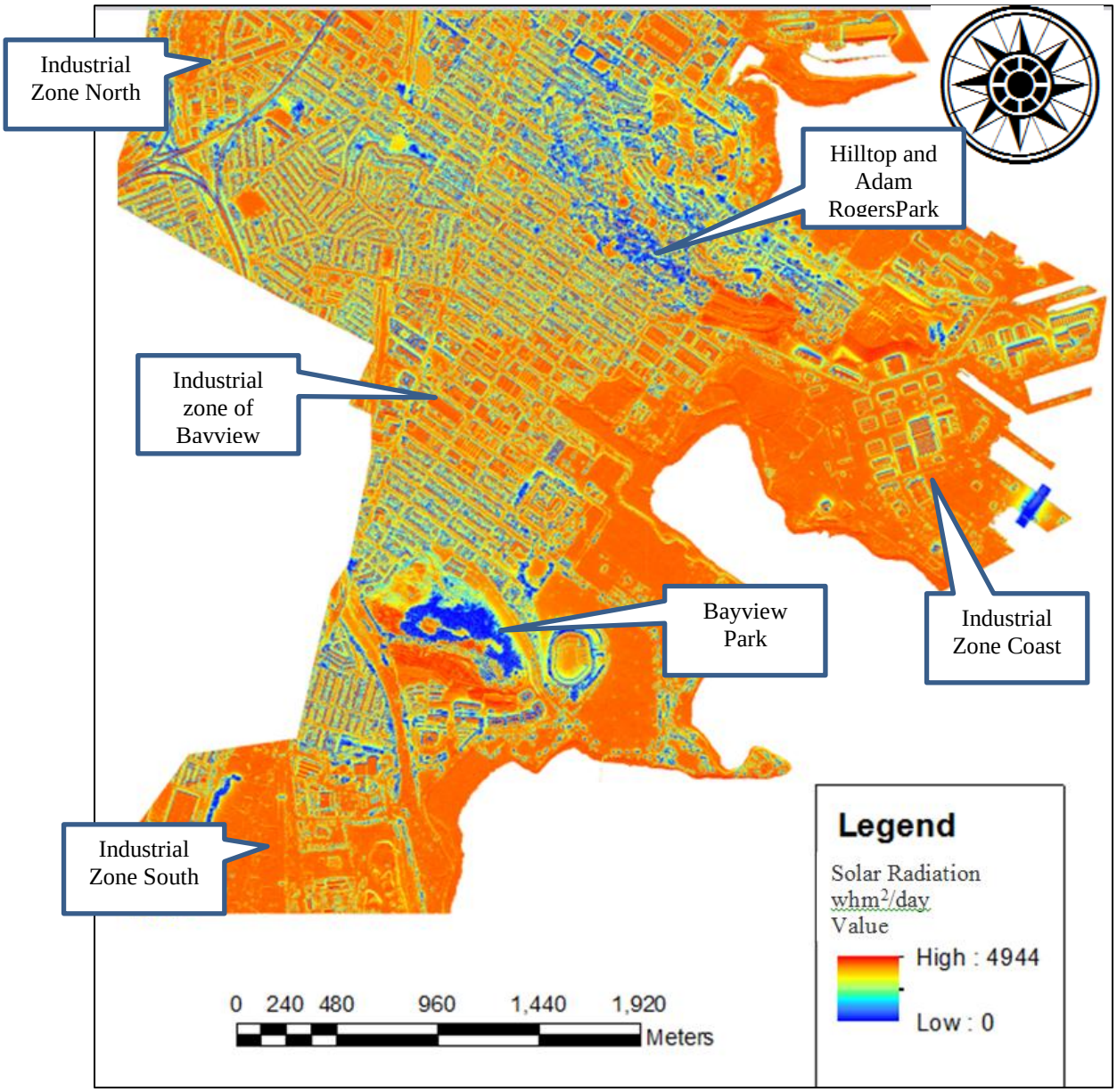

Figure 4-15 Solar radiation map for the full scene

4.3 Results of Estimations at Building Scale

This section is divided in two parts. The first part estimates the solar potential of buildings, expresses this amount in economic terms, as the cost of buying this energy from a local distributor, and finally, estimates the environmental benefits, as the amount of CO_2 that would be released to the atmosphere if the same amount of energy were produced by burning fossil fuels. The second part estimates the solar energy distribution throughout the day.

4.3.1 Estimation at Building Scale

In order to estimate the solar potential of buildings, first, the selected solar radiation model (T45) is calculated for the full scene (Figure 4-15). This solar radiation map is masked into the building outlines obtained with DT3 (Figure 4-16). The resulting image is presented in Figure 4-16, which is the basis of the calculus at building scale. The image representing the solar radiation at the rooftops is the basis of the calculus at building scales as is explained in the following section.

Solar radiation of the Rooftops

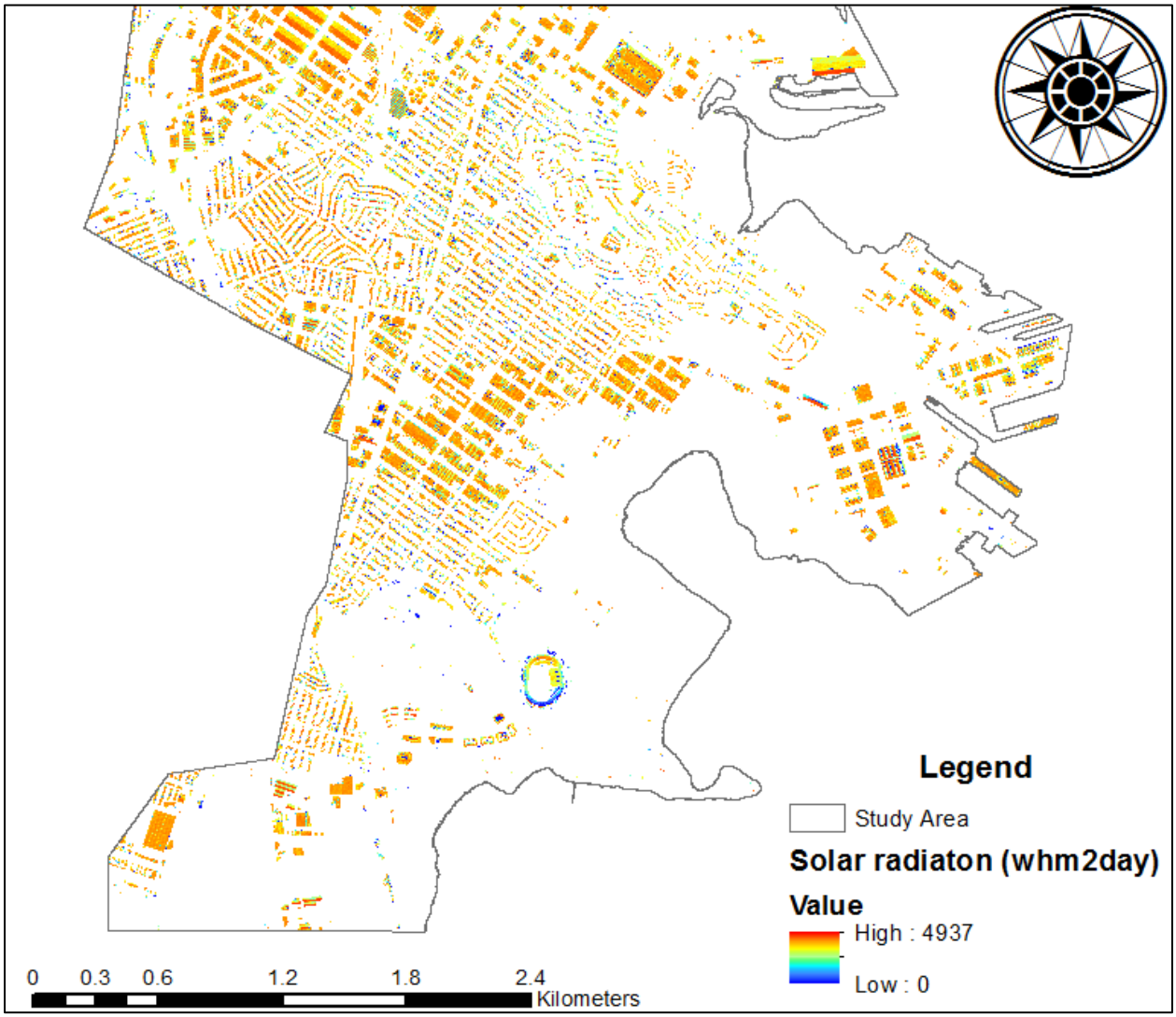

Figure 4-16 Solar radiation map masked by the building detection by T25 (DT3 using the predictors NDVI and PA)

Once the solar radiation map is masked by the building outlines (extracted in DT3), the resulting image represents the solar radiation received by the building rooftops (Figure 4-17).

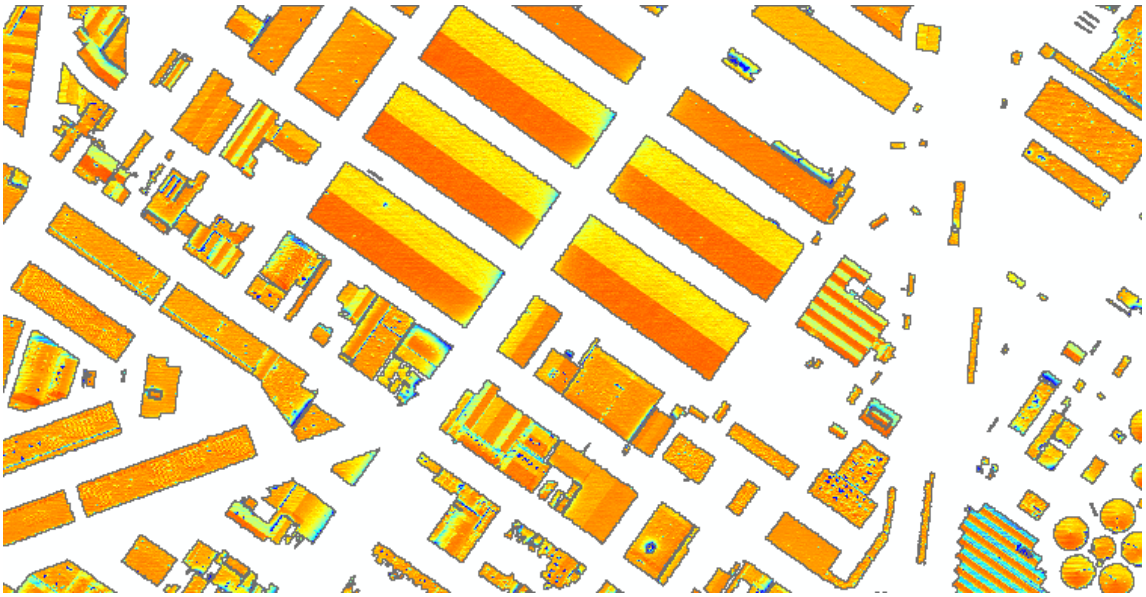

Figure 4-17 Solar radiation of the rooftops

Then, an image histogram is built for the building roofs (Figure 4-18). The most suitable zones for installing solar panels are chosen from the upper two thirds of the histogram peak; values greater than 4417wh/m^{2}day are considered shade-free and they are highlighted in light-blue in the histogram (Figure 4-18) and in the image (Figure 4-19).

Figure 4-18 Image histogram of the rooftops

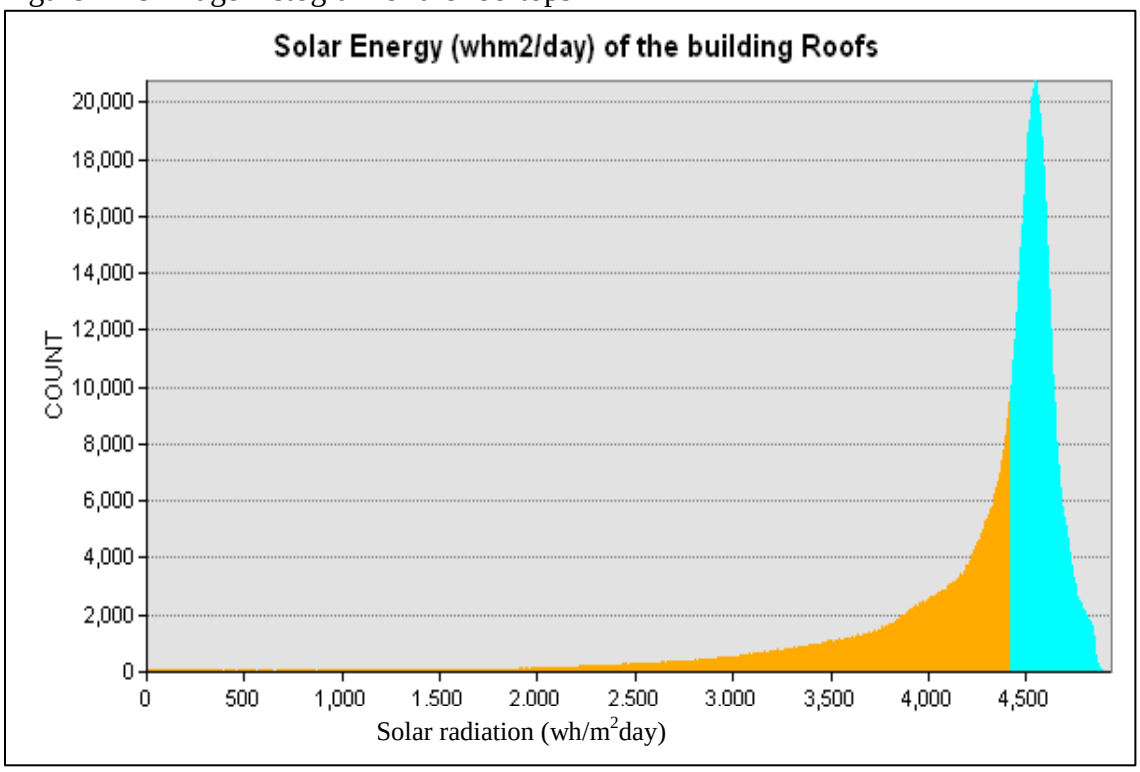

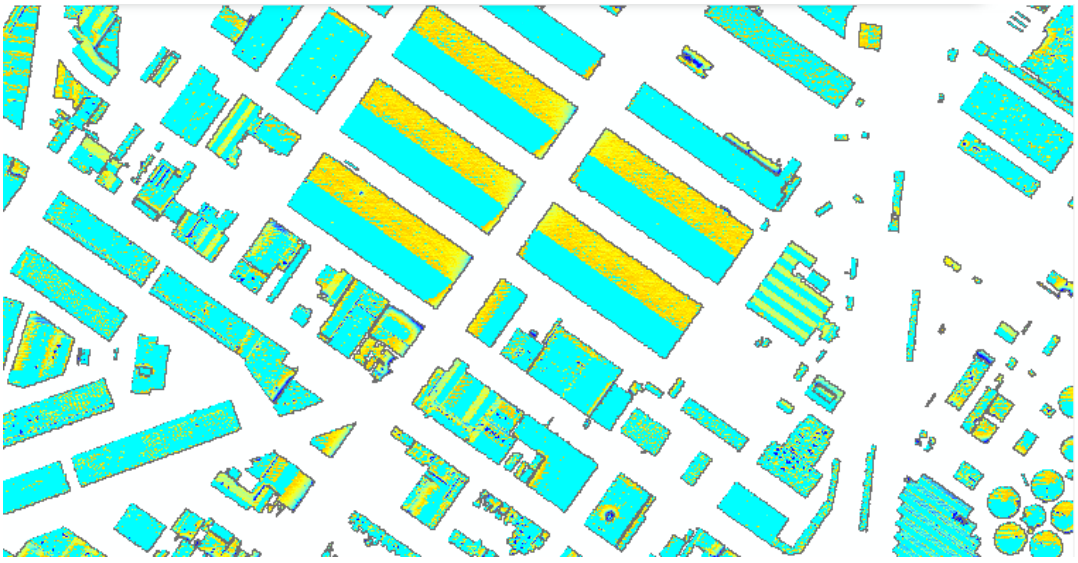

Figure 4-19 Shade-free Areas from the rooftops

In addition, the areas suitable for installing Photovoltaic panels (PV) should be equal to or greater than $4m^2$. Consequently, a building may have many suitable areas inside (Figure 4-20). The energy produced by each area is estimated by (3-7); and the energy harvested by each building is estimated as the sum of the areas inside that building, (3-8)

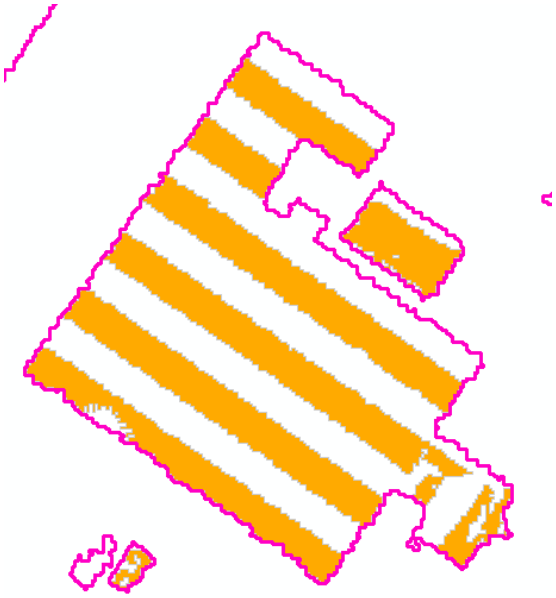

Figure 4-20 Suitable areas to harvest energy

The environmental benefits of installing PV on a building are estimated as the CO_2 released to the atmosphere if the same amount of energy were generated by burning fossil fuels; it is estimated by (3-9). The cost of the energy produced by every building, if this energy were purchased from a local distributer, was computed by (3-10). The results of this calculus are set on the shape file containing the buildings; thus, each individual building can be accessed from the map, using the identify function, to know its potential solar energy, the cost of buying this

energy, and the environmental benefits to install solar panels in the most suitable zones of the building (Figure 4-21).

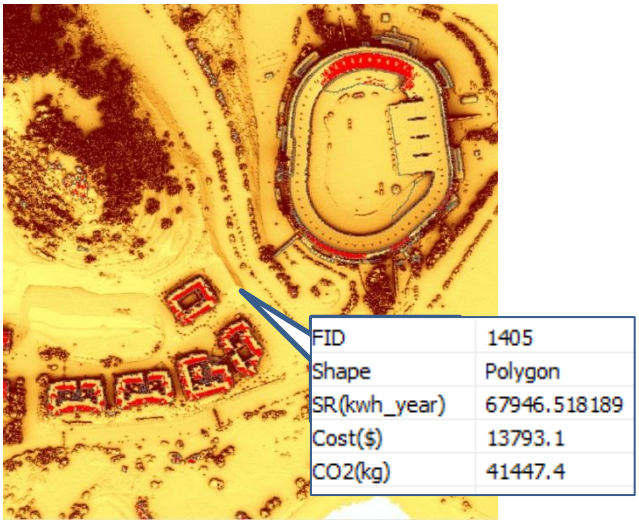

Figure 4-21 Accessing the information of each building

Considering the total number of buildings detected (5560), the total energy that can be harvested in a year is 104,909,378 kwh, which has a value of $ 21,296,603, and reduces the CO_2 emissions by 63,994,728 kg, as is summarised in Table 4-31. Summary of estimations at building scale

Table 4-31. Summary of estimations at building scale

kwh/year	Cost ($)	CO_2 (kg)
104,909,378	21,296,603	63,994,728

In Figure 4-22, the map represents the potential solar energy that each building would be able to harvest in a year using PV panels. In red are the buildings that harvest more than 500,000

(kwh/year), corresponding to the biggest industrial structures. In orange are the constructions that generate between 180,000 and 500,000 (kwh/year), corresponding to medium industrial buildings. In yellow are the structures generating between 100,000 and 180,000 (kwh/year), corresponding to small industrial edifices. In light-blue are the buildings harvesting between 11,000 and 100,000 (kwh/year), corresponding to residential areas, specifically, constructions that are adjacent to each other and that were detected as a single structures. In blue are the constructions able to generate more than 0 but less than 11,000(kwh/year), corresponding to single detached houses. Buildings labelled as 0 kw/year did not present areas large enough (more than $4m^2$) able to achieve high energy rates (4417 wh/m^2day); these constructions are represented in black.

From the map (Figure 4-22) it is possible to infer that industrial zones (highlighted with arrows) would be more efficient energy producer than residential areas, in addition, it is possible to identify the most productive buildings.

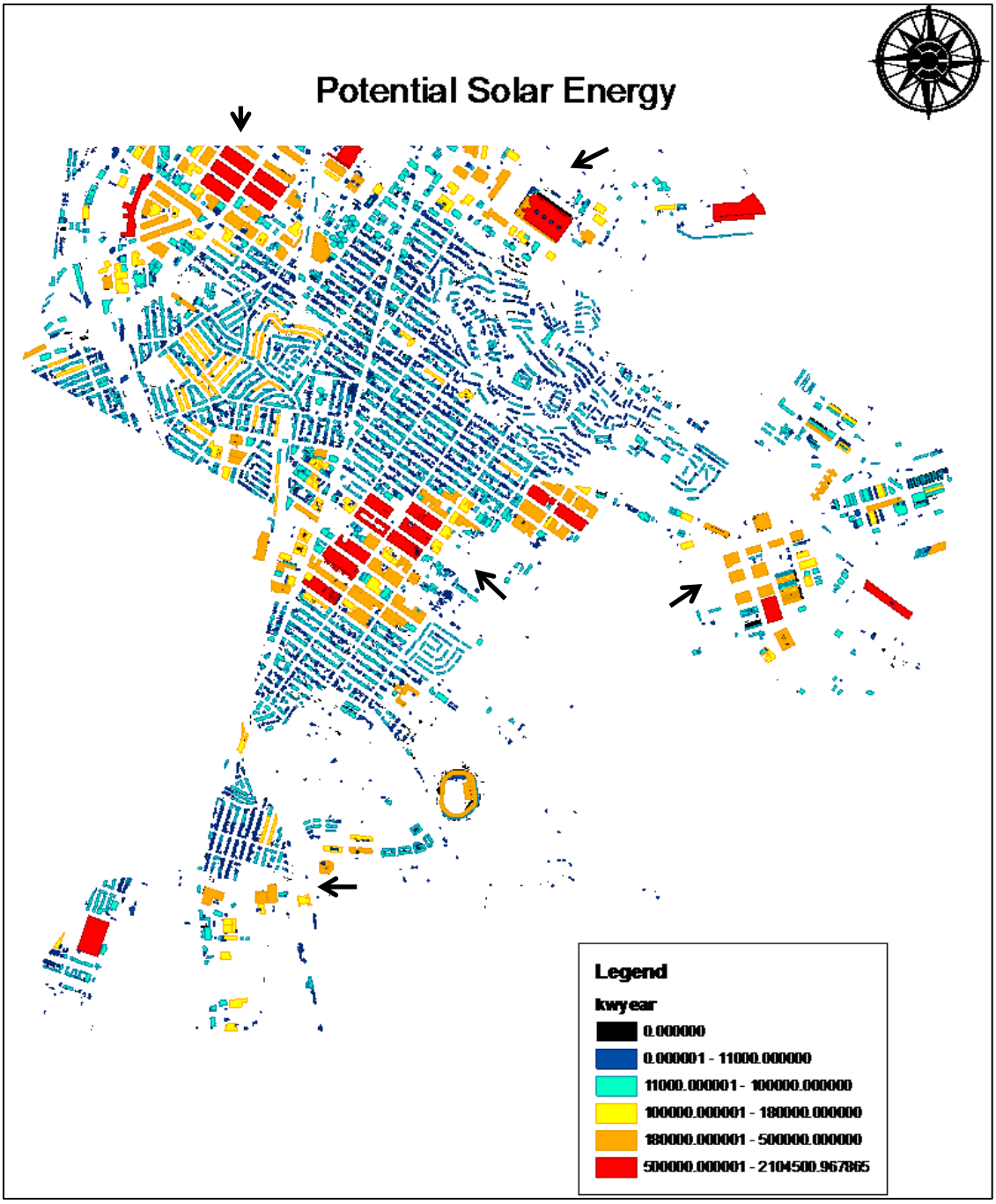

Figure 4-22 Potential solar energy map, the industrial zones are pointed with and arrow.

4.3.2 Distribution of the Solar Energy During the Day

As a fist approach to explore the distribution of the solar energy throughout the day, sixteen buildings were selected (Figure 4-23) as subject of the analysis. They were selected with different tilts and orientation, and then it is expect the result would be more representative. The Solar Analyst tool was carried out (over the sixteen buildings) on the 15th day of every month, at intervals of one hour, utilising the atmospheric parameter from T45.

Figure 4-23 Building for the analysis of energy daily distribution

In Figure 4-23, it is possible to appreciate that the selected constructions (delineated in red), correspond to a residential area. They have different orientations and roof inclinations. In addition, the zones that receive more than 4417 (wh/m^{2}day) are highlighted in light-red.

The hourly average of the sixteen buildings was used for the analysis of the daily distribution of energy.

Table 4-32 illustrate the hourly distribution of solar energy. The most productive months are Jun and July followed by May, August, April and September, with peak of harvesting energy occurring at 1:00pm. The coldest months of November, December, and January, are less productive and energy peak near 12:00pm.

Table 4-32 Distribution of the solar energy (wh/m^2) throughout the day

Time	Jan	Feb	Mar	Apr	May	Jun	Jul	Aug	Sep	Oct	Nov	Dec
6						1	1	1				
7				2	1	88	92	106	2			
8	1	1	2	110	98	287	295	316	111	1	1	1
9	67	90	108	320	305	501	509	525	314	98	74	61
10	192	249	300	523	517	687	692	695	502	271	209	175
11	294	387	475	682	697	825	826	806	641	422	320	266
12	342	469	596	780	823	904	898	851	714	519	378	306
13	329	485	652	809	886	918	905	827	717	549	372	285
14	256	434	637	769	882	867	847	737	650	510	305	209
15	142	324	553	661	812	756	727	586	519	408	189	100
16	29	172	410	497	681	592	556	392	339	255	59	11
17	0	32	226	295	500	393	353	181	140	88	0	0
18		0.02	54	96	291	185	147	23	10	1.24		
19			0	1	95	29	13	0.003	0.000			
20					1	0.0135	0.0002					
21												

Table 4-33 represents the perceptual distribution of energy measures on the 15th day of every month. During the whole year, energy peak occurred between 12 to 1pm. The most energy productive months are May, June, July and August; during these months, the harvesting period spreads throughout 9 hours. Unlike, the coldest months when the energy harvesting is concentrated in the 6 hours nearest to the energy peak.

Table 4-33 Distribution of the solar energy (%) throughout the day

Time	Jan	Feb	Mar	Apr	May	Jun	Jul	Aug	Sep	Oct	Nov	Dec
6	0	0	0	0	0	0	0	0	0	0	0	0
7	0	0	0	0	0	1	1	2	0	0	0	0
8	0	0	0	2	1	4	4	5	2	0	0	0
9	4	3	3	6	5	7	7	9	7	3	4	4
10	12	9	7	9	8	10	10	11	11	9	11	12
11	18	15	12	12	11	12	12	13	14	14	17	19
12	21	18	15	14	12	13	13	14	15	17	20	22
13	20	18	16	15	13	13	13	14	15	18	20	20
14	16	16	16	14	13	12	12	12	14	16	16	15
15	9	12	14	12	12	11	11	10	11	13	10	7
16	2	7	10	9	10	8	8	6	7	8	3	1
17	0	1	6	5	8	6	5	3	3	3	0	0
18	0	0	1	2	4	3	2	0	0	0	0	0
19	0	0	0	0	1	0	0	0	0	0	0	0
20	0	0	0	0	0	0	0	0	0	0	0	0

A summary of the analysis of the hourly distribution of energy is presented in Table 4-34. It indicates that the hours of maximum harvestable energy are from 10am to 4pm, overlapping with labour hours that represent the maximum demand for energy. In the winter time, the period of production is shorter and more concentrated in the peak hours. In contrast, during the warmest month of April to September, the harvesting period is longer and more evenly spread throughout the day.

Table 4-34 Daily energy production peaks

Time		**Jan**	**Feb**	**Mar**	**Apr**	**May**	**Jun**	**Jul**	**Aug**	**Sep**	**Oct**	**Nov**	**Dec**
from	to												
6	9	4.1	3.4	2.7	7.8	6.1	12.5	13.1	15.7	9.2	3.2	3.9	4.3
10	16	95.9	95.3	90.3	85.1	80.4	78.9	79.5	80.9	87.6	94.0	96.1	95.7
16	20	0.0	0.0	1.3	1.8	5.9	3.0	2.3	0.4	0.2	0.0	0.0	0.0

4.4 Chapter Summary

This chapter present the results of the building detection, solar radiation modelling and estimation at building scale. T25 was selected as the best treatment for building detection. T45 was selected as the best treatment to calibrate the solar radiation model. At building scale the methodology was able to answer the question proposed at in the introductory part.

CHAPTER 5 DISCUSSION

This chapter discusses the results of the building detection, solar modelling and estimation at building scale.

5.1 Discussion of Building Detection

This study carried out a building detection process as a basis of the calculus at building scale. The building outlines were extracted from the LiDAR data because that ensures a perfect match with the solar modelling (derived from the same data). In addition, LiDAR data are especially suitable for urban modelling because it provides precise and detailed information about the 3D structures, as Dorninger and Pfeifer (2008), Matikainen et al. (2003), and Rutzinger et al. 92006) have reported.

The building outlines were derived from the LiDAR data and not from the multispectral images as Levinson et al. (2009), Wigton et al. (2010), and City of Boston (2009) have done. This former approach was undertaken to avoid difficulties arising from the broad variety of rooftops and the spectral similarities between rooftops (especially flat roofs built in concrete) and other impervious surfaces that are not roofs (such as pavement).

Usually, a LiDAR building detection process is carried out on an object-based approach. The objects are generated by setting a height threshold. Then the buildings are separated from vegetation based on criteria of texture (local high differences) that can be measured by a Laplacian filter or Max Slope filter (Brandin and Hamren, 2003), Level Co-occurrence (Matikainen et al., 2003), or Homogeneity of Height (Rutzinger et al., 2006).

In contrast, this study uses an object-based approach to fuse LiDAR and satellite data and perform the building detection. That approach allows using the best characteristics of both datasets; LiDAR allows a highly precise extraction of the 3D forms, and multispectral imagery clearly distinguishes between land covers such as vegetation and impervious surfaces.

5.1.1 Statistical Analysis

The statistical analyses highlight NDVI and PA as the most efficient predictors for separating buildings from vegetation. That finding is coincident with Ünsalan and Boyer (2011), who consider NDVI as an excellent indicator to differentiate between vegetation and other land covers. Non other studies were found that use PA to separate buildings from vegetation.

The success of the combination of NDVI and PA to separate buildings from vegetation is that they are independent one from each other. NDVI is based on the object reflectance and it is an outstanding criterion to distinguish between vegetation and other land covers. However, because of offset issues (between LiDAR and multispectral imagery), NDVI is not able to detect one hundred percent of the building objects. On the other hand, PA is based on the object shape (derived from the Lidar data). It is the perfect complement for NDVI because PA is able to detect objects that NDVI cannot.

In addition, NDVI and PA tend to perform better when they are applied to large objects. A high levels of segmentation, the objects tend to be more irregular in their borders; thus, their rate perimeter area (PA) increases, and the PA of the buildings became similar to that of the vegetation; In the case of NDVI, probably when the object are smaller, the average NDVI is more affected by an offset between data sources (LiDAR and multispectral imagery). If the

predictors have different efficiencies at different object sizes, hierarchical classification has the potential to enhance the classification result.

These findings are broadly applicable to different tasks that require fusing of different data sources and performing feature extraction. For example, urban 3D models are useful to support governmental policies, planning, solar modeling, commercial analysis, virtual tours, and several others fields.

Independent sample t-test

The independent sample t-test is summarized in Table 4-19. This identified NDVI and PA as the most significant individual variables for separating building from vegetation. This significance arises because NDVI is an excellent criterion to separate vegetation from other land covers, and is only limited by the offset between the data sources. PA and Sobel are based on object geometry; however, PA seems to be a better predictor because Sobel fails when applied to separate small objects (DT2 and DT3 Class I). Finally, the average Area seems not to be significantly different between vegetation and building.

NDVI passed nine of nine t-tests performed, proving to be a consistent criterion for all the decision trees. PA passed seven of nine t-tests, confirming its usefulness for DT1, DT2, and Class II- DT3; PA is not so efficient in Class I-DT3 because this criterion tends to perform better for larger objects. Sobel passed four of nine t-tests. It seems to be a suitable criterion for DT1 and Class II-DT3; it is not efficient when applied to small objects (DT2 and ClassI-DT3). The variable Area passed two of nine t-tests for independent samples and so seems not to be an appropriate criterion for separating buildings from vegetation.

ROC curves and AUCs

The ROC curves (Figure 4-1, Figure 4-2, Figure 4-3 and Figure 4-4) indicate that NDVI and PA are the stronger predictors (for building detection), because their curves top the other criteria, especially for sensitivities greater than 90%.

On the other hand, the AUCs, summarised (Table 4-21), shows PA and NDVI as the stronger predictors for DT1. The Sobel criterion appears as the most significant variable for DT2 and ClassII-DT3. These results are not consistent with the t-tests. That is because Sobel AUC is misleading. Its strength is due to its efficiency up to 80% sensitivity (in DT2 and DT3). Sobel's efficiency drop drastically above 90% level of sensitivity, which can be verified in the ROC curves of DT2 (Figure 4-2) and DT3 (Figure 4-3 and Figure 4-4).

In addition, the AUC shows NDVI and PA criteria as better than Area, which is consistent with the ROC curve shapes (Figure 4-1, Figure 4-2, Figure 4-3, and Figure 4-4) and the results of the t-tests (Table 4-19). The AUC also suggests that NDVI and PA are more effective identifying larger objects. For example, in Table 4-21, DT1 presented higher AUCs than DT2 (which is more segmented), and Class II of DT3 presents greater AUCs than Class I of DT3 (which have smaller objects).

Thresholds and Accuracy assessment

The treatment, thresholds, and accuracy assessment results are summarised in Table 4-20. The combined criteria (NDVI OR PA) are selected for all the cases. That corresponds to T5, T15 and T25 for DT1, DT2 and DT3 respectively. This combination is selected because of their consistency in the t-tests, their ROCs shape, and their superior results in the accuracy

assessment. The combined treatments obtained better results, in the accuracy assessment, than individual variables. That is because the combine criteria use the logic operator "OR" that is the union of the results of both individual criteria.

In the accuracy assessment (Table 4-20), NDVI and PA tend to be more efficient for larger objects. This can be inferred because the lower levels of thresholds required detecting larger objects (Class II-DT3) and the higher levels of threshold required to detect smaller objects (Class I- DT3). This tendency can be explain: in the case of PA because at high levels of segmentation, the objects tend to be more irregular in their borders; thus, their rate perimeter area (PA) increase, and the PA of the buildings became similar to the vegetation; In the case of NDVI, probably when the object are smaller, the average NDVI is more affected by a offset between data sources (LiDAR and multispectral imagery).

Comparing the accuracy assessment, between decision trees, DT1 appears to be the most efficient method, with a 100% of presences and 44% of false positives (Table 4-20). However, by visual inspection it is possible to note that DT1 has several disadvantages arising from its low level of segmentation. On the other hand, DT3 obtained a more complete building detection than DT2, however, it introduced a large amount of false positives in the selection (Table 4-20).

5.1.2 Visual Inspection of Maps.

The visual inspection is a relevant criterion to choose a decision tree; it allows verifying effects of the segmentation and hierarchical classification, which are not evident on the statistical analysis. For example, Sobel segmentation allows better defining shapes, individualising adjacent structures, and distinguishing between overhanging features (such as a tree that hangs

over a building). Moreover, a hierarchical classification allows detecting better small buildings, however, it also include more noise (false positive).

For example, DT2 and DT3 include a Sobel segmentation that DT1 does not. That allows DT2 and DT3 a better definition of the object shapes, and moreover, permits separating between overlapping features. Figure 4-6-(a) shows the highway extraction of DT1, which includes adjacent buildings because of the impossibility of separating both objects. In this features DT1 differs from DT2 and DT3 (Figure 4-6-(b) and

Figure 4-6-(c), whose road selection do not include neighboring buildings. In addition, the road selection of DT3 (

Figure 4-6) includes smaller features belonging to the highway, which DT2 (Figure 4-6) do not include. DT3 can obtain more complete object detection because it allows different thresholds according to object size (Table 4-20).

In addition, complex shapes are roughly approximated by DT1. For example, in DT1, Figure 4-7-(a) the building shapes appear as a square. In contrast, in DT2 and DT3 (Figure 4-7 - (b) and Figure 4-7 -(c) respectively) presents buildings better defined. Moreover, DT3 Figure 4-7 -(c) introduces small features that are not present in DT2 Figure 4-7 - (b) because of the broad thresholds that DT3 assigned to the small objects (Table 2-1).

In other side, DT1 (because of its low levels of segmentation) tend to represent overhanging features as a single object. For example, a tree overlapping a building is represented by DT1 Figure 4-8-(a) as one object. In contrast, DT2 and DT3 (in Figure 4-8 -(b) and Figure 4-8 -(c) respectively) separate buildings from overhanging trees (and present better defined objects). In

Figure 4-8-(c), DT3 also includes more small elements than DT2 Figure 4-8 -(b), because the broad thresholds that DT3 use for small objects (Table 4-20).

Finally, comparing DT2 and DT3, both are re-segmented using Sobel criteria; DT3, with its broader threshold for smaller objects detected a 100% of buildings. Unlike, DT2, with its low threshold level reached at only 99% of buildings, but present less level of noise (false positives). This higher level of noise of DT3 compared to DT2 is evident comparing Figure 4-6-(b) to Figure 4-6 -(c) and Figure 4-7 -(b) to Figure 4-7 -(c), and Figure 4-8 -(b) to Figure 4-8 -(c) respectively.

In summary, DT3 is considered the best decision tree because the Sobel segmentation allows a better defining objects shapes, and separating adjacent and overlapping features; as was demonstrated by the visual inspection. In addition, DT3 it includes a hierarchical classification, which is suitable because the predictors tend to perform different at different object sizes. T25 was selected as the best treatment to perform the building detection, because it combines DT3 with the two stronger predictors NDVI and PA.

5.1.3 Precision of Feature Extraction

Even though LiDAR data are especially suitable for generating 3D city models because of this data already represents the structures, the precision of the product depends on several factors especially: the accuracy of the data, the object size and form, and the matching of the different data sources. The accuracy of the data sources utilised in this study was described on the introductory chapter and all the datasets met a high level of quality control.

The object size affects the precision of the building extraction because during the object generation a minimum size is set and also because the object size influences the performance of the predictors.

A minimum object size was defined as $20m^2$ in order to obtain a workable number of objects and exclude vehicles, which are similar to buildings in reflectance and shape. Then, during the object generation, objects smaller than $20m^2$ are merged into its larger neighbours, thus, the precision of the building detection is limited to objects larger than $20m^2$.

In contrast, the efficiency of the predictors decreases when the object size reduces. For example, the AUC summarised in Table 4-1 shows that PA obtains excellent results (90%) in DT3-ClassII (objects between 88 and $259m^2$), but it loses effectiveness (83%) in DT3-ClassI (objects smaller than $88m^2$). This change in efficiency occurred at higher levels of segmentation, the object's borders became irregular and the means (PA) of the building became similar to the means of vegetation. In addition, NDVI also decreases in AUC efficiency (Table 4-21) when the object size is reduced, because the means average of (NDVI) became more sensitive to mismatches of the data. The sensitivity of the predictor to the object size can be partially overcome by carrying out a hierarchical classification and adjusting the threshold according to the object size. For example, Table 4-20 illustrate that DT3 allows setting larger thresholds for the smaller objects.

The object shape is other factor influencing the precision of the building detection process, especially at low levels of segmentation. For example, DT1 roughly approximates complex building shapes, Figure 4-7-(a); this issue can be partially overcome by re-segmenting the objects with an edge detector as is done by DT2 and DT3 (Figure 4-7-(b) and -(c) respectively). Similarly, overhanging features such as a trees overlapping houses are usually detected as single

object by DT1, Figure 4-8-(a); however, the edge detector used by DT2 and DT3 help to separate and define the objects (Figure 4-8-(b) and -(c) respectively). Nevertheless, despite that help, adjacent buildings, such as townhouses, are always represented as a single object.

Finally, the integration of LiDAR data and satellite imagery is an important factor influencing the precision of building extraction. NDVI is an excellent criterion to distinguish between vegetation and constructions; however, integration pixel by pixel is difficult because, usually, there is some level of offsetting between the datasets. For instance, the outlines of the objects (derived from the LiDAR data) may not perfectly line up with the objects in the satellite image, Figure 4-5 - (b), from where the NDVI is derived.

In this study this issue is overcome through two strategies: an object oriented approach and combining a predictor based on the reflectance (NDVI) with a predictor based on the geometry of the object as are: PA, Sobel, and Area. These two strategies were successful in integrate the LiDAR data and satellite imagery because the object oriented approach does not require a perfect pixel by pixel match; it only requires that the predictors be (in average) significantly different between groups (building and vegetation). In addition, the combination of two predictors based on different sources such as NDVI (based on object reflectance) and PA (based on the object geometry) ensures a high efficiency in the building detection process.

5.2 Discussion of Solar Modelling

This study carried out a GIS solar modelling based on LiDAR data, which provides precise and detailed information of the 3D structures of the rooftops. Then, the model accounts for the shade, tilt, and orientation effects given by the real topography. Many studies estimates solar radiation

based on the cadastral outlines, assuming flat roofs, and using reduction factors for stand for shade orientation and tilt. (Chaudari et al., 2004, City of San Francisco, 2013, and City of Boston, 2009). However, a solar modelling based on the real 3D structure of the rooftops can gives a more price estimation of the potential solar energy that each building can harvest.

The solar radiation model is based on three assumptions: the values measured by the weather station represent the true solar radiation of San Francisco; the solar panels would be set in a flat position (with respect to the roof), and the upper two third part of the histogram peak (derived from the solar map) represent regions shade-free.

This study assumes that the weather station data represents the true solar radiation values of San Francisco, and uses them to calibrate the model. However, the NSRDB identified an uncertainty of 9% based on quantification of random and systematic errors. The random error is due to independent influences during measurements, and is different in every measurement process. The systematic error is due to a procedure or instrument and it is present in every measurement; this error is fixed and repeatable. Because the large sample size for this data set, random error is minimum and uncertainty is mostly systematic.

The second assumption is that the solar panels would be in a flat position with respect to the roofs; however, considering the possibility to tilt and orient panels, higher solar radiation values may be obtained. In addition, the modeled values do not vary with tilt at the same rate that data measured by weather station does (Figure 4-14). Thus, modeled solar radiation values are expected to be more precise at lower tilts. For example, at tilt 0, the error is 3%, and at tilt 90, the error is 29% (Table 4-30).

Calibration model T45 tends to underestimate solar radiation a high tilt levels. More precise results can be obtained by calibrating every month with an individual combination of atmospheric parameters, according with its specific conditions. However, this study chose an annual calibration because is more time and computationally efficient due to the large of the scene, in addition the annual result was considered sufficiently accurate.

The third assumption is that the top two thirds parts of the histogram peak represent the zones shade-free. The threshold was found by analysing the yearly average masked by the building outlines. The idea behind using a masked version of the solar map is to obtain an image free of noises, one that represents only the solar energy received by the buildings, non by vegetation or ground.

The thresholding process pretends to label the pixels, from the areas shade-free, which receive the highest amount of energy as suitable for installing solar panels and others as not adequate. This process can be carried out for an individual building or for the whole image; an individual threshold allows to find the cut value that fit better for a specific building. However, this study chose a general threshold because it allows comparisons between buildings, determinations of which one is the more efficient for energy harvesting. In addition, the threshold allows the identification of the best places to locate solar panels, usually the building owners do not cover the whole roof with panels, and they rather prefer to install the PV in the most efficient places.

In order to select this threshold, statistical parameters such as the median and the mean were considered, however, these parameters were discarded because these are central measurements, and the segmentation is looking for extremely high value. Then, a more sophisticated approach was taken; an image histogram was created (Figure 4-11), and the threshold was found by

analysing its shape. The objective of the threshold is selecting the area shade-free that retrieve the highest amount of energy; including as many pixels as possible. Then, because the peak of the histogram is located among the higher values, the threshold was set, by image observation at the initial two third parts of the peak. Figure 4-18 shows the image histogram and the selected threshold; Figure 4-19 shows the corresponding places shade-free, in the image. The pixel values equal or higher than the threshold were labelled as the best areas (for installing solar panels).

5.3 Discussion of Estimations at Building Scale

The estimations at building scale involve the amount of energy that each building can harvest by installing solar panels, the cost of buying this energy from a local distributor and the reduction on the CO_2 emissions that this panels produce. These calculi are based on the building outlines and solar model obtained in the previous sections, and then are under of the same limitations and constrain than these process.

In addition, the estimation of the potential energy harvested by each area (3-7) applied the same module coverage (65%) to all type of constructions. However, industrial buildings tends to present more percentage of surfaces available to set solar panels, then probably, a coverage factor customised by building type may obtain a more accurate result.

Other efficiency factors can be customised to local condition, knowing for example, the specific type of solar panel that will be installed and the local cost of the energy.

5.4 Chapter Summary

This chapter discuss the results presented in chapter 4. T25 was selected to carry out the building detection because of it combines the best decision tree and the stronger predictors. DT3 is considered the best decision tree because its good levels of object-shape definition. In addition, the Sobel segmentation allows DT3 to separate overlapping elements such as building and trees. Moreover, the hierarchical classification allows DT3 to maximize the number of building detected.

T45 was selected to carry out the solar modelling because of its high levels of precision. Among the annual treatments T45 obtained the smaller amounts of error. On other hand, an annual calibration was preferred to a monthly calibration; because it is more time and computationally efficient.

At building scale, the methodology proposed was able to answer the questions of how much energy each building can produce, and what is the significance of this energy in economic and environmental terms. In addition, the best places to locate solar panels (in each building) were found. Finally, the information at building scale allows comparing between buildings efficiencies.

CHAPTER 6 CONCLUSIONS AND RECOMMENDATIONS

This chapter offers the conclusions of this study, describes its limitations and present some suggestions for future studies.

5.1 Conclusions

Solar radiation is a clean renewable energy that addresses the two main challenges of our times: energy scarcity and global warming. The implementation of solar panels involves benefits such as providing economic saving, diversifying energy sources, reducing the electric demand on the central system, limiting the use of fossil fuels and reducing the greenhouse emissions. However, before installing solar panels, it is important to assess the energy that a building can produce and the best location to install them.

This study provides a methodology to semi-automatically estimate the energy that every building can harvest, in an area of 12 km^2 of the City of San Francisco. This energy was expresses as economic saving and environmental benefits. The method involves three main sections: building detection, solar modeling, and estimations at building scale.

The building detection process allows applying this methodology to any location, regardless of whether the area counts on cadastral outlines. In addition, a solar modelling based on the real 3D feature of each building allows a customised and realistic estimation that take into account the many factors that influence energy harvesting, such as roof area available, shade, orientation, tilt, and also the many loses of efficiency that the system may have.

This study found that an object-based approach allows a good integration between satellite and LiDAR data overcoming some offset issues that appear because of the large size of the study area and the elevation differences.

This thesis analyses the dependency of the building detection process on the object size. This analysis compares DT3 Class I (smaller objects) and DT3 Class II (larger objects). The statistical analysis (t-tests, AUC, ROC curves and accuracy assessment) indicate that the building detection process is more efficient when it is applied to larger objects (DT3 Class II), because smaller object are more sensitive to offset between data sources.

Moreover, this study examines the dependency of the building detection process on segmentation using an edge detector filter (Sobel). These analyses compare DT1 (without Sobel segmentation) to DT2 and DT3 (Sobel segmented). The statistical analyses (t-tests, AUC, ROC curves and accuracy assessment) show that the building detection process is more efficient when it is applied to objects with lower levels of segmentation (DT1). However, a visual inspection proved the value of the Sobel segmentation because DT2 and DT3 were found more precise in defining object-shapes. In addition, the Sobel segmentation allows DT2 and DT3 to separate between adjacent and overlapping features, such as, neighboring buildings or trees hanging over buildings.

The efficiency of the predictors was analysed by comparing them individually and combined. The statistical analysis (t-tests, AUC, ROC curves and accuracy assessment) determined that the stronger predictors were NDVI and PA. The interaction between these variables was highly positive; the combination of two predictors always yields higher stronger results than each individual variable.

T25 was identified as the best treatment to perform the building detection process, because it utilizes the stronger predictors and the best decision tree. The best combination was NDVI and PA. This combination succeeded because these predictors are independent of one another. NDVI is based on object reflectance and PA on object geometry, thus, their results are complementary. On the other hand, DT3 was identified as the best decision tree because of its flexibility in assigning different thresholds to different object sizes. The hierarchical classification of DT3 became especially relevant because the predictor perform different at different objects sizes.

The Solar Analyst tool is very suitable for modelling solar radiation at building scale; because it considers local factors such as orientation, tilt, shadow (cast by local topography), and weather conditions. The proper set of atmospheric parameters is crucial to obtaining accurate results. In addition, GIS solar modelling generates outputs continuous on the space.

The combination of atmospheric parameters T45 (Transmittivity 0.5 and Diffuse proportion 0.5) was identified as the best for the conditions of San Francisco, California. An annual calibration was preferred to a monthly calibration; because it was more computationally and timely efficient.

At building scale, this study proposes a methodology to assess the solar potential of each building. The methodology successfully generates information about the potential energy that each building can harvest, the cost of buying this energy from a local distributor, and the reduction on CO_2 emissions that this amount of energy represents. In addition, the most suitable areas to locate solar panels in were identified.

5.2 Limitations and Suggestions for Future Studies

One limitation in the building detection process was the object size, because this procedure is suitable only for buildings larger than $20m^2$. In addition, the efficiency of the predictors is higher when they are applied to larger object and detect the whole building population, imply introducing several false positives.

For future studies in building detection, would be appropriated trying a principal component analysis to separate buildings from vegetation, especially applied to the predictors NDVI and PA. Because in a rotated plane may be possible to obtain a more efficient thresholds.

In the solar radiation modelling, Arc GIS tool appears a very suitable as a base of the model; In addition, the calibration of the atmospheric parameters using weather station data is a practical approach. However, the process of 90 treatments was very tedious and time consuming task. The development of a tool for automates the calibration of the atmospheric parameter according weather condition would be very suitable and time saving.

At building scale, the efficiency factors were applied homogenously to all the building population. However, may be more accurate applied a larger module coverage to industrial buildings than a residential areas. That because the first tend to present more surface available to locate solar panels. Other efficiency factors can be customised knowing the specific conditions of the system such as the solar technology to be implement. Finally, other reductions on greenhouse emission can be estimated by considering gases such as sulfur dioxide, and nitrogen oxide.

REFERENCES

Almeida, A., and Landsberg, J.J., 2003. Evaluating methods of estimating global radiation and vapor pressure deficit using a dense network of automatic weather stations in coastal Brazil. *Agricultural and Forest Meteorology*, 118:237-250.

Angelis-Dimakis, A., Biberacher, M., Dominguez, J., Fiorese, G., Gadocha, S., Gnansounou, E., Guariso, G., et al., 2011. Methods and tools to evaluate the availability of renewable energy sources. *Renewable and Sustainable Energy Reviews*, 15(2), 1182–1200.

Ball, R.A., Purcell, L.C., and Carey, S.K., 2004. Evaluation of solar radiation prediction models. *North America. Agronomy Journal*, 96:391-397.

Bergamasco, L., & Asinari, P., 2011. Scalable methodology for the photovoltaic solar energy potential assessment based on available roof surface area: Application to Piedmont region (Italy). *Solar Energy*, 85(5), 1041-1055.

Bindi, M., and Miglietta, P., 1991. Estimating daily global radiation from air temperature and rainfall measurements. *Climate Research*, 1:117-124.

Brandin, M. and Hamrén, R., 2003. Classification of Ground Objects Using Laser Radar Data. Master Thesis. Linköping University, Department of Electrical Engineering. Retrieved from http://liu.diva-portal.org/smash/record.jsf?pid=diva2:18896

Chaudhari, M., Frantzis, L., and Hoff, T. E, 2004. PV grid connected market potential under a cost breakthrough scenario. Retrieved from http://www.ef.org/documents/EF-Final-Final2.pdf

City of Boston, 2009. Renew Boston Solar. Retrieved from http://gis.cityofboston.gov/solarboston/#

City of San Francisco, 2013. San Francisco Solar Map. Retrieved from City of Boston, 2009. http://sfenergymap.org/#

Colligon, J. S., (2006). The world energy crisis: Some vacuum-based solutions. *Vacuum*, 80 (10), pp. 1047

Coops, N.C., Waring, R.H., and Moncrieff, J.B., 2000. Estimating mean monthly incident solar radiation on horizontal and inclined slopes from mean monthly temperatures extremes. *International Journal of Biometeorology*, 44:204-211

Digital Globe, 2012. WoldView-2. Retrieved from: http://www.digitalglobe.com/downloads/WorldView2-DS-WV2-Web.pdf

Dorninger, P. and Pfeifer, N., 2008. A Comprehensive automated 3D approach for building extraction, reconstruction, and regularization from airborne laser scanning point clouds. *Sensors*, 8(11), 7323–7343.

Dubayah, R., and Rich, P. M. (1995). Topographic solar radiation models for GIS. *International Journal of Geographical Information Systems*, 9: 405–19

Dubayah, R., and Rich, P.M., 1996. GIS-based solar radiation modeling. pp. 129-134 In: M.F. Goodchild, L.T. Steyaert, B.O. Parks. C. Johnston, D. Maidment, M. Crane, and S. Glendinning (eds). GIS and Environmental Modeling: Progress and Research Issues. GIS World Books. Fort Collins, CO.

Filin, S., and Pfeifer, N., 2005. Neighborhood systems for airborne laser data. *Photogrammetric. Engineering Remote Sensing*. 71.(6), 743-755.

Filin, S., and Pfeifer, N., 2006. Segmentation of airborne laser scanning data using a slope adaptive neighborhood. *ISPRS Journal of Photogrammetry and Remote Sensing*, 60(2), 71–80.

Fu, P., and Rich, P.M., 1999. Design and implementation of the Solar Analyst: an ArcView extension for modeling solar radiation at landscape scales. *Proceedings of the 19th Annual Esri User Conference*, San Diego, USA. Retrieved from http://proceedings.esri.com/library/userconf/proc99/proceed/papers/pap867/p867.htm

Gadsden, S., Rylatt, M., Lomas, K., Robinson, D., 2003. Predicting the urban solar fraction: a methodology for energy advisers and planners based on GIS. *Energy and Buildings*, 35, 37–48

Geiger, R. J.,1965. The climate near the ground. Harvard University Press, Cambridge.

Green, M. A. 2004. Recent developments in photovoltaic. Solar Energy 76, no. 1-3 3–8.

Hofierka, J., and Kanuk, J., 2009. Assessment of photovoltaic potential in urban areas using open-source solar radiation tools. *Renewable Energy*, 34 (2009) 2206–2214.

Hofierka, J., and Suri, M., 2002. The solar radiation model for Open Source GIS: implementation and applications. Proceedings of the Open Source Free Software GIS-GRASS users conference 2002 - Trento, Italy. 11-13 September 2002.

Jwa, Y., Sohn, G., Tao, V., and Cho, W., 2008. An implicit geometric regularization of 3D building shape using airborne Lidar data. *ISPRS Archives*, 36(5), 69–76.

Kassner, R., Koppe, W., Schuttenberg, T. and Bareth, G., 2008. Analysis of the solar potential of roofs by using official lidar data. In: IAPRS, 37(B4), 399 – 403.

Kermel, F. 1988. Estimating hourly all-sky irradiation components from meteorological data. *Journal of Applied Meteorology*, 27:157-163.

Kriegler, F.J., Malila, W.A., Nalepka, R.F., and Richardson, W., 1969. Preprocessing transformations and their effects on multispectral recognition. Proceedings of the Sixth International Symposium on Remote Sensing of Environment, University of Michigan, Ann Arbor, MI, 97-131.

Kumar, L., Skidmore, A.K. and Knowles, E., 1997. Modelling topographic variation in solar radiation in a GIS environment. *International Journal of Geographical Information Science*, 11, pp. 475–497.

Levinson, R., Akbari, H., Pomerantz, M., and Gupta, S., 2009. Solar access of residential rooftops in four California cities. *Solar Energy*, 83(12), 2120-2135.

Ludwig, D., and McKinley, L., 2010. Solar Atlas of Berlin. *GIM International*. Retrieved from http://www.gim-international.com/issues/articles/id1504-Solar_Atlas_of_Berlin.html

Maas, H.G. and Vosselman, G., 1999. Two algorithms for extracting building models from raw laser altimetry data. *ISPRS Journal of Photogrammetry and Remote Sensing*, 54(2/3): 153–163.

Matikainen, L., Hyyppa, J. and Hyyppa, H., 2003. Automatic detection of buildings from laser scanner data for map updating. International Archives of Photogrammetry, Remote Sensing and Spatial Information Sciences, 34(3/W13).

Meteotest, 2008. Meteonormversion 6.1. Handbook. Retrieved from: www.meteonorm. com.

Miller, E., Shepard, S., Grond, K., Kellet. R., Miller, N., Pond, E., Schorth, O, Tooke,.R.,Vander Laan, M., Blundell, S. Khan. S., Solomon,R, 2011. Visualizing urban futures: Geomatic Decision support for Canadian cities report I: Literature review. Retrieved from http://www.citiescentre.utoronto.ca/Assets/Cities+Centre+Digital+Assets/pdfs/Research/TSI201/TSII201litreviewfull.pdf

Morgan, M. and Tempfli, K., 2000. Automatic building extraction from airborne laser scanning data. *ISPRS Archives*, 33(B4): 616–622.

NASA, 2006. The Energy of the sun. Retrieved from http://www-spof.gsfc.nasa.gov/stargaze/Sun7enrg.htm

National Solar Radiation Data Bases (NSRDB), 1992. Retrieved from http://rredc.nrel.gov/solar/old_data/nsrdb/1961-1990/redbook/sum2/23234.txt

O'Brien, W., Kennedy, Ch., Athienitis, A., and Kesik,T., 2010.The relationship between net energy use and the urban density of solar buildings. *Environment and Planning B: Planning and Design*, 37.6 1002-1021.

Panwar, N.L, Kaushik. S. C., and Kothari, S., 2011. Role of renewable energy sources in environmental protection: A review. *Renewable and Sustainable Energy Reviews*, 15: 1513-1524.

Rich, P.M., J. Wood, D.A., Vieglais, K., Burck, K., and Webb, N., 1999. Guide to HemiView: software for analysis of hemispherical photography. Delta-T Devices, Ltd., Cambridge, England.

Rigollier C, Lefevre M, Wald L., 2004. The method Heliosat-2 for deriving shortwave solar radiation from satellite images. *Solar Energy*, 77:159‑69.

Rutzinger, M.B. Hofle, B., Pfeifer, N. et al., 2006. Object based analysis of airborne laser scanning data for natural hazard purposes using open source components. *In the First International Conference on Object-based Image Analysis, Salzburg, Austria*

Sampath, A. and Shan, J., 2007. Building boundary tracing and regularization from airborne lidar point clouds. *Photogrammetric Engineering and Remote Sensing*, 73(7): 805–812.

Shapiro L. G. and Stockman, G. C., 2001. *Computer Vision*. New Jersey, Prentice-Hall.

Solomon, C.J., and Breckon, T.P., 2011 Fundamentals of Digital Image Processing. John Wiley and Sons, LTD.

SUN- AREA, 2013. Solar potential - roof cadastre. Retrieved from: http://www.sun-area.net/index.php?id=103

Suri, M., and Hofierka, J., 2004. A new gis-based solar radiation model and its application to photovoltaic assessments. *Transactions in GIS*, 8(2): 175-190.

Tooke, T. R., Coops, N. C., & Voogt, J., 2009. Assessment of urban tree shade using fused LIDAR and high spatial resolution imagery. Urban Remote Sensing Event, 2009 Joint (pp. 1–6).

U.S. Geological Survey (USGS), 2010. Retrieved from the metadata provides in the context of the IEEE GRSS 2012 Data Fusion Contest.

Ünsalan, C., and Boyer, K.L.(2011). Multispectral Satellite Image Understanding: From Land Classification to Building and Road Detection. London: Springer.

US Energy information administration (EIA), 2012. Retrieved from http://www.eia.gov/tools/faqs/faq.cfm?id=74&t=11

Wiginton, L. K., Nguyen, H. T., & Pearce, J., 2010. Quantifying rooftop solar photovoltaic potential for regional renewable energy policy. *Computers, Environment and Urban Systems,* 34(4): 345–357.

Yu, B., Liu, H., Wu, J., and Lin, W., 2009. Investigating impacts of urban morphology onspatio-temporal variations of solar radiation with airborne LIDAR data and a solar flux model: a case study of downtown Houston. *International Journal of Remote Sensing*, 30(17): 4359-4385.

APPENDIX A

Monthly square difference between modeled and measured Solar Radiation Values

Treatment	Jan	Feb	Mar	Apr	May	Jun	Jul	Aug	Sep	Oct	Nov	Dec	Year
1	4.7	8.5	15.7	27.5	36.7	42.2	43.9	35.7	25.9	14.3	6.0	3.9	19.1
2	4.3	7.3	12.5	20.9	27.3	31.4	33.1	27.4	20.8	12.4	5.4	3.6	15.2
3	3.5	5.6	8.8	14.2	18.1	21.0	22.5	19.0	15.2	9.8	4.4	3.0	10.8
4	2.5	3.7	5.2	8.0	10.0	11.8	13.0	11.3	9.6	6.9	3.2	2.2	6.66
5	1.4	1.8	2.1	3.2	3.8	4.8	5.5	4.9	4.6	4.0	1.8	1.3	3.04
6	0.5	0.4	0.3	0.4	0.4	0.7	0.9	0.9	1.2	1.5	0.6	0.5	0.60
7	0.0	0.0	0.4	0.5	0.7	0.4	0.3	0.2	0.0	0.1	0.0	0.0	0.11
8	0.7	1.5	3.4	4.9	6.2	5.3	5.2	4.0	2.4	0.6	0.8	0.5	2.60
9	3.7	6.0	11.0	15.0	18.5	17.0	17.2	13.9	9.8	4.2	4.1	3.0	9.51
10	10.9	15.7	25.0	33.0	39.9	38.5	38.7	31.9	24.3	12.7	11.7	9.5	23.0
11	4.7	8.4	15.5	27.1	36.1	41.5	43.2	35.2	25.6	14.2	6.0	3.9	18.9
12	4.2	7.1	12.0	20.0	26.1	30.0	31.7	26.3	20.1	12.1	5.3	3.5	14.6
13	3.4	5.3	8.1	13.0	16.4	19.1	20.5	17.5	14.1	9.3	4.2	2.9	10.0
14	2.3	3.2	4.3	6.7	8.2	9.8	10.8	9.5	8.2	6.2	2.8	2.0	5.67
15	1.1	1.3	1.4	2.0	2.4	3.1	3.7	3.4	3.4	3.1	1.4	1.0	2.12
16	0.2	0.1	0.0	0.0	0.0	0.1	0.1	0.2	0.4	0.8	0.3	0.2	0.14
17	0.1	0.4	1.2	1.8	2.4	1.9	1.7	1.2	0.5	0.0	0.1	0.1	0.74
18	1.7	3.1	6.4	9.0	11.3	10.1	10.2	8.1	5.3	1.8	1.9	1.3	5.28
19	6.7	10.2	17.5	23.7	29.0	27.3	27.8	22.7	16.7	7.9	7.3	5.6	15.7
20	17.8	24.7	37.5	48.8	58.7	57.6	57.8	47.9	37.6	20.9	19.1	15.9	35.3
21	4.7	8.3	15.2	26.5	35.4	40.6	42.4	34.5	25.2	14.1	6.0	3.9	18.6
22	4.1	6.9	11.4	19.0	24.6	28.2	29.9	25.0	19.3	11.7	5.2	3.5	13.9
23	3.2	4.8	7.2	11.4	14.4	16.8	18.2	15.5	12.8	8.6	4.0	2.7	9.05
24	2.0	2.7	3.3	5.1	6.2	7.5	8.4	7.4	6.7	5.3	2.4	1.7	4.52
25	0.8	0.8	0.6	0.9	1.0	1.5	1.9	1.8	2.0	2.2	0.9	0.7	1.18
26	0.0	0.0	0.2	0.3	0.4	0.2	0.1	0.0	0.0	0.3	0.0	0.0	0.02
27	0.5	1.2	3.2	4.7	6.0	5.1	5.0	3.8	2.2	0.5	0.6	0.4	2.37
28	3.7	6.1	11.6	16.2	20.1	18.5	18.9	15.3	10.7	4.4	4.1	2.9	10.1
29	11.7	17.3	28.2	37.8	46.0	44.0	45.1	37.2	28.2	14.5	12.9	10.0	26.1
30	29.1	39.3	57.4	73.7	88.2	87.7	87.8	73.3	58.8	34.4	31.1	26.6	54.9
31	4.6	8.2	14.9	25.9	34.4	39.4	41.2	33.7	24.7	13.9	5.9	3.9	18.2
32	4.0	6.5	10.7	17.6	22.6	26.0	27.7	23.2	18.1	11.2	5.0	3.4	13.1
33	2.9	4.3	6.1	9.6	11.9	13.9	15.2	13.2	11.1	7.8	3.6	2.5	7.78
34	1.6	2.0	2.2	3.3	3.9	4.9	5.6	5.1	4.8	4.2	2.0	1.4	3.18
35	0.4	0.3	0.1	0.1	0.1	0.3	0.4	0.5	0.7	1.2	0.5	0.4	0.35
36	0.0	0.3	1.1	1.8	2.4	1.9	1.7	1.2	0.5	0.0	0.0	0.0	0.65
37	1.7	3.3	7.2	10.4	13.2	12.0	12.1	9.6	6.2	2.0	1.9	1.3	5.97
38	7.3	11.7	20.9	29.0	35.8	33.8	34.9	28.5	20.8	9.6	8.3	6.0	19.0
39	20.6	29.6	46.5	61.7	74.7	72.4	74.6	62.0	48.3	26.3	22.7	17.9	43.9
40	48.6	64.1	90.4	114.	136.	137.	137.	115.	94.5	57.7	51.7	45.0	87.9
41	4.6	8.1	14.5	25.0	33.0	37.8	39.6	32.5	24.1	13.7	5.9	3.8	17.6
42	3.8	6.1	9.7	15.7	20.0	23.0	24.6	20.8	16.6	10.6	4.8	3.2	11.9
43	2.5	3.6	4.8	7.2	8.8	10.4	11.6	10.2	8.9	6.7	3.2	2.2	6.17
44	1.1	1.2	1.1	1.4	1.6	2.1	2.6	2.5	2.8	2.9	1.4	1.0	1.70
45	0.1	0.0	0.1	0.3	0.5	0.3	0.2	0.1	0.0	0.3	0.1	0.1	0.01

Treatment	Jan	Feb	Mar	Apr	May	Jun	Jul	Aug	Sep	Oct	Nov	Dec	Year
46	0.5	1.4	4.0	6.2	8.1	7.3	7.1	5.4	3.1	0.6	0.6	0.4	3.09
47	4.3	7.8	15.4	22.3	28.1	26.5	27.2	21.9	15.1	6.1	5.0	3.4	13.75
48	14.6	22.6	38.5	53.2	65.2	62.7	65.3	53.8	40.4	20.3	16.6	12.2	36.11
49	37.4	52.3	79.6	105.	126.	124.	128.	107.	85.3	48.7	41.2	32.7	76.78
50	84.1	108.	149.	187.	222.	226.	226.	190.	158.	100.	89.3	78.9	146.9
51	4.5	7.9	13.9	23.6	31.0	35.5	37.3	30.8	23.1	13.3	5.8	3.8	16.89
52	3.6	5.5	8.3	13.1	16.4	18.9	20.4	17.5	14.4	9.6	4.5	3.0	10.23
53	2.1	2.7	3.1	4.3	5.0	6.1	7.0	6.4	6.1	5.2	2.5	1.9	4.10
54	0.6	0.4	0.1	0.1	0.0	0.1	0.2	0.3	0.7	1.4	0.7	0.6	0.34
55	0.0	0.4	1.9	3.3	4.7	4.1	3.8	2.7	1.2	0.0	0.1	0.0	1.30
56	2.3	5.0	11.6	17.8	23.1	21.9	22.1	17.4	11.2	3.7	2.8	1.7	10.14
57	10.5	18.0	33.7	48.7	60.9	58.7	61.1	49.8	35.8	16.3	12.3	8.5	31.41
58	30.2	45.6	74.9	103.	125.	122.	128.	106.	82.1	43.7	34.3	25.4	71.97
59	71.7	98.5	146.	191.	229.	227.	236.	198.	160.	95.2	79.1	63.3	142.9
60	155.7	198.	264.	330.	390.	401.	399.	337.	285.	186.	164.	147.	263.7
61	4.2	6.9	11.0	17.4	21.8	24.9	26.7	22.9	18.4	11.7	5.3	3.6	15.59
62	2.4	3.0	3.0	3.6	3.7	4.3	5.3	5.2	5.8	5.6	3.0	2.2	7.72
63	0.4	0.1	0.2	0.9	1.9	1.8	1.3	0.6	0.0	0.6	0.4	0.5	1.59
64	0.6	2.7	10.0	18.9	27.0	27.3	26.1	19.2	10.1	2.0	0.8	0.3	0.38
65	7.7	17.7	41.8	68.9	91.5	92.6	93.4	73.6	47.5	17.5	9.7	5.7	8.23
66	30.1	55.7	108.	166.	212.	213.	221.	179.	127.	58.2	36.4	23.9	30.92
67	82.6	133.	230.	331.	412.	410.	433.	359.	271.	141.	97.1	68.2	76.83
68	192.0	279.	436.	597.	725.	721.	764.	642.	510.	293.	219.	164.	158.9
69	409.9	547.	777.	1009	1203	1211	1264	1070	889.	558.	452.	366.	298.6
70	841.7	1042	1337	1644	1929	2018	2005	1703	1478	1012	886.	809.	533.8
71	3.6	5.2	6.3	7.8	8.3	9.3	10.9	10.5	10.7	8.8	4.5	3.1	13.15
72	0.8	0.2	0.3	2.5	5.5	6.0	4.6	2.2	0.1	0.7	0.9	0.9	3.75
73	0.9	5.4	23.1	49.5	74.2	79.7	75.3	54.3	27.3	5.4	1.4	0.4	0.07
74	14.5	38.9	102.	184.	254.	267.	265.	205.	126.	43.7	19.2	10.3	9.05
75	62.0	129.	277.	452.	594.	615.	630.	504.	343.	146.	77.9	47.8	40.05
76	179.8	320.	599.	913.	1161	1185	1239	1016	738.	361.	218.	144.	106.3
77	431.8	684.	1151	1656	2051	2067	2193	1827	1402	759.	508.	359.	227.6
78	935.3	1344	2058	2810	3404	3414	3633	3063	2462	1456	1069	804.	434.8
79	1918.	2532	3535	4577	5443	5515	5767	4897	4113	2642	2116	1723	779.9
80	3853.	4720	5955	7276	8514	8971	8900	7582	6649	4644	4052	3730	1356.
81	3.6	5.2	6.3	7.8	8.3	9.3	10.9	10.5	10.7	8.8	4.5	3.1	7.07
82	0.8	0.2	0.3	2.5	5.5	6.0	4.6	2.2	0.1	0.7	0.9	0.9	0.34
83	0.9	5.4	23.1	49.5	74.2	79.7	75.3	54.3	27.3	5.4	1.4	0.4	23.59
84	14.5	38.9	102.	184.	254.	267.	265.	205.	126.	43.7	19.2	10.3	103.9
85	62.0	129.	277.	452.	594.	615.	630.	504.	343.	146.	77.9	47.8	279.1
86	179.8	320.	599.	913.	1161	1185	1239	1016	738.	361.	218.	144.	603.5
87	431.8	684.	1151	1656	2051	2067	2193	1827	1402	759.	508.	359.	1159.
88	935.3	1344	2058	2810	3404	3414	3633	3063	2462	1456	1069	804.	2078.
89	1918.	2532	3535	4577	5443	5515	5767	4897	4113	2642	2116	1723	3584.
90	3853.	4720	5955	7276	8514	8971	8900	7582	6649	4644	4052	3730	6087.

APENDIX B

Intermediate results

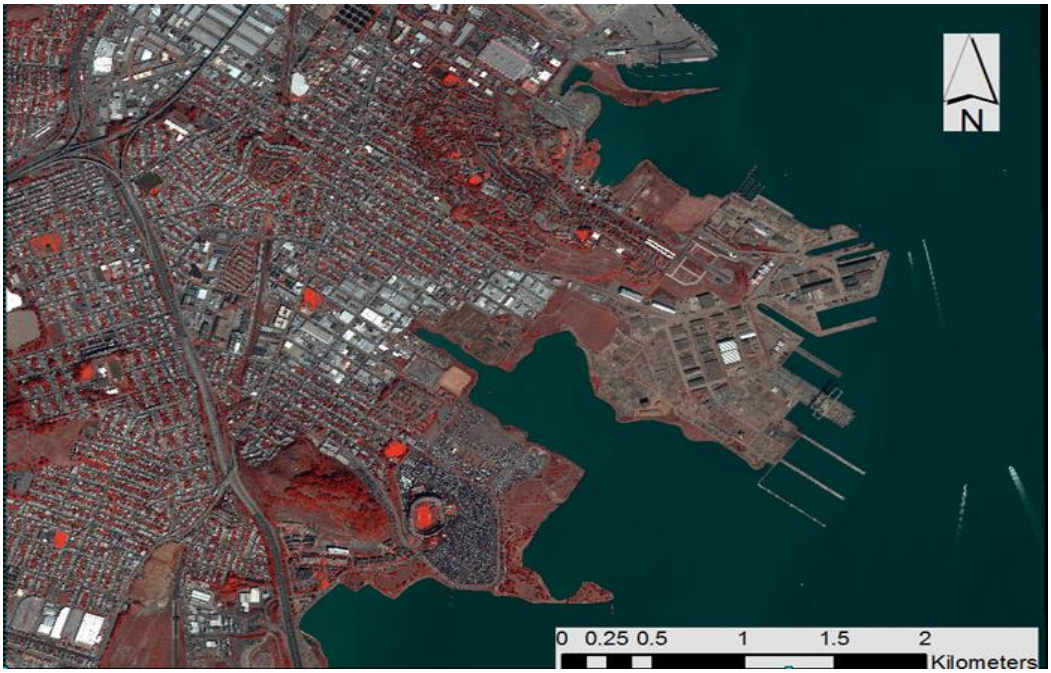

Figure B-1 False Color of the Study Area

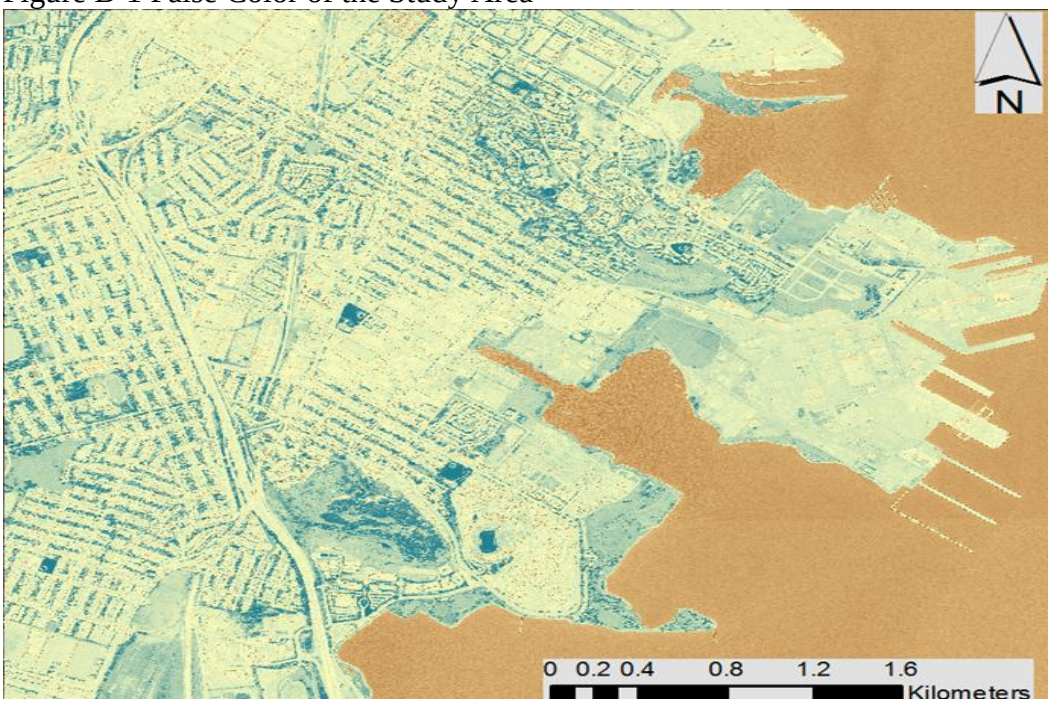

Figure B-2 NDVI of the Study Area

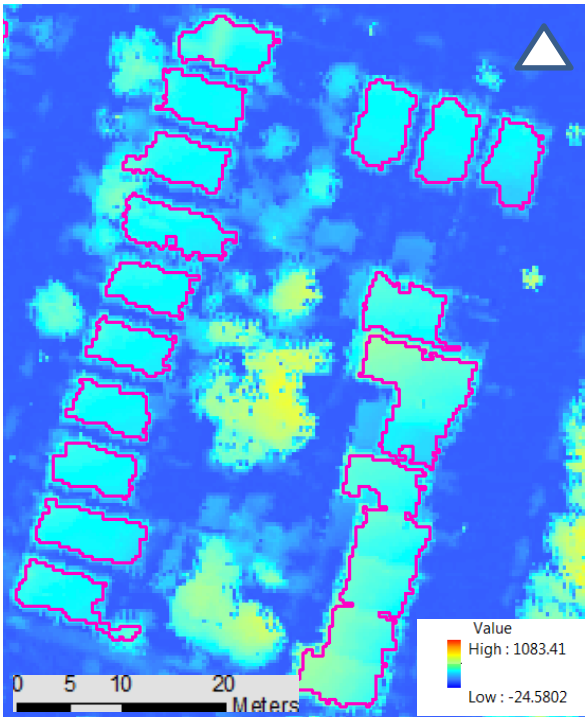

Figure B- 3 Buildingoutlines over nDEM

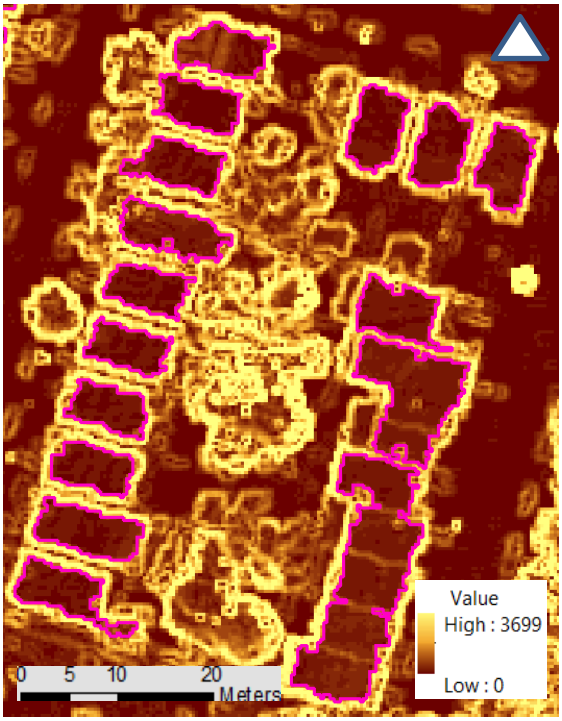

Figure B- 4 Buildingoutlines over Sobel

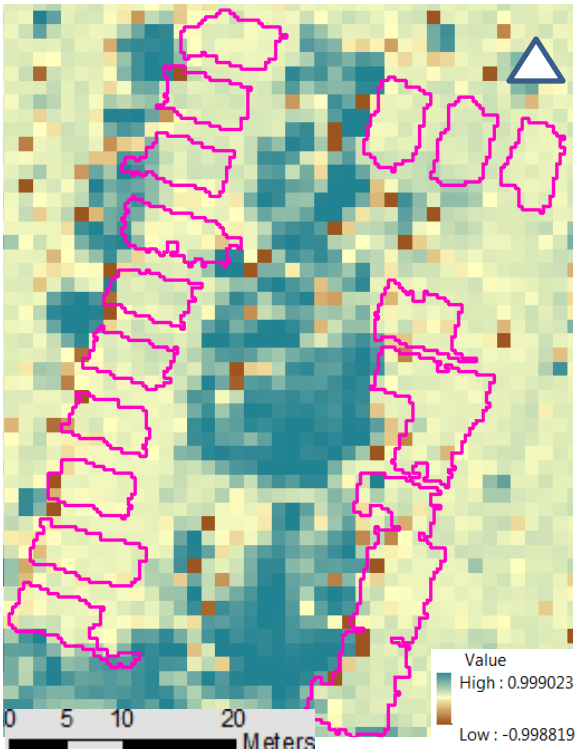

Figure B-5 Building outlines over NDVI

Table

BuildingDT3_2

FID	Shape *	ID	nDEM	NDVI	Sobel	p_a
0	Polygon	403	6.8898	0.056269	0.277949	0.198375
1	Polygon	422	5.80816	0.028604	0.249414	0.234349
2	Polygon	465	5.21461	-0.030167	2.0932	0.498874
3	Polygon	509	5.04061	-0.039643	0.731274	0.247071
4	Polygon	574	6.25019	0.043928	1.523	0.221249
5	Polygon	589	3.96281	0.028889	0.542382	0.280811
6	Polygon	837	6.6255	0.02195	0.475528	0.168504
7	Polygon	862	7.41355	0.018606	0.683464	0.311155
8	Polygon	884	6.87228	-0.017137	0.209771	0.137968
9	Polygon	922	3.62822	0.047246	0.462454	0.351648
10	Polygon	925	3.14454	0.024389	1.22306	0.33316
11	Polygon	938	7.60739	0.316981	1.8849	0.40257
12	Polygon	962	4.66453	0.015492	0.301451	0.159771
13	Polygon	985	6.27872	-0.011348	2.00104	0.144738
14	Polygon	986	6.23071	-0.004035	1.48657	0.408879
15	Polygon	100	7.30811	-0.015732	0.35225	0.136823
16	Polygon	103	8.60157	-0.013833	1.07052	0.396808
17	Polygon	108	5.66703	-0.027556	1.76216	0.19358

0 (0 out of 5587 Selected)

BuildingDT3_2

Figure B- 6 Table of properties of the Building outlines

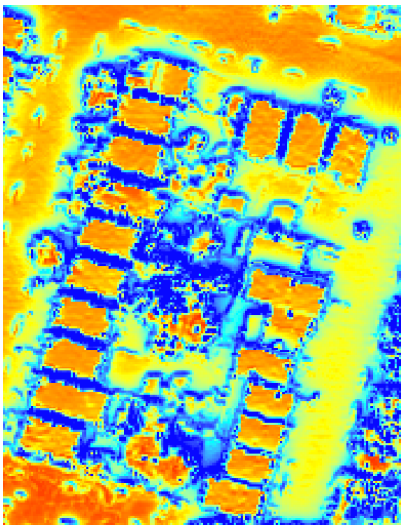

Figure B-7 Solar radiation map

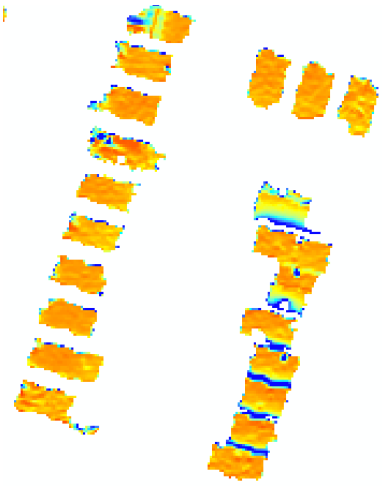

Figure B-8 Solar radiation on rooftops

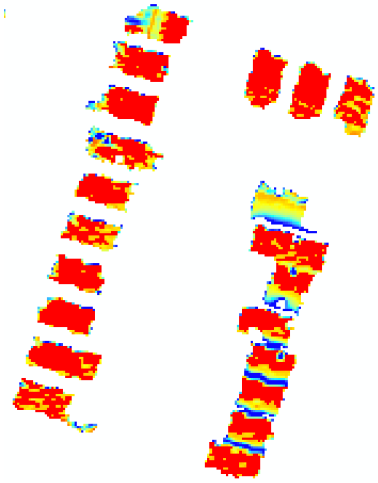

Figure B-9 Suitable areas to install PV (red)

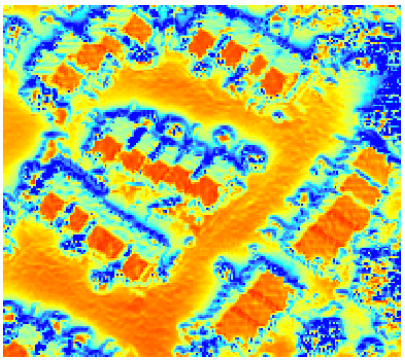

Figure B-10 Solar radiation map

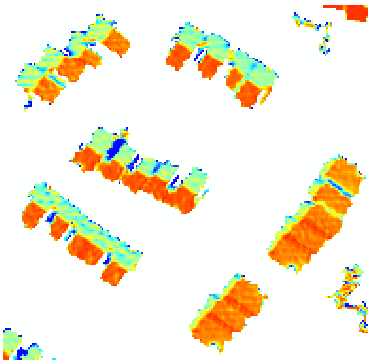

Figure B- 11 Solar radiation on rooftops

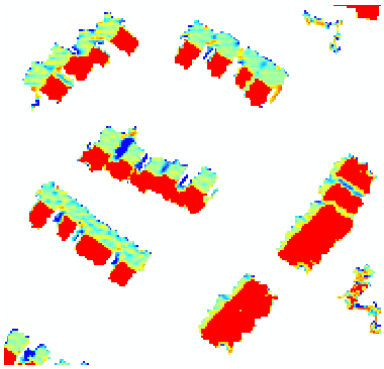

Figure B-12 Suitable areas to install PV (red)